Imaging Ionic Flux through Individual Pores in Droplet Interface Bilayers



Marc Szabo

Trinity College

University of Oxford

A dissertation submitted for the degree of

Doctor of Philosophy

January 2016

Abstract

Optical measurements of ion flux are a powerful technique when studying the functional properties of ion channels and the dynamics of pore formation in biological membranes. The simultaneous read-out of optical single channel recordings (oSCR) provides an alternative way of measuring electrical activity and is more feasible than parallelising electrical measurements. Channel activity is monitored with ion specific indicator dyes whose response is proportional to the magnitude of the current. Here, two novel applications of oSCR in a droplet interface bilayer model membrane system are presented.

Firstly, a technique for potassium-flux imaging through individual electropores is developed. Three indicator dyes are characterised with fluorescence spectroscopy and oSCR of potassium-flux are shown for the first time. Dynamic fluorescence response when applying a voltage protocol can be observed while monitoring currents through several pores in parallel. The response time is between 2.5-10 s and the minimum resolvable current is estimated to be -2 nA.

Secondly, pore formation in the presence of four antimicrobial peptides (melittin, magainin 2, alamethicin, indolicidin) is visualised by calcium-flux imaging combined with single-molecule imaging of labelled peptides in the same membrane region. Calculations of radial distribution functions show a uniform distribution of peptides on the membrane surface. Punctate poration events observed with calcium-flux most likely originate from barrel-stave (alamethicin) or toroidal pores (melittin and magainin 2), whereas indolicidin does not promote pore formation.

The techniques developed in this thesis are an important contribution to the field of oSCR.

Declaration

The work described in this thesis was carried out between October 2012 and January 2016 in the laboratory of Dr. Mark I Wallace at the Chemistry Research Laboratory of the University of Oxford. All the work described within this thesis is my own, unless explicitly attributed to my collaborators. This work has not been submitted previously for any other degree at the University of Oxford or any other university. Publications prepared from this work are stated in Appendix A.

Marc Szabo

January 2016

Acknowledgements

First of all I'd like to thank my supervisor Mark Wallace for the opportunity to work in his group for the past three years and his constant support. I am also thankful to my co-supervisor Stephen Tucker.

I would like to the thank the DTC program directors for their support over the course of 4 years and EPSRC for providing me with a full stipend.

The Wallace Group has provided a great work environment and I will miss the good spirit and supportive atmosphere. Thanks to Hajra Basit, Matthew Blosser, Matthew Cheetham, Helena Coker, Linus Conrad, John Danial, Daniel Kattnig, Vivek Ramakrishna, Ravinash Krishna Kumar, Carina Monico, Jason Sengel, Michael Senior, Lyndsey Starr, Eve Weatherill and Shidong Xi. It's been a great time!

The friendships I have formed over the past 4 years are invaluable to me and there are many people I wouldn't have met if it weren't for Trinity MCR.

Thanks to Anna Regoutz, Caitlin Gale and Nat Upton for always being good friends and for several weekend getaways into the British countryside.

There's nothing like a Trinity breakfast to get you started in the morning, many of which I have enjoyed with Jenni Zelenty, Andy Dahl and Abi Buglass.

Special thanks to Fred Jayatilaka and Richard Crowther for teaching me almost everything I know about British culture and humour.

Over the course of 4 years, one sees many people who come and leave, but the friendships remain and I am very glad that we've kept in touch. Thanks to Richard Bunworth, Michael Dela Cruz, Liz Gourd, Jazz Jagger, Alicia Kielmovitch, Matthias Meier, Carolina Sena and Charlotte Watter.

Many people have stayed and accompanied me for all or most of my time at Oxford and I'd like to thank Lina Arthur, Hannah Boston, Ben Cartlidge, Karolina Chocian, Jonathan Downing, Malte Luecken, Nayab Malik, Phoebe Oliver, Charly Treiber and Nikola Vlahov. Many thanks also to the entire DTC 2011 cohort.

I am very fortunate to have formed many long-lasting friendships from the days of secondary school and I'd like to thank Regina Groth, Gunnar Herzig, Nils Schwesig and Peter Stihl. Thanks also to Marin Hirschfeld for being my companion during

one year of Russian studies.

Finally, I wouldn't have made it this far if it weren't for the everlasting support of my family and I am therefore indebted to Gerlinde, Zoltan and Andy Szabo.

Contents

List of Figures **x**

List of Abbreviations **xiii**

1 Introduction **1**

1.1 Biological membranes 1

1.2 Cell membrane mimics 4

1.2.1 Black lipid membranes 5

1.2.2 Supported lipid bilayers 6

1.2.3 Droplet interface bilayers 8

1.3 Ion conductance and pore formation in cell membranes 10

1.3.1 Ion channels 10

1.3.2 Electroporation 12

1.3.3 Antimicrobial peptides 14

1.4 Single-channel recording techniques 18

1.4.1 Patch-clamping 19

1.4.2 Channel recordings in model membranes 20

1.4.3 Optical single-channel recordings 21

1.5 Summary 24

2 Experimental techniques **26**

2.1 Materials . . . 26
2.2 Droplet interface bilayers . . . 27
2.2.1 Device fabrication . . . 27
2.2.2 Lipid stock preparation . . . 27
2.2.3 DIB formation . . . 28
2.3 Electrical recordings . . . 30
2.4 Fluorescence spectroscopy of potassium indicator dyes . . . 32
2.5 TIRF Imaging . . . 34
2.6 TIRF microscopy setup . . . 35
2.6.1 Potassium flux imaging . . . 35
2.6.2 Dual-colour imaging . . . 36
2.6.3 Combined calcium-flux and single-molecule AMP imaging . . . 38
2.7 Gaussian fitting and single-particle tracking . . . 40
2.7.1 Gaussian fitting . . . 40
2.7.2 Single-particle tracking . . . 41

3 Imaging potassium-flux through individual electropores 44

3.1 Introduction . . . 45
3.2 Potassium indicator dyes . . . 48
3.2.1 APG-2 . . . 49
3.2.2 APG-4 . . . 49
3.2.3 KS2 . . . 50
3.3 Experimental details and data analysis . . . 51
3.3.1 Fluorescence spectroscopy . . . 51
3.3.1.1 APG-2 . . . 51
3.3.1.2 KS2 . . . 52
3.3.1.3 APG-4 . . . 52

3.3.2 DIB formation . . . 52
3.3.2.1 APG-2 . . . 53
3.3.2.2 APG-4 . . . 54
3.3.3 Electrical recordings . . . 54
3.3.4 Data analysis . . . 55
3.4 Results . . . 56
3.4.1 APG-2 . . . 56
3.4.1.1 Fluorescence spectroscopy . . . 56
3.4.1.2 Potassium-flux imaging . . . 58
3.4.2 KS2 . . . 59
3.4.3 APG-4 . . . 61
3.4.3.1 Fluorescence spectroscopy . . . 61
3.4.3.2 Potassium-flux imaging . . . 63
3.4.3.3 Estimate of minimum detectable current . . . 67
3.5 Discussion . . . 69

4 Electrophysiology and pore formation imaging of AMPs 74

4.1 Introduction . . . 75
4.1.1 Melittin . . . 76
4.1.2 Magainin 2 . . . 78
4.1.3 Alamethicin . . . 81
4.1.4 Indolicidin . . . 82
4.1.5 Summary . . . 84
4.2 Electrophysiology . . . 85
4.2.1 Melittin results . . . 87
4.2.2 Magainin 2 results . . . 89
4.2.3 Alamethicin results . . . 91

4.2.4 Indolicidin results 92
4.2.5 Effect of calcium 93
4.2.6 Discussion 95
4.3 Calcium-flux oSCR and single-molecule peptide imaging 97
4.3.1 Experimental details and analysis 97
4.3.2 Melittin results 100
4.3.2.1 Imaging and tracking 100
4.3.2.2 Radial distribution function 101
4.3.2.3 Spot count and diffusion analysis 104
4.3.3 Magainin 2 results 105
4.3.3.1 Imaging and tracking 105
4.3.3.2 Radial distribution function 107
4.3.3.3 Spot count and diffusion analysis 108
4.3.4 Alamethicin results 110
4.3.4.1 Imaging and tracking 110
4.3.4.2 Radial distribution function 110
4.3.4.3 Spot count and diffusion analysis 112
4.3.5 Indolicidin results 114
4.3.5.1 Imaging and tracking 114
4.3.5.2 Radial distribution function 114
4.3.5.3 Spot count and diffusion analysis 114
4.3.6 Discussion 117
4.4 Conclusions 121

5 Conclusions and future work **123**

5.1 Potassium-flux imaging 123
5.2 Pore formation and AMP imaging 125

5.3 Summary 128
5.4 Publications 128

Bibliography **129**

A Publications **156**

A.1 Accepted 156
A.2 In preparation 156

B Code **157**

B.1 Potassium imaging: step profile 157
B.2 Potassium imaging: squarewave profile 158
B.3 AMP imaging: radial distribution functions 159
B.4 Gaussian fitting of pores 162

List of Figures

1.1 Self-assembly of lipids in aqueous environment 2

1.2 Lipid structures 3

1.3 Black lipid membrane 6

1.4 Supported lipid bilayer 7

1.5 Sketch of hydrogel supported DIB 9

1.6 Conformational changes and gating of ion channel 11

1.7 Electroporation 13

1.8 AMP chain lengths and net charge 15

1.9 Pore-formation models 16

1.10 Patch-clamping setup 19

1.11 Single-channel recordings in DIB 21

1.12 Optical single-channel recordings through alpha-hemolysin pores . . . 23

2.1 PMMA device and incubation tank 28

2.2 DIB and electrical setup 29

2.3 Picture of electrical setup 31

2.4 Optical setup for potassium-flux imaging 36

2.5 Optical setup for dual-colour imaging 37

2.6 Combined calcium-flux and labelled AMP imaging 39

3.1 Structure of APG-2 49

3.2 Structure of APG-3 50
3.3 Structure of KS2 50
3.4 DIB setup for potassium-flux imaging 53
3.5 Background correction for imaging data 55
3.6 APG-2 titrations 57
3.7 APG-2 titration with Kryptofix-222 58
3.8 Potassium-flux imaging with APG-2 59
3.9 Characterisation of KS2 60
3.10 Sensitivity of APG-4 to Na^+ ions 61
3.11 Characterisation of APG-4 62
3.12 Square-wave potential analysis of potassium-flux imaging with APG-4 64
3.13 Average fluorescence profile and current 65
3.14 Determining the sensitivity of APG-4 by applying a step-potential . 66
3.15 Estimate of minimum detectable current 68
3.16 Images of individual pores used for analysis 69
3.17 Potassium-flux imaging in the absence of Kryptofix-222 70

4.1 Melittin structure 76
4.2 Magainin 2 structure 79
4.3 Alamethicin structure 81
4.4 Indolicidin structure 83
4.5 Analysis of electrical data 87
4.6 Electrical characterisation of melittin 88
4.7 Electrical characterisation of magainin 2 89
4.8 Electrical characterisation of alamethicin 91
4.9 Electrical characterisation of indolicidin 93
4.10 Melittin activity with $CaCl_2$ substrate buffer 94

4.11 Melittin images for calcium-flux and labelled AMPs 102
4.12 Radial distribution functions for melittin 103
4.13 Spot count and diffusion constants for melittin 103
4.14 MSD for melittin 104
4.15 Magainin 2 images for calcium-flux and labelled AMPs 106
4.16 Average signal over time 107
4.17 Radial distribution functions for magainin 2 108
4.18 Spot count and diffusion constants for magainin 2 108
4.19 MSD for magainin 109
4.20 Alamethicin images for calcium-flux and labelled AMPs 111
4.21 Radial distribution functions for alamethicin 112
4.22 Spot count and diffusion constants for alamethicin 112
4.23 MSD for alamethicin 113
4.24 Indolicidin images for calcium-flux and labelled AMPs 115
4.25 Radial distribution functions for indolicidin 116
4.26 Spot count and diffusion constants for indolicidin 116
4.27 MSD for indolicidin 117
4.28 Melittin imaging with 100% labelled peptides 120

List of Abbreviations

AMP	Antimicrobial peptide
APG	Asante Potassium Green
BLM	Black Lipid Membrane
CL	Cardiolipin (1',3'-bis[1,2-dimyristoyl-*sn*-glycero-3-phospho]-*sn*-glycerol)
CNC	Computer Numerical Control
DOPC	1,2-Dioleoyl-*sn*-glycero-3-phosphocholine
DPhPC	1,2-diphytanoyl-*sn*-glycero-3-phosphocholine
DPPG	1,2-dihexadecanoyl-*sn*-glycero-3-phospho-(1'-*rac*-glycerol)
DIB	Droplet Interface Bilayer
E.coli	Escherichia coli
EDTA	Ethylenediaminetetraacetic Acid
EMCCD	Electron Multiplying Charge Coupled Detector
FRET	Forster Resonance Energy Transfer
GUV	Giant Unilamellar Vesicle
HEPES	4-(2-hydroxyethyl)-1-piperazineethanesulfonic acid
MIC	Minimum Inhibitory Concentration
NMR	Nuclear Magnetic Resonance
oSCR	Optical Single Channel recordings
PBFI	Potassium-Binding Benzofuran Isophthalate
PMMA	Poly-Methyl Methacrylate

POPE	1-hexadecanoyl-2-(9Z-octadecenoyl)-*sn*-glycero-3-phosphoethanolamine
POPG	1-hexadecanoyl-2-(9Z-octadecenoyl)-*sn*-glycero-3-phospho-(1'-*rac*-glycerol)
RDF	Radial Distribution Function
S.aureus	Staphylococcus aureus
SLB	Supported Lipid Bilayer
TAMRA	Tetramethylrhodamine
TMA	Tetramethyl Ammonium
TIRF	Total Internal Reflection Fluorescence

Chapter 1

Introduction

1.1 Biological membranes

The cell and its enclosing membrane are the essential building blocks of life. The number of cells in the human body is estimated to be 3.72×10^{13}, all of which carry out specialised functions such as immune response, cognitive activity or metabolism [1]. The membrane acts as both a protective boundary and as a regulatory gate for the intake and release of nutrients to every cell. Understanding its properties and components is vital to understanding the mechanisms of single-and multicellular life. Although membrane proteins themselves can be targeted by pathogens causing various diseases [2], direct disruption of the membrane structure can also play an important role in cell destruction or malfunction. This is exploited by defence agents called antimicrobial peptides (AMPs), which act as part of the innate immune system by means of cell lysis, among other mechanisms. The stability and structure of membranes is vital to the function of cells and is enabled by the organisation of lipids into bilayer structures. There are typically over 100 chemically distinct types of lipids present in every mammalian cell [3] and their amphiphilic nature is responsible for bilayer structures formed in aqueous environments. Hy-

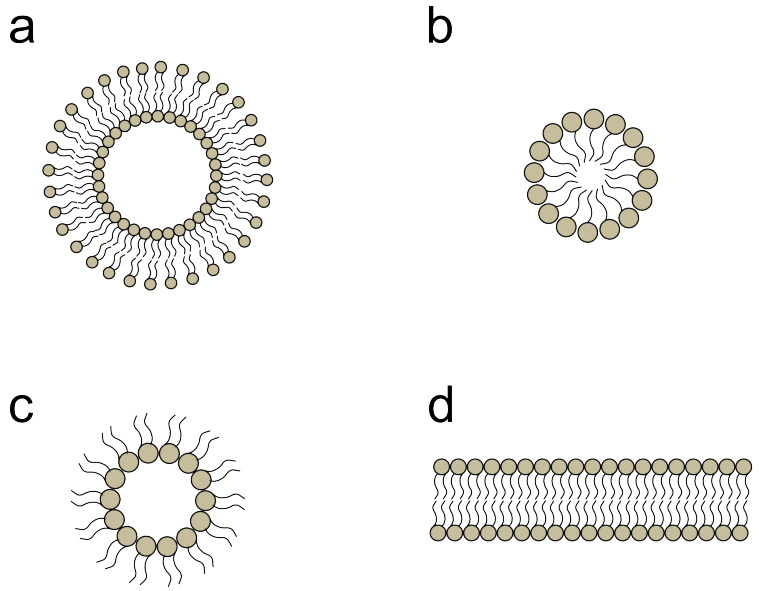


Figure 1.1: Amphiphilic lipids can self-assemble into different structures in an aqueous environment **(a)** Liposomes or vesicles **(b)** Micelles **(c)** Inverted micelles **(d)** Bilayers

drophilic headgroups are oriented towards an aqueous solvent whereas the tails are oriented towards other lipid tails, leaving only the headgroups exposed. Depending on lipid concentration and the ratio of polar to non-polar areas, several polymorphic forms such as micelles or liposomes can occur as shown in Fig.1.1 [4]. There is large chemical variation among different lipids and the LIPID MAPS database identifies more than 40000 unique lipid structures [5]. In very general terms, lipids have been defined as biological substances which are hydrophobic in nature and only soluble in organic solvents [6]. Most lipids show similarities on a functional level, which enables their interaction in cell membranes. The basic structure is composed of a backbone (e.g. glycerol or sphingosine) which typically forms ester bonds with one or more hydrophobic fatty acid chains of variable length. Furthermore, the backbone is attached to a hydrophilic head group. This is often a phosphate group which is also attached to additional molecules such as sugars, amino acids or alcohols. The chemical diversity of lipids arises from variation with respect to any of these components. The fatty acid chains can vary in number and length. They can also be

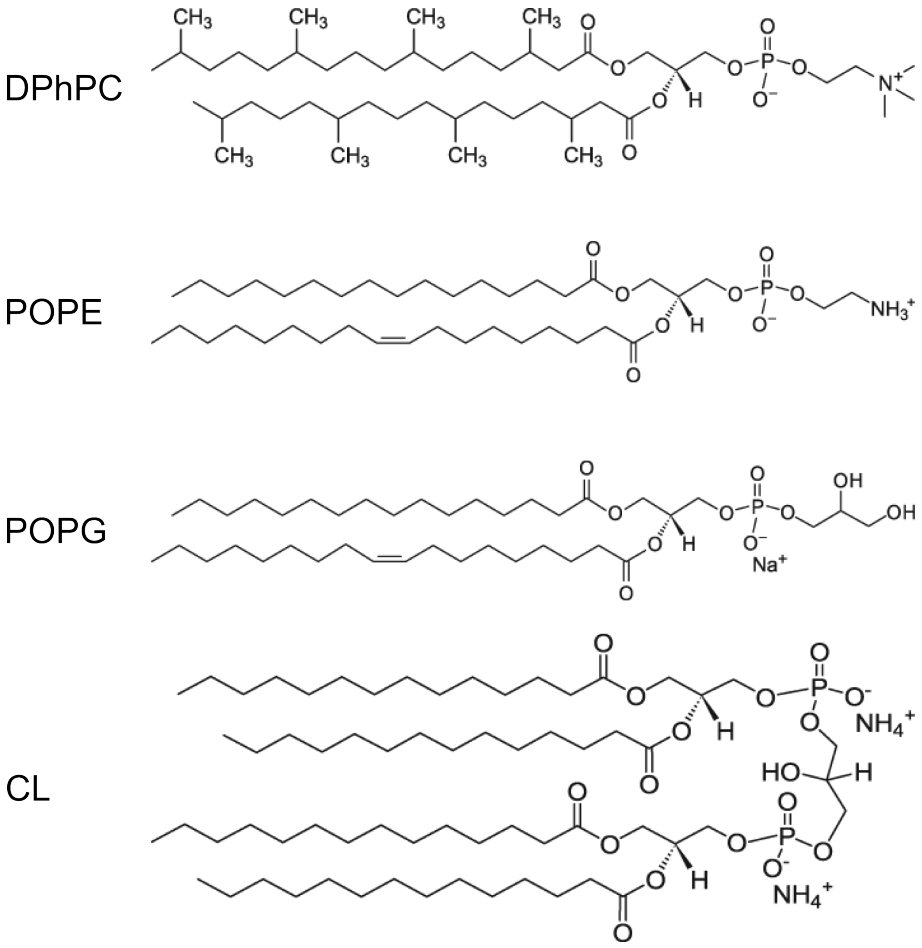


Figure 1.2: Structures of all the lipids used in this thesis. Structures reproduced from *www.avanti.com*

saturated or unsaturated. Unsaturated tails have one or more double-bonds, which introduce a kinked tail structure. Together with different backbones and attached head groups, many different lipid molecules are constructed in nature [7, 8]. The most common types of lipid groups can be categorised into Glycerophospholipids, Sphingolipids, Glycolipids or Sterols. Glycerophospholipids make up around 40-60 mol% of all biological membranes [9]. Their basic structure consists of saturated or unsaturated fatty acid chains and a polar phosphate head group linked together by glycerol. The head groups vary depending on the alcohol linked to the phosphate group which can be choline, ethanolamine, serine, glycerol or inositol. Correspondingly, the head groups are abbreviated as PC, PE, PS, PG or PI [9] and the head

groups can be either zwitterionic or negatively charged. In most eukaryotes, zwitterionic PC makes up more than 50 % of membrane lipids [10]. Bacterial membranes, on the other hand, are mostly composed of zwitterionic PE lipids as well as negatively charged PG and Cardiolipin (CL) lipids [11]. In this thesis, the following variety of lipids are used in an artificial lipid bilayer system to create different types of cell mimics:

- 1,2-diphytanoyl-*sn*-glycero-3-phosphocholine (DPhPC)
- 1-hexadecanoyl-2-(9Z-octadecenoyl)-*sn*-glycero-3-phosphoethanolamine (POPE)
- 1-hexadecanoyl-2-(9Z-octadecenoyl)-*sn*-glycero-3-phospho-(1'-*rac*-glycerol) (POPG)
- 1',3'-bis[1,2-dimyristoyl-*sn*-glycero-3-phospho]-*sn*-glycerol (Cardiolipin).

The structure of each lipid is shown in Fig.1.2.

1.2 Cell membrane mimics

The desire to understand properties of membranes has led to the development of model systems that act as membrane mimics. Any natural cell is a highly complex structure with many different proteins embedded in its membrane and an intracellular machinery including all the components for reproduction and cell division. The reduction of complexity to a very basic level in membrane mimics, makes fundamental properties such as lipid composition, bilayer formation or lipid-protein interactions more easily accessible[12]. While any artificial system is only realistic to a limited extent, it can be a powerful tool due to its ability to easily control basic parameters that would be difficult to manipulate in real cells. The most prevalent cell membrane mimics will be discussed in the following sections.

1.2.1 Black lipid membranes

Black Lipid Membranes (BLMs), first introduced by Mueller et al., have been used extensively as model membranes [13]. Apart from allowing formation of a lipid bilayers, this technique also enables electrical recordings between two chambers separated by the bilayer [14]. The membrane is formed over an aperture connecting the two chambers. A hole of typically 1 mm diameter is formed in a hydrophobic material like Teflon and lipids are either painted over the opening, or applied in a volatile solvent to the air and water interface. Subsequent raising and lowering of the liquid over the aperture results in bilayer formation. Two compartments contain an aqueous solution of interest and are exposed to one monolayer each, both of which make up the bilayer. By applying an electrical field across the membrane, ion flux across the bilayer can be detected. Various channels and pore forming proteins have been incorporated and studied in BLMs. Examples include the peptide gramicidin A [15], bacterial outer membrane proteins [16] and alpha-hemolysin [17]. While BLMs have proven to be a very powerful and versatile technique[18], there are several drawbacks, most importantly protein reconstitution, which have lead to the development of alternative membrane mimics. The membrane usually exhibits poor stability and the bilayer area itself is not readily accessible by surface detection techniques [19]. An improved method increasing stability and creating a portable membrane with a single nanopore formed between an agarose gel has been reported recently [20]. Systems allowing more controlled incorporation of proteins into planar bilayers by means of vesicle fusion [21] or microfluidic delivery[22] have also been developed. Furthermore, protein insertion into model membranes can be realised by transfer with mechanical probes [23, 24]. Despite improvements to classic BLMs addressing stability and protein insertion, alternatives are required especially when it comes to parallel electrical and optical measurements of the bilayer area.

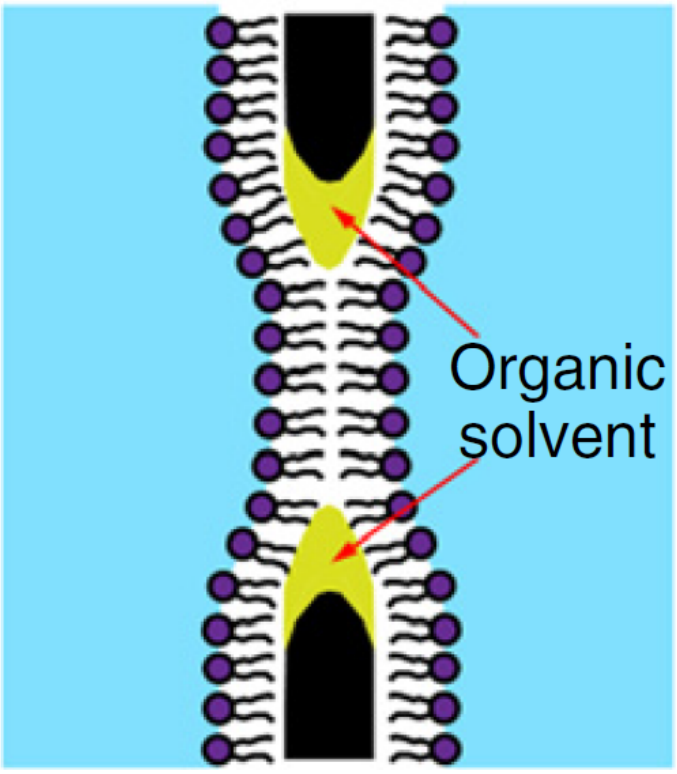


Figure 1.3: Schematic of a black lipid membrane. Bilayers are formed across an annulus formed of a hydrophobic material such as teflon. Residual organic solvent used to dissolve lipids is located between leaflets around the edges. Both sides of the bilayer are embedded in an aqueous solution. Reproduced from [25]

1.2.2 Supported lipid bilayers

Supported Lipid Bilayers (SLBs) formed on a solid substrate are an important alternative to BLMs [26]. One key advantage is the exposure of one bilayer leaflet, therefore making it accessible to surface characterisation techniques such as Total Internal Reflection Microscopy, Surface Plasmon Resonance or Atomic Force Microscopy [27, 28]. Various substrates can be used for bilayer formation such as silica, mica or borosilicate glass. There are several methods to form supported bilayers such as the Langmuir-Blodgett technique where a hydrophilic substrate is pulled through a lipid monolayer which adheres to the substrate. This is followed by pushing the substrate coated with the monolayer through another monolayer resulting in formation of a bilayer [19]. An easier and more popular method is bilayer

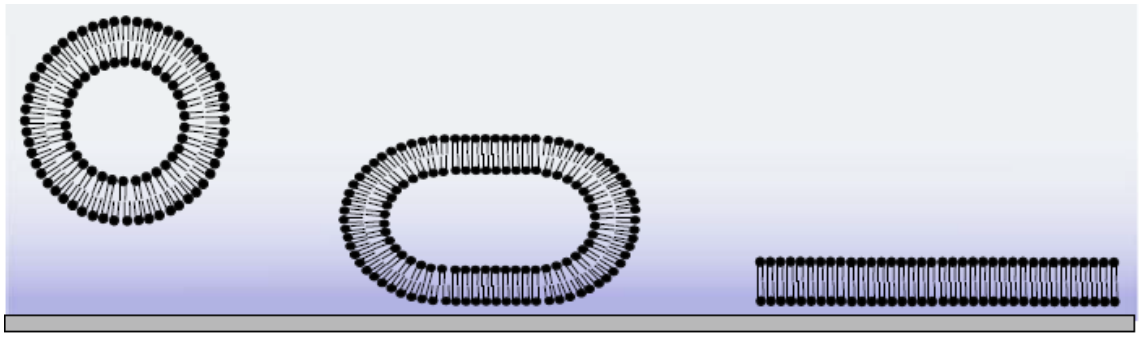


Figure 1.4: Example of supported lipid bilayer formation by vesicle rupture on a surface. Reproduced from [12]

formation by vesicle fusion [19]. A bulk solution is placed on a hydrophilic substrate leading to adsorption and fusion of vesicles which eventually rupture and form a planar supported bilayer on the substrate. A major advantage of SLB formation with this method is the incorporation of membrane proteins which can be done during vesicle production. The resulting bilayer will therefore include the protein of choice. Mobility and lateral diffusion in SLB systems is somewhat preserved by the presence of a thin (1 nm) water film between substrate and bilayer, but lipid diffusion is considerably slower in SLBs [29]. Interactions with the substrate can also compromise the mobility and function of transmembrane proteins, especially those with large peripheral domains. Overcoming this limitation led to the development of polymer-cushioned bilayers [30]. In order to prevent adsorption to the support surface, a polymer layer is formed between the bilayer and the surface. Despite having various advantages over BLMs regarding membrane accessibility, SLBs are not ideal for electrical characterisation of channel proteins incorporated into the bilayer, because incorporation of an electrical apparatus with a tight seal is not possible. Combined electrical and membrane surface specific measurements such as fluorescence microscopy can be realised using Droplet Interface Bilayers.

1.2.3 Droplet interface bilayers

Electrical recordings in SLBs are generally problematic, because open edges and defects hamper the establishment of an electric seal between both leaflets of the bilayer. The recently developed technique called Droplet Interface Bilayers (DIBs) allows formation of stable electrical seals between both side of the bilayers (> 100 GΩ) enabling single-channel recordings of various proteins that insert into the membrane [31, 32]. DIBs are either formed between two droplets or between a droplet and a hydrogel. The agarose hydrogel is formed on a glass coverslip and a monolayer forms by exposition to a lipid-in-oil solution. Aqueous droplets are incubated in the same solution which leads to a lipid monolayer coating around the droplet. Bilayers form when the droplet is placed on top of the monolayer that has previously formed on the hydrogel (Fig.1.5). This particular setup enables parallel electrical recordings and imaging of the bilayer region. Single molecule tracking of membrane proteins as well as optical-single channel recordings through alpha-hemolysin pores were both realised using this technique [31, 33] . For this thesis, the DIB technique was chosen for several reasons. The most important feature is the possibility of parallel electrical and optical readout. Due to the bilayer formation on a substrate-coated cover-slip, the bilayer area can be imaged with TIRF microscopy while performing electrical measurements with an inserted electrode. Therefore, oSCR can be used to image ion conductance through pores. This would not be possible with BLMs or SLBs. While SLBs are also formed on a substrate, tight electrical seals cannot be formed easily. Another major advantage of DIBs is the control of system parameters such as lipid and buffer composition. For the experiments involving AMPs, the concentration of peptides needs to be adjusted to regions where they cause pore formation. In addition, DIBs show greater stability than other model membrane systems and the experiments performed here require bilayer stability for at least 30-60 minutes. Bilayer formation on a hydrogel substrate can also be a drawback of this method,

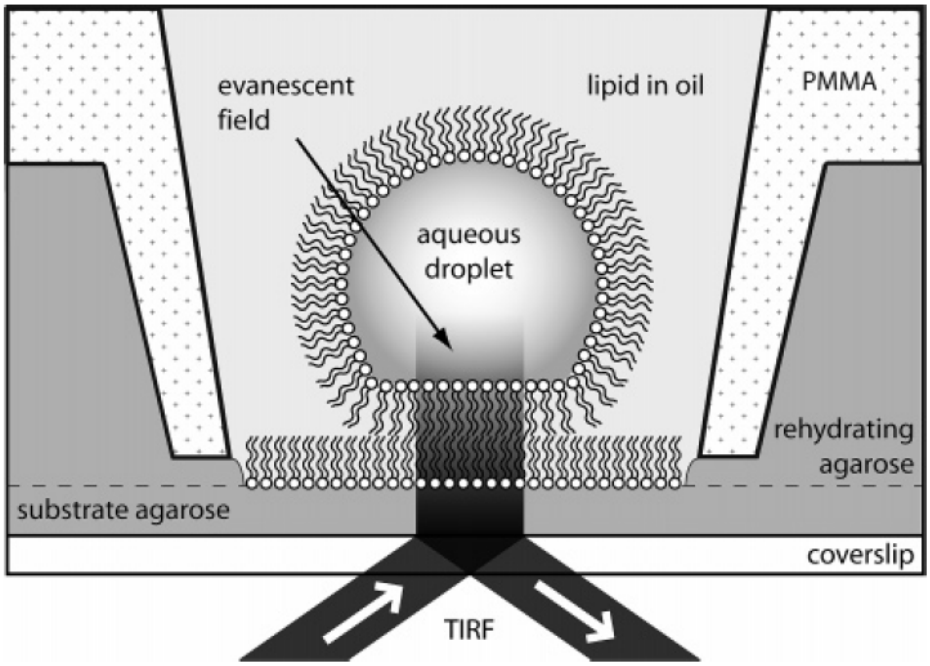


Figure 1.5: DIB setup using TIRF microscopy of the bilayer region. A monolayer is formed on a planar hydogel and around the aqueous droplet after incubation in a lipid-in-oil solution. When bringing both into contact, bilayers form. Reproduced from [31]

because it can influence protein diffusion and also hydration of the bilayer. Furthermore, lipid concentrations higher than 2 mg/ml are usually required for stable bilayer formation. This however not an issue for the experiments performed in this thesis where concentrations of 3.5 mg/ml (PE/PG/CL) and 8.7 mg/ml (DPhPC) are used. As with other model membrane systems, DIBs are an artificial system with much less complexity than a real cell membrane.

The experiments in this thesis could not be easily realised in any other model membrane system, because only DIBs allow the combination of electrical and optical measurements together with control over bilayer and buffer composition. More details on DIBs and protocols can be found in the literature [34, 35].

1.3 Ion conductance and pore formation in cell membranes

A planar lipid bilayer acts as an electrical seal allowing hardly any permeation of ions or other molecules across the membrane. This stability is of course vital to maintain a protective barrier for all intracellular components. However, rather than being closed off and isolated entities, biological cells constantly release and take up nutrients while also controlling their transmembrane voltage [36]. The otherwise insulating membrane barrier can be crossed through a system of ion channels and transporters which regulate access to cells. Ion transport through channels also regulates electrical signalling which is vital to processes such as cell communication or muscle contraction [37]. The stability and structural integrity of the membrane is essential to keep cells alive and functional. Targeted disruption of specific membranes and subsequent lysis by antimicrobial peptides is an integral part of the innate immune system and allows broad antibacterial defense [38]. Apart from natural transport across cells, forced cell permeation can be achieved through electroporation which is caused by applying high voltages and is widely used in biotechnology [39]. The following section gives a review of ion conductance and pore formation mechanisms in cell membranes.

1.3.1 Ion channels

Ion channels are pore-forming transmembrane proteins that regulate ion transport across cell membranes. They provide the foundation for electrical excitability of cells and neurotransmission, which are essential for physiological processes like cardiac function, propagation of action potential and muscle contraction [40, 41]. Ion channels arguably provide the most effective and controlled way of allowing various ions to cross the protective membrane. The two key functions governing their ubiq-

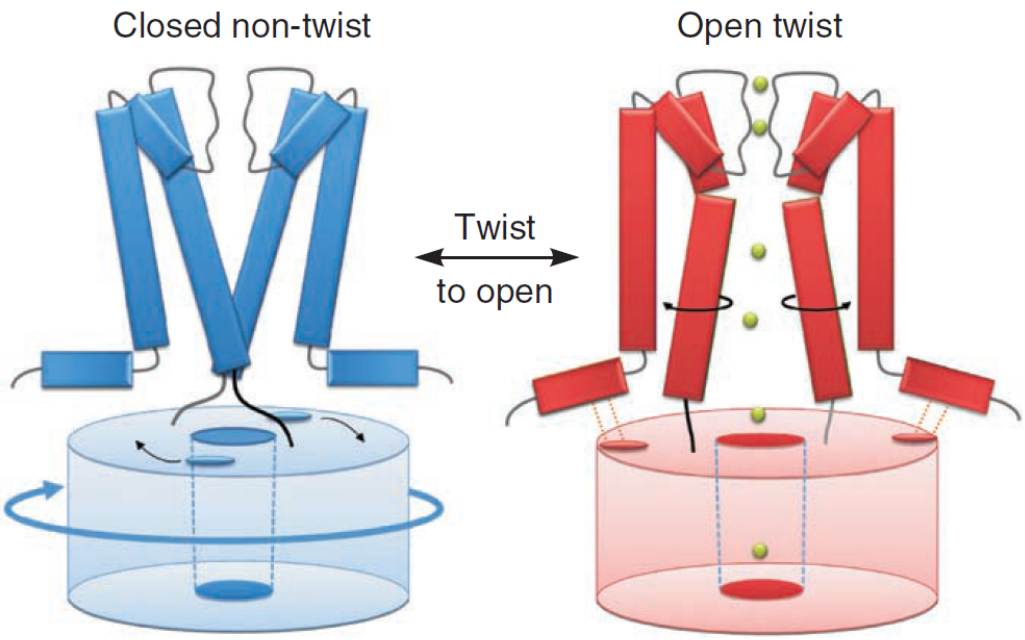


Figure 1.6: Example of conformational changes leading to opening and closing of a KirBac3.1 potassium channel. Reproduced from [44]

uitous involvement in physiological processes are selectivity and gating. The vast majority are selective for specific ions such as potassium, sodium, calcium or chloride. There are over 90 genes coding for subunits of potassium channels and their abundance in all human organs makes them an important drug target. Potassium channels are selective against sodium ions by factor of 10000 [42]. Given that both carry the same charge, discrimination can only be based on size. Comparing the size of potassium ions (1.33 Å) to sodium ions (0.95 Å) gives an indication of the elaborate and finely tuned function of the selectivity filter. This unit ensures that only specific ions can cross the channel while maintaining high rates of conduction at the same time [43]. In order to control an appropriate ion concentration and the transmembrane voltage in the cell, ion channels open and close depending on various stimuli such as voltage or ligand binding [2]. Voltage-gated channels are essential for creating electrical impulses and therefore regulate physiological processes such as nerve signalling and cardiac function [42]. Selectivity and gating are inherently

linked to protein structure. The amino acid sequence forming the selectivity filter of K^+ channels is a highly conserved structure among all types of potassium channels. Conformational changes of channel subunits govern the gating process by changing the diameter of the pore and thereby modulating it between open and closed states. Despite the intimate connection between structure and function, it is experimentally challenging to clearly relate them to one another. The reason for this lies in the nature of the techniques used to characterise both. X-Ray crystallography is a powerful tool that has been used to solve the 3D structure of channels and proteins in general. On the other hand, patch-clamping is the de facto technique that allows the measurement of picoampere currents through single channels and their gating characteristics by trapping a small portion of cell membrane with a glass pipette. The static nature of crystal structures and the dynamic nature of patch-clamping makes a combination of both impossible [45]. However, novel approaches using optical single-channel recordings, potentially combined with FRET to probe channel conformation might provide a solution to what has been termed the holy grail of ion channel research [46]. Optical channel recordings are a major focus of this thesis and will be explained in more detail in the next section.

1.3.2 Electroporation

The previous section introduced ion channels which allow permeabilisation of specific ions through the membrane. This happens in a controlled way since ion channels are selective and respond to distinctive stimuli. Another way of cell permeabilisation is through electroporation. Early experiments with BLMs showed that membranes are unstable above a voltage threshold ranging between 150-500 mV [47, 48, 49]. While the exact mechanism remains somewhat unclear it was shown that the specific rupture potential is dependent on the type of lipids, the concentration of the electrolyte in solution and also the duration of an electric pulse [50]. Furthermore,

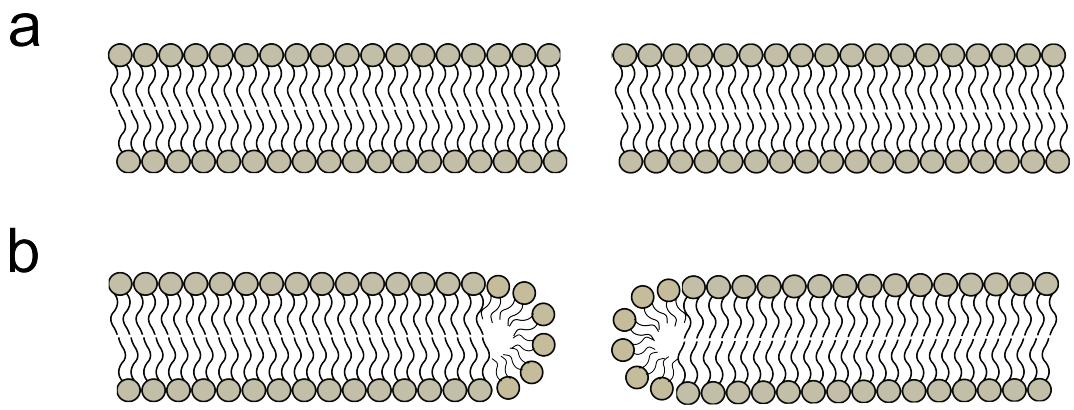


Figure 1.7: The toroidal pore model of electroporation proposes a transition between a **(a)** hydrophobic pore with exposed tail-groups and **(b)** hydrophilic pore with polar head-groups along the pore region

an increase in permeability was shown in vesicle membranes with an applied electric field resulting in electrolyte efflux through electropores [51]. The permeability of electropores is however not restricted to small salt ions but was also observed for larger molecules such as sucrose [52] and calcein [53]. Until rupture, electropore formation is a reversible process and a categorisation into 5 stages has been suggested [54]: During the initial *Trigger* stage, the voltage difference between the membrane reaches a critical value above which permeabilisation starts. This is followed by *Expansion* while the applied electric field is above the critical value. As soon as the field is subcritical, the membrane goes through a *Stabilisation* stage characterised by a decrease in conductivity which is followed by *Resealing*. During this stage the leakage of membranes gradually decreases and eventually disappears. Depite the reversibility of this process there seems to be a *Memory* stage where alterations to membrane properties were present for minutes or hours after resealing.

Electroporation has become an established technique in medical sciences and biotechnology. It is used to introduce foreign molecules such as DNA into cells by forming pores in their membrane and thus rendering it permeable [55, 39]. There are several theoretical descriptions of electroporation which can be broadly categorised into pore-forming and non-pore-forming models. Theories that do not involve the

formation of pores take a deterministic approach to calculate the critical transmembrane voltage based on compression of the membrane due to the electric field. Pore-based models are more accepted, because they incorporate the the stochastic nature of membrane rupture [56]. A prominent model is the toroidal-pore model which describes pore formation as a transition between a hydrophobic pore, with lipid tails exposed to water, to a hydrophilic pore where lipid head-groups face water molecules and line the pore region (see Fig.1.7). The basic model assumes that the generation of a pore is governed by the balance between an increase in energy due to line tension and a decrease in energy due to surface tension [50]. The presence of an applied potential lowers the energy barrier even further, therefore increasing the pore formation probability. Extended and more advanced theories of electroporation have been developed and can be found in the literature (see e.g. Neu and Krassowska [57] and Lewis [58])

1.3.3 Antimicrobial peptides

Antimicrobial peptides are vital components of the innate (non-adaptive) immune system. Since only vertebrates have an adaptive immune system they are key agents of bacterial defence for a broad range of organisms. The existence of antibacterial agents has been known since the late 19th century without any detailed knowledge about their structure or mode of action. Early discoveries of specific molecules include gramicidin [59] and Alexander Fleming's study on the antimicrobial effect of lysozyme [60]. The discovery of new AMPs has increased dramatically over the past 40 to 50 years and there are now more than 2000 identified AMPs in the Antimicrobial Peptide Database [61]. There is some variantion with regard to chain length and charge but the majority of AMPs are composed of 10-60 amino acids and mostly carry positive net charge (see Fig.1.8).

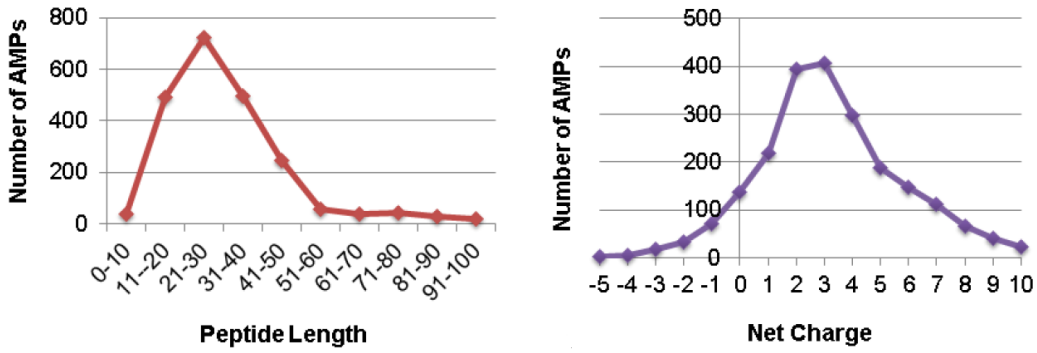


Figure 1.8: Distribution of AMP chain lengths and net charge. Reproduced from [61]

AMPs specifically target bacterial membranes and their functionality exploits a key difference between both types of membranes, namely the presence of negatively charged phospholipid headgroups in bacterial cell membranes [38]. Due to positive net charge, AMPs molecules can bind to negatively charged lipids through electrostatic interactions. AMPs usually have an unstructured conformation when in aqueous solution. In a membrane environment, they can fold into secondary structures, most commonly they exhibit α-helical, β-sheet or extended conformations [62]. Particularly for α-helical AMPs, there is a distinct segregation into positively charged and hydrophobic regions. It is generally believed that the amount of net positive charge indicates stronger preference for bacterial membranes and therefore higher bactericidal activity [63]. While charge seems to be essential for recognition and binding to negatively charged lipids, the hydrophobic areas are thought to promote insertion and pore formation. In this situation, hydrophobic residues would be oriented towards the fatty acid chains in the lipid bilayer [64]. The membranes of mammalian cells are composed of zwitterionic lipids, predominantly phosphatidylcholine (PC), phosphatidylethanolamine (PE) and sphyingomyelin [63, 65]. In order for AMPs to function as part of the mammalian immune system, it is essential that native cells are not targeted. Several AMPs, however, do interact with neutral membranes and even permeate them. Toxins and venoms such as melittin show relatively

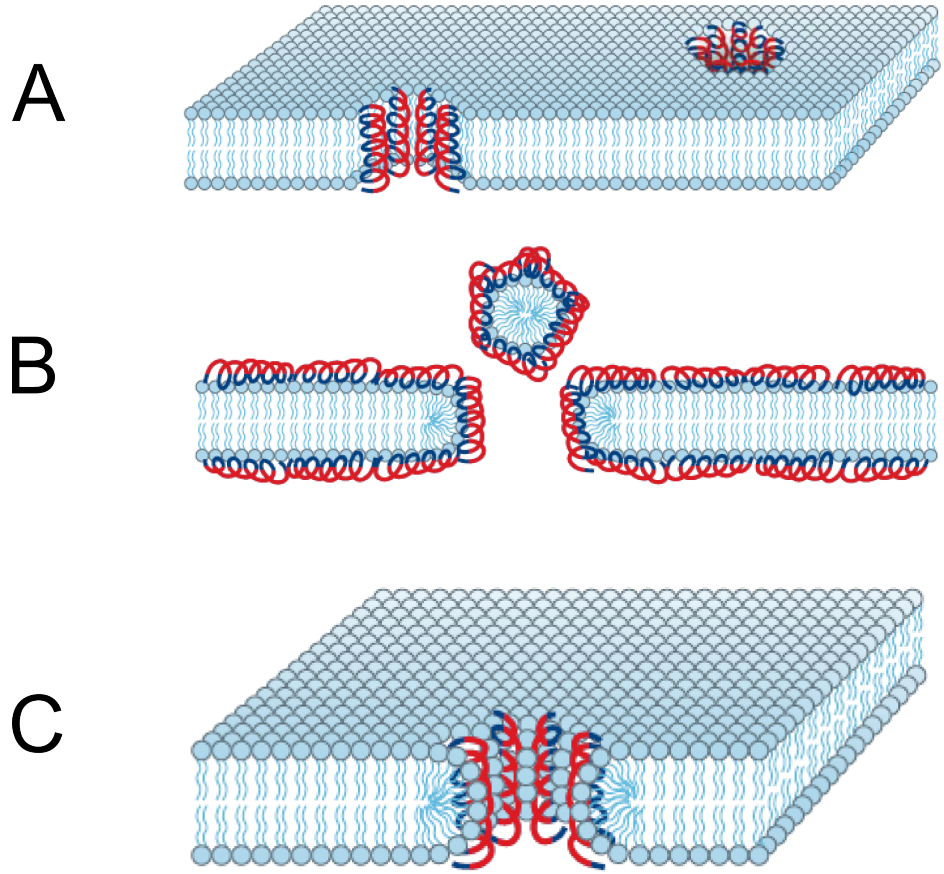


Figure 1.9: Illustration of a) Barrel-Stave model b) Carpet model and c) Toroidal-Pore model. Reproduced from [67]

high affinity for PC bilayers [66].

Several studies have shown that various AMPs cause channel formation or some degree of permeability in targeted membranes [68]. Alamethicin is an archetypical example of a voltage-gated pore with distinct conductance levels, indicating the presence of transmembrane helices [69, 70]. Channel formation has also been observed for melittin in experiments with model membranes [71]. For magainin, an increase in membrane conductivity was observed and circular dichroism showed the presence of two distinct orientations when interaction with a bilayer [72, 73].
Despite the vast evidence for selectivity and channel formation of numerous AMPs, the exact mode of action for cell penetration remains unclear. While it is gener-

ally accepted that some form of cell lysis take place in order to induce permeability, the details have remained somewhat elusive. There are mainly three proposed mechanisms for pore formation that are used to categorise AMPs and explain their interaction with lipid membranes [67, 68]. All models suggest initial binding to the surface of the membrane followed by secondary interactions. An illustration of all three models is shown in Fig.1.9.

1. **Barrel-Stave model**

   This model is mostly applicable to alamethicin which exhibits distinct conductance levels and channel-like behaviour. A pore formed of several monomers sits in the bilayer with hydrophobic parts facing the lipid core region. The hydrophobic regions make up the interior part of the pore.

2. **Carpet model**

   In this scenario, a high density of peptides bind to the surface of the membrane forming a carpet-like structure. Above a critical concentration, peptides disintegrate parts of the membrane similar to detergents and breaks it into small pieces. Membrane permeation is believed to occur without formation of channels.

3. **Toroidal-pore model**

   For this model it is hypothesised that peptides insert into the bilayer but do not form a tight, channel-like structure. The centre of pore is lined with both the polar peptide regions and lipid head-groups that are arranged along the aqueous pore.

Apart from pore-forming models, there are also proposed mechanism for intracellular killing. Indolicidin, for example, can cross the membrane without lysing it. Instead of affecting the bilayer structure it inhibits DNA synthesis and induces filamentation in *E.coli* cells [74]. Further means of intracellular killing include inhibition of

cell-wall synthesis and inhibition of enzymatic activity [67].

It should be noted that more generalised detergent-like models of pore formation have been proposed to unify the carpet and toroidal pore model suggesting they are manifestations of the same mechanism [75].

There is a pressing problem regarding antibiotic resistance resulting in an immediate need for alternative treatment approaches. AMPs are potential candidates due to their selectivity for bacterial membranes. Changing the composition of phospholipids in the membrane would be a costly process for bacteria and developing immunity against AMPs is therefore more difficult [76]. In the context of AMP resistance, a study demonstrated the successful synthesis of antagonists which are able to inhibit AMP function [77]. Clinical trials on several potential peptide based drugs are currently being carried out [78]. Unfortunately there have also been setbacks in the past where development of ongoing products has been discontinued (e.g. plectasin or pexiganan)[79]. While the propects for AMPs as antibiotic drugs are promising, it is essential to gain a more elaborate understanding of pore-forming and cell killing mechanisms. In this thesis, four representative AMPs are investigated to elucidate the binding locations in the membrane and image the location of conductive pores.

1.4 Single-channel recording techniques

For the understanding of ion channels and membrane pore function, it is important to have sensitive and high information content techniques that can resolve single channels. Due to the small scale of channel and pore currents (typically pA) this is not an easy task. Whole cell configurations monitor the sum of currents through all channels in a membrane without giving information on individual channels. Channel gating and pore formation are stochastic processes and the stochastic nature can only

be fully characterised with single-channel resolution. Furthermore, identification and screening of channel blockers is much more efficient when monitoring single channels. For several decades, patch clamping was the only method available and is still widely used today. Efforts towards higher throughput and scalability of channel recordings have raised interest in optical screening methods where currents are detected by means of ion-specific indicator dyes. Both techniques will be discussed in this section.

1.4.1 Patch-clamping

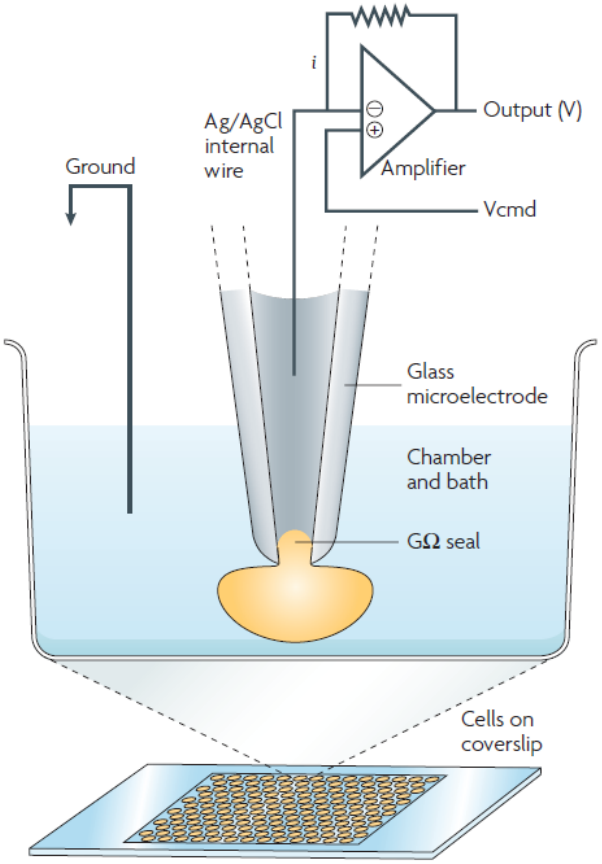


Figure 1.10: Schematic of a patch-clamp setup. A glass pipette creates a GΩ seal around a membrane area. Currents through single-channels in the encapsulated area are recorded by means of an attached electrode. Reproduced from [80]

Developed by Neher and Sakmann in the 1970s, patch-clamping has arguably

become the most powerful tool for single-channel studies. Their first report was the observation of single acetylcholine receptor currents obtained from frog muscle fibres [81]. In order to isolate single channels, a glass pipette with a diameter of a few micrometers is used to encapsulate small patches of a membrane (in many cases xenopus oocytes). When applying suction to the glass pipette, a tight giga-ohm seal with the membrane can be achieved so that background noise is reduced which is crucial to resolve channel currents on a scale of picoamperes. This setup also allows manipulation of the membrane potential [82, 83]. There are several modes of patch clamping that can be applied. The whole-cell configuration allow measurement of channel contributions from the the entire cell. This is achieved by rupturing the a membrane patch of a cell while maintaining the electric seal. In the cell-free configuration, selected membrane patches are removed from the cell and remain encapsulated in the pipette. The advantage of this variant is control of ionic solutions on both sides of the channel which is not possible whith the membrane attached to an entire cell [84].

While traditional patch-clamping is a powerful method, it is low in throughput and requires highly skilled and trained staff. In the context of drug discovery and ion channels as potential targets, screening methods which are able to record a large amount of channel data are highly desirable. When considering that a single Patch-Clamp experiment can only record one channel or a whole cell at a time, it becomes clear that this setup is limited in terms of data acquisition. The demand for high throughput methods has led to development of automated and parallelised electrophysiology techniques [80, 85].

1.4.2 Channel recordings in model membranes

Being able to study proteins in their natural environment without any purification is a major advantage of single-channel recordings in cells with patch clamping.

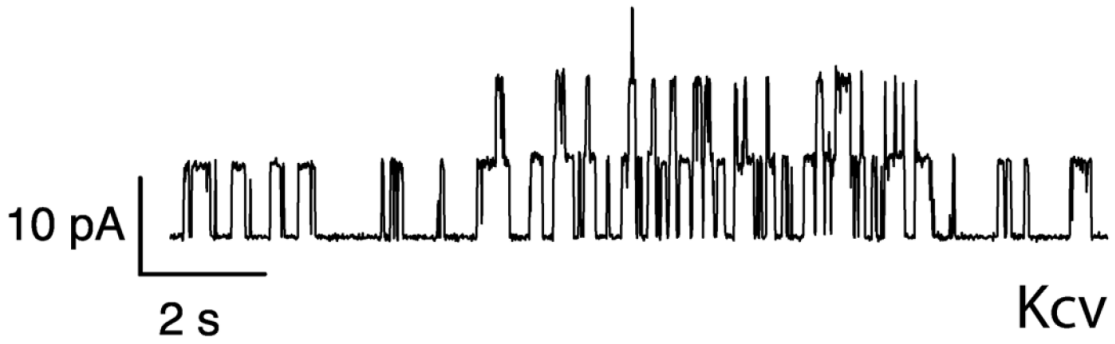


Figure 1.11: Single-channel recording of Kcv obtained by reconstitution into droplet interface bilayer. Reproduced from [32]

However, model membranes have also been used extensively for electrophysiological studies. The relative simplicity of their production and the ability to incorporate reconstituted channel proteins while removing unwanted components makes them an important alternative. BLMs have been described earlier in this chapter. Several ion channels and peptides have been characterised in this in vitro environment. They are particularly attractive for proteins which can be readily purified or synthesised. Examples include magainin I [86], magainin 2 [87], melittin [88], gramicidin [89], OmpA [90].

More recently, electrical recordings have been conducted in droplet interface bilayers with various reconstituted proteins such as α-hemolysin, KcsA, OmpG,Kcv [35, 91] (see Fig1.11), alamethicin [92] and bacteriorhodopsin [93] . Several reconstitution protocols have been reported for the DIB system [94].

1.4.3 Optical single-channel recordings

Despite advances in automated patch-clamping and the relative simplicity of channel recordings with model membranes, neither method is particularly suited for large-scale screening which is desirable for drug development. Optical measurements of

ion flux have become a powerful alternative to patch-clamping when studying the functional properties of ion channels [95, 96, 97]. The simultaneous read-out of optical single channel recordings (oSCR) provides an alternative way of measuring electrical activity and is more feasible than parallelising electrical measurements. Channel activity is monitored with ion specific indicator dyes whose response is proportional to the magnitude of the current. Recording the fluorescence profile over time yields traces that are analogous to single-channel electrical recordings. Especially over the past 10-15 years oSCRs of Ca^{2+}-flux have given valuable insight [98, 99], but an early successful combination of Ca^{2+} flux imaging and patch-clamping dates back to 1988 [100]. A method called 'optical patch-clamping' was introduced by Demuro and Parker [101] and showed hundreds of simultaneous calcium-flux oSCRs through voltage-gated Ca^{2+} channels with a temporal resolution of 2 ms. The same technique was used to image calcium-flux through Aβ peptide pores, which disrupt the membrane structure and play an important role for Alzheimer's disease [102]. While optical calcium flux experiments are usually performed in cells or oocytes, optical assays using droplet interface bilayers (DIBs) to image currents through, for example, α-hemolysin pores are a promising alternative [97]. Simultaneous optical and electrical measurements of α-hemolysin were also performed in DIBs showing a direct correspondence between current and fluorescence signal [33]. DIBs provide a controlled environment where parameters such as salt and lipid concentrations as well as lipid type can easily be varied. Furthermore, bilayer arrays have been used for parallel and multi-channel monitoring of ion current through several nanopores, thus carrying the potential of increasing through-put for ion channel and drug screening measurements [103].

Two main advantages over patch-clamping have raised interest in imaging methods. First of all, optical methods enable parallel readouts of single channel data, thereby drastically increasing statistics of measurements. Traditional patch-clamping only

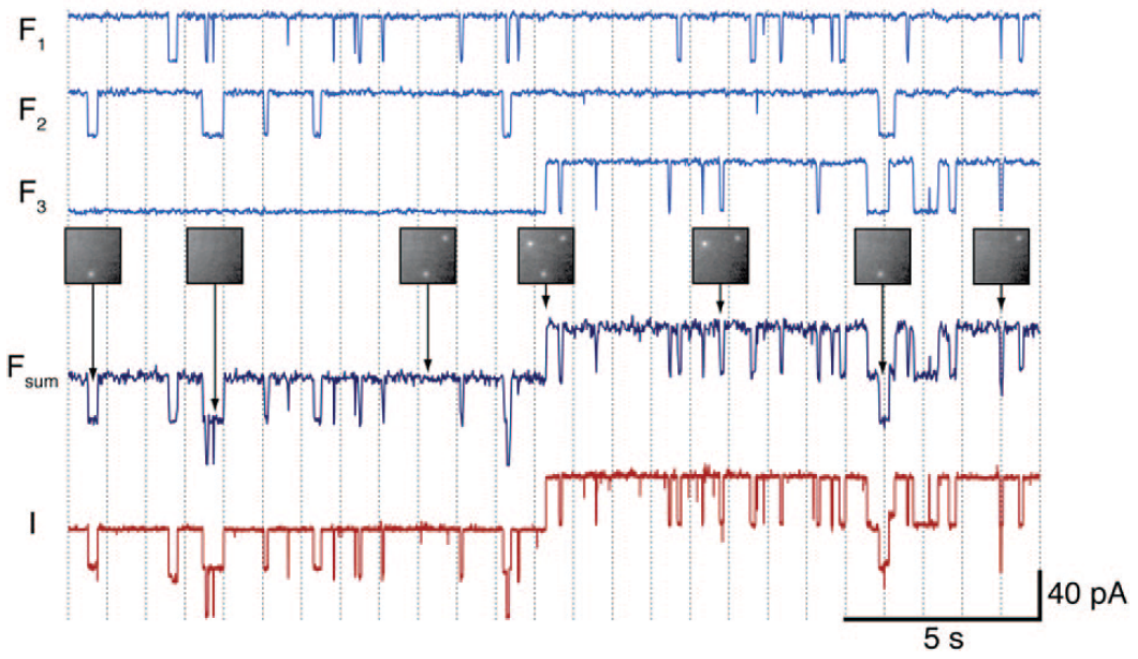


Figure 1.12: Example of optical single-channel recording through α-hemolysin pores. The fluorescence from calcium-flux through three individual pores is monitored. The sum of all fluorescence signals is equivalent to the overall electrical current going through the bilayer. Reproduced from [33].

allows recordings of one single-channel at a time or multiple channels combined. Furthermore, imaging contains spatial information on the distribution of channels within the membrane, as well as their motility over time. Compared to patch-clamping, imaging is also less invasive.

As mentioned previously, linking the function of channel proteins to structural changes has been experimentally challenging. This is however very important to determine the structural elements that are essential for channel gating. Ion channel structures can be determined through X-Ray crystallography down to atomic resolution and functional studies are accessible through patch-clamping [104]. The combination of these particular techniques is clearly impossible. Novel approaches to monitor structural changes involve fluorescence resonance energy transfer (FRET). When labelling specific cysteine residues in a protein of interest with an acceptor and

a donor dye, changes in the distance between both cause an increase or decrease in fluorescence of the acceptor dye. This can be taken down to single-molecule level to observe conformational changes of individual molecules [105]. Therefore the combination of simultaneous single-molecule imaging and optical single-channel recordings would provide a link between dynamic changes in structure and function. A study on gramicidin channels achieved the combination of FRET and electrical measurements and established a correlation between the two [106]. It does however remain challenging to show a one-to-one relationship between a fluorescence and electrical signal on a single-molecule level because this would essentially require the incorporation of only one channel into a bilayer. If the current were monitored by optical single channel recordings, the combination with FRET measurements would become more feasible and scalable. Many channels inserted in one bilayer could be imaged in parallel and one could still extract single-molecule information. The FRET signal would show conformational changes while oSCRs provide the electrical activity [46, 45].

1.5 Summary

Imaging the electrical activity of both ion channels and pores is important for questions regarding their structure and function but also the nature of pore formation and their location in membranes. This thesis highlights two novel applications of oSCR:

Chapter 3 will explore an extension of ion-flux imaging to potassium which has so far not been realised. Three potassium indicator dyes are tested with in-depth analysis carried out for APG-4. The limitations of this method will be discussed

and suggestions for improvements of potassium indicator dyes will be provided.

Chapter 4 will investigate pore formation of the four AMPs magainin 2, melittin, indolicidin and alamethicin. Electrophysiological characterisation of all peptides will show their interaction with the membranes in the DIB system. Using calcium-flux imaging, pore formation is visualised while also determining the distribution of labelled peptides around the pore region and on the membrane surface to test the validity of proposed pore forming mechanisms.

Chapter 2

Experimental techniques

The experimental techniques applied in chapters 3 and 4 will be described in this section. The detailed conditions will be outlined in the respective chapters, whereas this chapter focuses on a general description of the experimental setup and methods.

2.1 Materials

All lipids used in this thesis (DPhPC, POPE, POPG and CL) were purchased from Avanti Polar lipids (Birmingham/Alabaster, AL, USA). The potassium indicator dyes APG-2 and APG-4 and the calcium indicator dye Fluo-8 were purchased from Teflabs (Austin, Texas, USA). KS2 was obtained from Xianfeng Zhou (Center for Biosignatures Discovery Automation, Biodesign Institute, Arizona State University, Tempe, Arizona 85287, United States). The AMPs melittin, indolicidin and magainin 2 were labelled with tetramethylrhodamine (TAMRA) and custom-made by LifeTein (Somerset, NJ, USA). Unlabelled peptides were purchased from Bachem (Bubendorf, Switzerland). Labelled alamethicin was synthesised by a collaborator from the Darren Dixon group (Department of Chemistry, University of Oxford). Unlabelled alamethicin was purchased from Sigma Aldrich. Unless stated otherwise,

the remaining materials were purchased from Sigma Aldrich.

2.2 Droplet interface bilayers

The model membrane system used in all experiments are Droplet Interface Bilayers (DIBs) on a hydrogel support. It has been developed since 2007 and several reports have been published [35, 34, 32, 107, 94] . Simultaneous optical and electrical recordings are essential for all the experiments carried out in this thesis and this technique allows imaging of a supported bilayer formed on a coverslip. Electrical recordings can be performed by inserting Ag/AgCl electrodes into individual lipid coated droplets that have formed bilayers on the substrate.

2.2.1 Device fabrication

DIBs are prepared using a CNC micro-machined 16-well PMMA (Poly- methyl methacrylate) device shown in Fig.2.1. Each of the 16 wells can hold one droplet and therefore one bilayer which can be imaged through a cover-slip placed at the bottom. The holes at the side are used for filling with agarose buffer and also to hold the ground electrode. A second electrode is inserted into a droplet from the top, therefore enabling application of a voltage across the bilayer. Prior to bilayer formation, droplets are incubated in lipid solution. Each incubation chamber can hold roughly 8 droplets.

2.2.2 Lipid stock preparation

Potassium-flux imaging experiments are carried with DPhPC, and for AMP experiments a ternary mixture of 69:29:2 (mol%) POPE:POPG:Cardiolipin is used. DPhPC and POPE in powder form are each dissolved in chloroform to make up a solution of 25 mg/ml. POPG is dissolved in chloroform and methanol (1:1) and

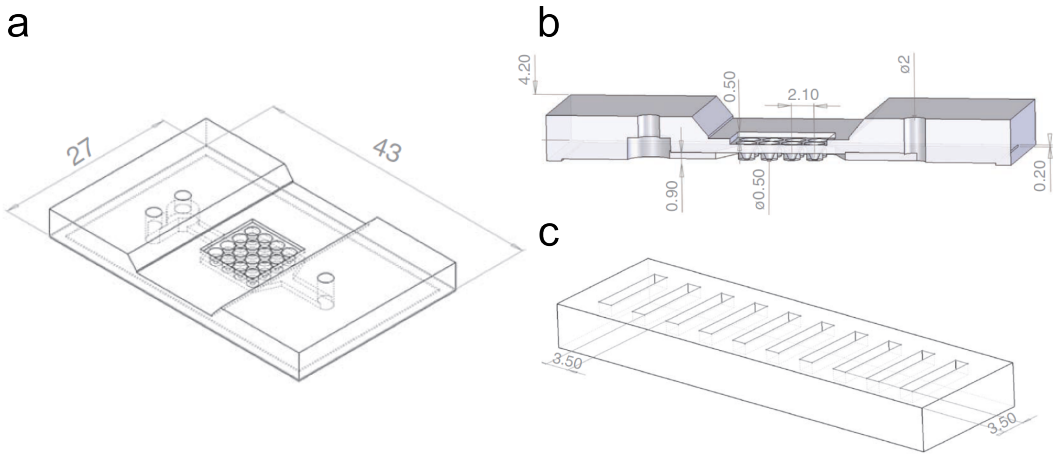


Figure 2.1: (a) PMMA device with 16 wells used to form DIBs (b) Cross-section showing the flow channel and groove to fit glass cover-slip (c) Incubation chambers for preparing aqueous droplets in lipid-in-oil solution to form monolayer coating. Reproduced from [34]

also made up to a concentration of 25 mg/ml. Cardiolipin is stored in chloroform at 10 mg/ml. All lipid stocks were stored at -20℃.

Lipid-in-oil solutions are made by drying down an appropriate amount of lipid solution from the chloroform stock under vacuum for at least 2 hours after preliminary drying under a gentle stream of nitrogen. DPhPC solutions are prepared to a concentration of 8.7 mg/ml in 95% hexadecane and 5% silicone oil AR-20. POPE/POPG/CL solutions are 3.5 mg/ml in hexadecane. All lipids are kept in Teflon-lidded glass vials.

2.2.3 DIB formation

The specific conditions for DIB preparation vary depending on the experiment, but the general procedure remains the same for all experiments carried out in this thesis:

1. To create a clean and hydrophilic surface, a 24 mm x 40 mm glass cover-slip (Gerhard Menzel, Braunschweig, Germany) is plasma cleaned (Femto Plasma cleaner, Diener Electronic, Ebhausen, Germany) for 8 min at 0.5 bar oxygen.

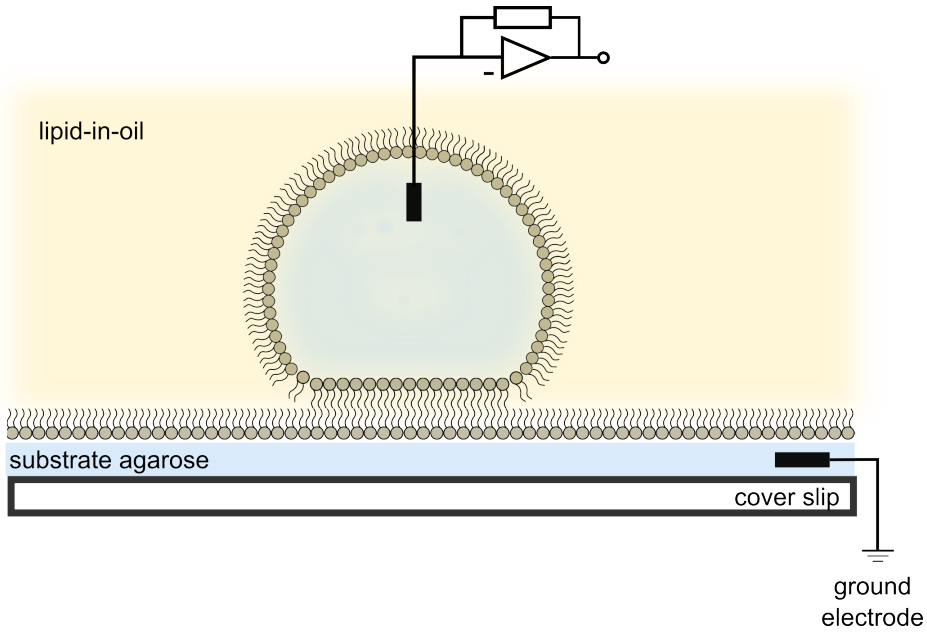


Figure 2.2: Sketch of a DIB formed on an agarose substrate together with setup for electrical recordings.

2. To allow lipid monolayer formation, a thin hydrophilic agarose-layer is created on the glass cover-slip. 0.75 % low-melting agarose is heated to 90℃ and 170 µL subsequently spin-coated (WS-650MZ-23NPP/LITE, Laurell, Pennsylvania, US) for 30 s at 4000 rpm

3. The spin-coated cover-slip is placed in the bottom groove of the PMMA device with the agarose layer facing upward. In order to prevent leakage and dehydration, the cover-slip is fixed and sealed with adhesive tape

4. 'Re-hydrating' agarose buffer is heated to 90℃ and 200 µL is filled into the PMMA device through a hole at the beginning of the flow channel.

5. The ground electrode is placed into one of the centre holes while the remaining holes are sealed with tape. The inserted electrode is sealed with vacuum grease.

6. 70 µL lipid-in-oil solution is spread around the centre of the PMMA device to fill each of the 16 wells

7. 30 µL lipid-in-oil solution is applied to one of chambers of the incubation device. 100 nL droplets are inserted to allow formation of a lipid monolayer coating around the droplet.

8. After 30 min incubation time, individual droplets are inserted into each well.

9. When using 95% hexadecane and 5% silicone oil, bilayers from within minutes. When using 100% hexadecane, the PMMA device is heated for 10 min at 50 ℃ to facilitate bilayer formation.

2.3 Electrical recordings

Electrical recordings can be performed parallel to optical measurements with the DIB system. This is essential when correlating optical measurements of ion flux to electrical currents through the membrane. The DIB system described in the previous section allows illumination of the bilayer region through a coverslip at the bottom of the PMMA device. At the same time, the transmembrane voltage is controlled with an applied protocol and electrical currents are recorded which requires the DIB system to be shielded by a Faraday cage.

Electrical recordings are used for all experiments in chapter 3 and chapter 4. In chapter 3, parallel electrical and optical experiments are required to image potassium flux through conductive electropores which form in the membrane above a voltage threshold. In the first part of chapter 4, electrical studies without imaging are used to characterise the electrophysiological properties of AMPs and their influence on bilayer stability. The second part of chapter 4 combines calcium-flux imaging through pores formed by AMPs with single-molecule imaging of labelled AMPs. The procedure for setting up electrical recordings is the same for all experiments and consists of the following steps:

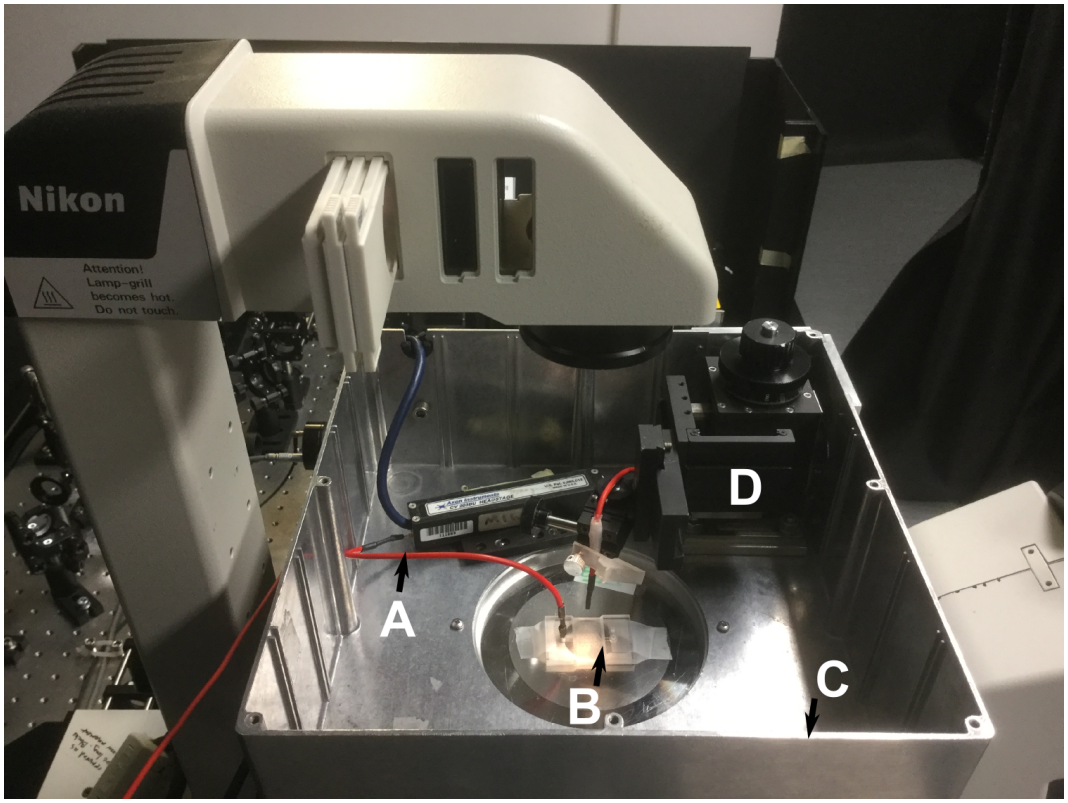


Figure 2.3: Picture of the setup for electrical recordings on a microscope stage. **(A)** Electrode connected to a head-stage **(B)** PMMA device placed above the objective **(C)** Faraday cage to reduce noise of electrical signal **(D)** Micromanipulator to control position of electrode

1. Once bilayers have formed, the PMMA device is fixed on a stage insert and mounted in a Faraday cage that is placed on a microscope stage. A hole is present at the bottom of the cage above the microscope objective to allow imaging.

2. Two Ag/AgCl-coated electrodes are required for electrical recordings. The ground electrode is fixed in the substrate agarose of the PMMA device. The second electrode is mounted on a micro-manipulator and initially place above the well containing the droplet bilayer of interest. Both electrodes are connected to a head-stage within the Faraday cage. The head-stage is externally connected to a patch-clamp amplifier (Axopatch 200B, Molecular Devices).

3. The second electrode needs to be inserted into the droplet to apply a voltage across the bilayer. Prior to inserting, the tip of the electrode is dipped into 0.75% agarose dissolved in MilliQ water.

4. The lid of the Faraday cage is closed to ensure shielding from external fields. The electrical noise is typically reduced to 10 pA, depending on the bilayer surface area.

5. With the help of white-light microscopy, the electrode is place centrally above the bilayer using external control wheels of the micro-manipulator. The electrode is subsequently lowered until inserted into the droplet. The position of the bilayer can be changed by moving the electrode in x-and y- direction. The bilayer area can be controlled by adjusting the z-position.

6. Electrical recordings are digitized (National Instruments BNC-2090) and processed using WINEDR (Strathclyde Electrophysiological Software, courtesy of J. Dempster, University of Strathclyde, UK). Voltage protocols are created in WINEDR and data acquisition is triggered by the EMCCD camera when performing parallel electrical and imaging experiments.

7. For the purpose of data analysis, WINEDR files are converted to text-files.

2.4 Fluorescence spectroscopy of potassium indicator dyes

Fluorescence occurs when light of a certain wavelength is absorbed by a molecule which subsequently emits light at a higher wavelength.The photons of the absorbing light elevate electrons from the vibrational ground state into an excited state with higher energy. Through internal conversion, electrons usually relax into the lowest

level of the excited state. When returning to the ground state, a photon is emitted at a wavelength that corresponds to the energy difference between both states. The energy of the emitted photon is lower and thus has a higher wavelength (Stokes-shift). Fluorescence lifetimes are on a scale of 10^{-9} s, because transitions happen between singlet states, which are allowed due to spin-pairing of electrons with opposite spins. In contrast, transitions from a triplet state are suppressed and have longer life-times which is known as phosphorescence [108]. The ratio of the number of emitted photons to the number of absorbed photons is called the quantum yield and defined as

$$Q = \frac{\Gamma}{\Gamma + k_{nr}}$$

where Γ is the emission rate of the fluorophore and k_{nr} is the rate of non-radiative decay to the ground state S_0 [108].

Fluorescent indicator dyes are available for a variety of different ions such as calcium, potassium, sodium and magnesium [96]. They are based on the principle that an ion chelating unit (typically crown ethers or cryptands) is attached to a fluorescent dye. Binding to respective ions results in intramolecular charge transfer thereby increasing the amount of electrons that can be excited. Hence, a higher quantum yield of the fluorophore is achieved resulting in an increase in fluorescence. It is therefore an optical method to measure the presence and concentration of specific ions. In order to develop a method to enable potassium-flux imaging, the bulk characterisation and optimisation of available indicator dye properties is an essential preparation for subsequent experiments in DIBs. Fluorescence spectroscopy is used in chapter 3 to determine ion selectivity and fluorescence response of the three potassium indicator dyes APG-2, APG-4 and KS2 by titration with various salt solutions. A Varian Cary Eclipse Fluorescence Spectrophotometer (Agilent Technologies, Stockport, UK) is used for all measurements.

2.5 TIRF Imaging

The imaging carried out it this thesis requires visualisation of pore formation and single-molecules in a lipid bilayer. Total Internal Reflection Fluorescence (TIRF) microscopy is an established technique that enables the illumination of a small nanoscopic layer of a solution as opposed to epi-fluorescence where the entire sample volume is excited [109]. Imaging only a region of 100 - 200 nm considerably increases the signal-to-noise ratio and therefore allows resolution of the point-spread-functions from fluorescence of single molecules. Similarly, fluorescence from potassium indicator dyes is localised around pore regions at the membrane surface and visualisation also requires a narrow region of illumination.

When a light beam propagates through a medium with refractive index n_2 (e.g. glass) and encounters a planar surface with a medium of lower refractive index n_1 (e.g. water), the critical angle is given by

$$\theta_c = \sin^{-1}(n_1/n_2)$$

Below the critical angle, the incident beam is refracted at the interface according to Snell's law. For incident angles greater than the critical angle it is however totally internally reflected. For this to take place, it is required that $n_2 > n_1$. Although the entire light is seemingly reflected, an evanescent component of the EM radiation emerges parallel to the interface and penetrates into the medium. This wave decays exponentially and the intensity dependent on the perpendicular distance z is given by

$$I(z) = I(0)e^{-z/d}$$

where

$$d = \frac{\lambda_0}{4\pi}\left(n_2^2 \sin^2\theta - n_1^2\right)^{-1/2}$$

and λ_0 is the wavelength of the incident light in vacuum. The penetration depth typically does not reach beyond 100 nm which makes it suitable for imaging of DIBs [110]. Application of TIRF with DIBs has been shown in several studies and will also be adapted in this thesis [33, 97].

2.6 TIRF microscopy setup

All imaging experiments were performed with a Nikon microscope using a Nikon 60x APO TIRF objective. Images are recorded with an Andor iXon Ultra 888 EMCCD camera. The laser alignment and illumination are different for potassium-flux imaging experiments and dual-colour imaging of pores and AMP molecules. The specific setups are described separately in the following sections.

2.6.1 Potassium flux imaging

The potassium indicator dyes APG-2 and APG-4 are both excitable with green light. Therefore, a green 532 nm laser (Coherent, Compass 215 M) is used for all experiments with potassium-flux imaging. The laser light is collimated before being focused onto an optical fibre (Thorlabs). The fibre optic setup couples to the microscope and enables an even Gaussian illumination. The beam is focused on the back aperture of a high numerical aperture objective (Nikon, Plan Apo TIRF 60x 1.45) after being redirected by a dichroic beam splitter (Semrock, FF 545/650). The position of the beam is adjusted such that total internal reflection occurs at the glass cover-slip and membrane interface, causing illumination of a thin layer approximately 100 nm deep. The emitted light passes through an emission filter (Semrock, 580/75) and is redirected into the EMCCD camera (Andor iXon Ultra 888, 20 Hz, 300 gain). All images are recorded at 50 Hz frame rate and EM gain 300. See Fig.2.4 for a schematic of the optics.

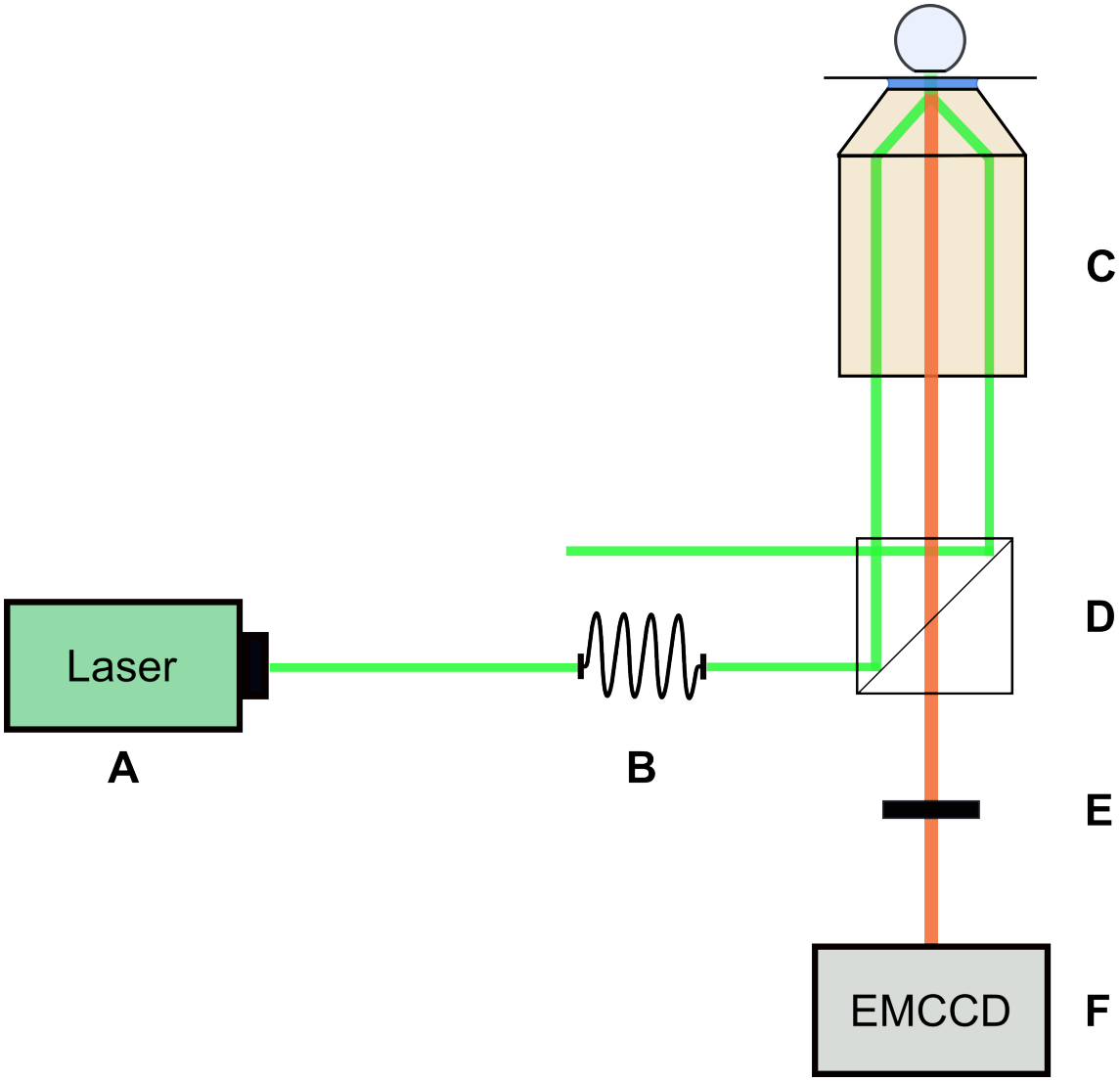


Figure 2.4: Schematic of the optics for potassium-flux imaging. **(A)** 532 nm green laser **(B)** Optical fibre that is launched directly into the microscope **(C)** 60x TIRF objective **(D)** Dichroic beamsplitter **(E)** Emission filter (580/75 nm) **(F)** EMCCD camera

2.6.2 Dual-colour imaging

In order to image calcium-flux through membrane pores and also track single AMP molecules, a dual-laser setup is used enabling sequential blue and green excitation.

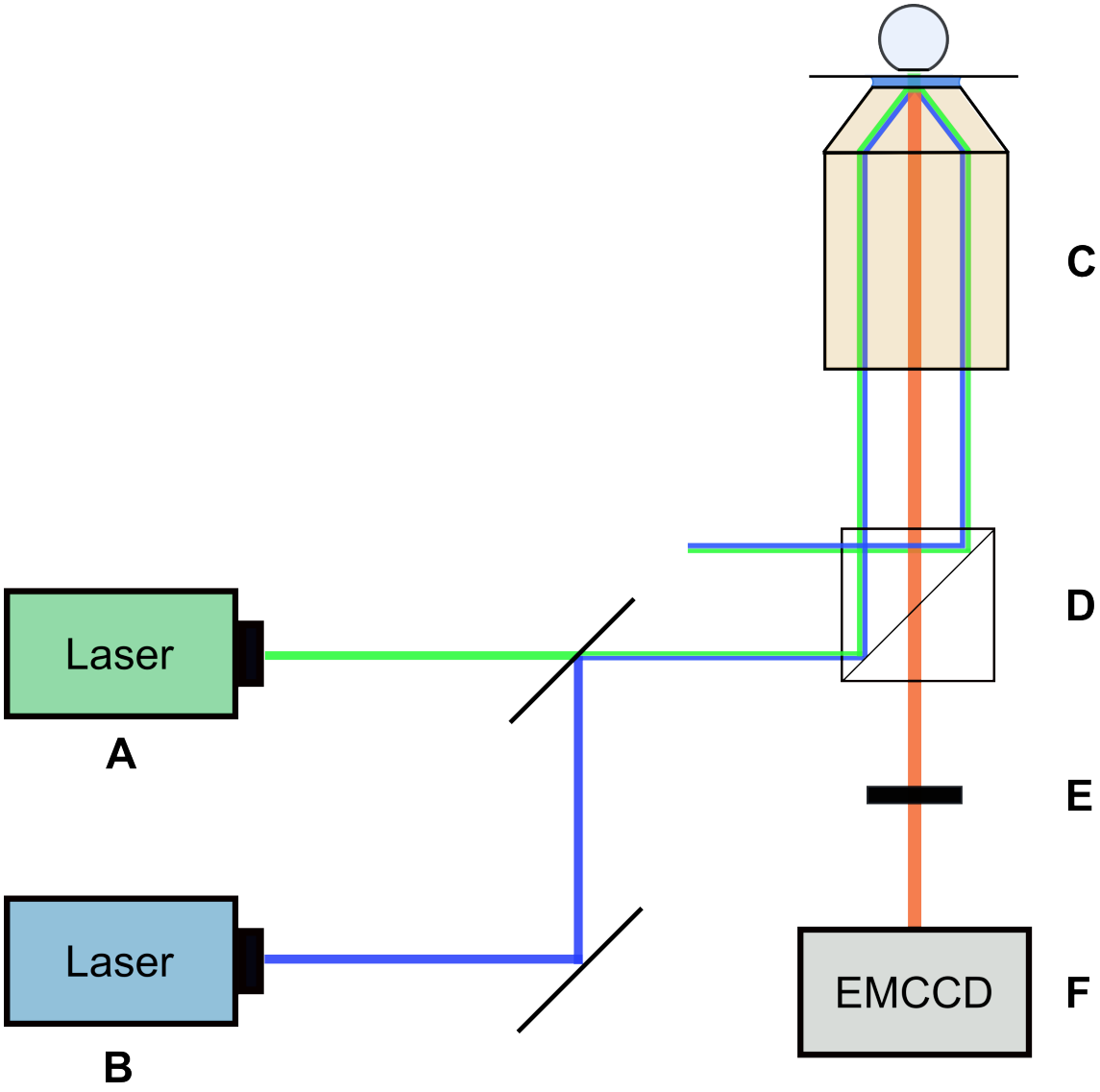


Figure 2.5: Schematic of the optics for dual-colour imaging for AMP experiments. **(A)** 532 nm green laser **(B)** 473 nm blue laser **(C)** 60x TIRF objective **(D)** Dichroic beamsplitter **(E)** Emission filter (580/75 nm) **(F)** EMCCD camera

Unless stated otherwise, the materials are from the same manufacturer as stated in the previous section. A 532 nm and 473 nm laser are combined on an optical path after collimation using a system of mirrors. After being launched into the microscope, the beams are reflected on a dichroic beam splitter and focused at the back aperture of a 60x TIRF objective. The light is totally internally reflected at the glass cover-slip and bilayer interface causing an evanescent wave illuminating up

to 100 nm of the sample. The emission light passes through an emission filter and is redirected into an EMCCD camera. All images are recorded at 50 Hz frame rate and EM gain 150.

In a separate experiment, a region of interest of the membrane is recorded using green excitation to monitor the positions of labelled AMPs while applying a sequence of voltages from 0 mV to -180 mV in steps of 30 mV. The acquisition setting are the same as before. See Fig.2.5 for a schematic of the setup.

2.6.3 Combined calcium-flux and single-molecule AMP imaging

Most oSCR have been preformed using calcium-flux imaging with individual optical channel events, sometimes also called SCCaFT (Single-channel Calcium Fluorescent Transients)[101]. Fluorescent calcium indicator dyes are very sensitive and exhibit a good combination of signal to background and binding affinity [111]. SCCaFT imaging in DIBs has been reported in several studies ([33, 97]) and a similar setup will be adopted for the imaging of pore formation by AMPs. The indicator dye Fluo-8 (Teflabs) was chosen due to its high selectivity for calcium and good dynamic response to calcium currents (K_d=290 nM for calcium binding). The calcium chelator EDTA is added for background reduction and also to control the size of the fluorescence signal around the pore region. In order to image the distribution of antimicrobial peptides around the pore regions, TAMRA labelled AMPs are TIRF imaged by switching from blue to green laser excitation once a pore has been identified.

Data acquisition is performed as follows: Using the patch-clamp amplifier, a voltage is applied such that pore formation is visible electrically. The applied potential varies according to respective AMPs. Once pores form, their location is identified

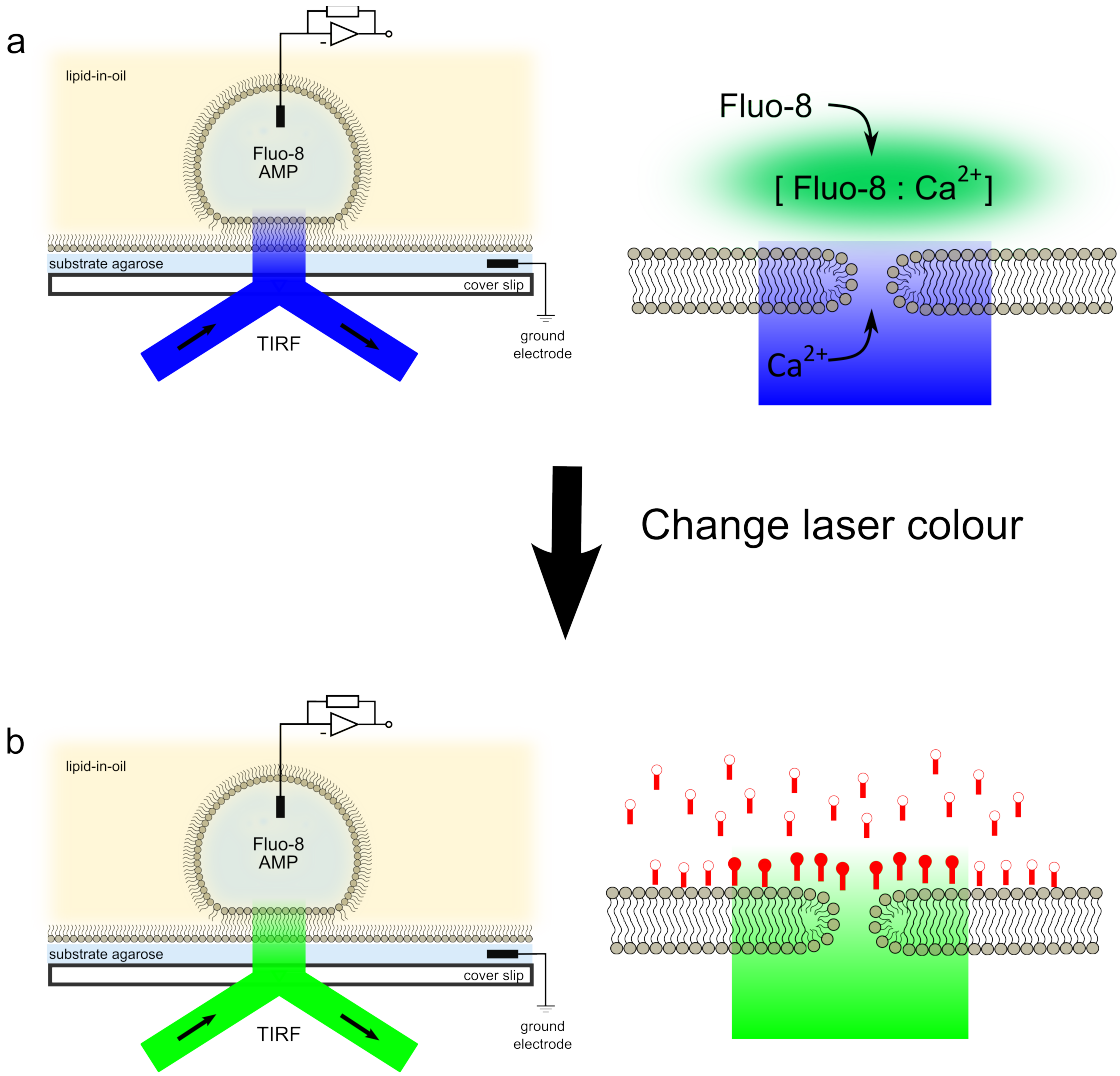


Figure 2.6: **(a)** Schematic of DIB imaging with TIRF. The bilayer region is excited with a blue laser. The substrate contains $CaCl_2$ buffer and the droplet buffer is composed of KCl, Fluo-8 and EDTA. When applying a voltage, pores form above a certain threshold and calcium ions are transported through the bilayer causing fluorescence **(b)** Once a pore has been identified, the laser colour is switched to green to imaged the location of peptides in the same region of the membrane.

with calcium-flux imaging using blue excitation. Image acquisition is subsequently started and around 500 frames showing pores in the membrane are recorded. While continuing the recording, the shutter of the blue laser is closed followed by opening the shutter for the green laser in order to image labelled AMPs in the region of

the previously identified pore. The relative intensity of TAMRA at 473 nm (blue) excitation is approximately 5% compared to the maximum excitation intensity at 550 nm (green). Therefore, no considerable photobleaching is expected from the blue laser during calcium-flux imaging which is done before switching to the green laser. At least 1500 frames are recorded with green laser excitation. This experiment is performed for the AMPs melittin, magainin 2, indolicidin and alamethicin. At least 5 datasets are collected for each AMP. A schematic of the sequential imaging procedure is shown in Fig.2.6

2.7 Gaussian fitting and single-particle tracking

For the purpose of identifying pore locations and the tracks of labelled AMPs, Gaussian fitting and a particle tracking program are used.

2.7.1 Gaussian fitting

Calcium flux through the bilayer causes a fluorescent spot around pore regions and in order to identify their locations, Gaussian fitting is used. The program is written in Igor Pro (Wavemetrics, OR, USA) and adapted from a program originally written by Jason Sengel. The procedure is based on the CLEAN algorithm [112] and involves the following steps:

1. A stack of images in TIF-format containing a recording of oSCRs is selected and opened in Igor

2. Once the file is loaded, three parameters need to be declared. The approximate radius of the fluorescence spot is specified in pixels. The intensity threshold above which the signal is considered to be from an oSCR is specified. Finally, a coverage area that is blanked out after fitting is specified, typically as twice

the radius of a fluorescent spot.

3. The pixel with highest intensity is selected and a 2D Gaussian is fitted to a region of twice the radius that was previously specified. The 2D Gaussian is

$$f(x,y) = Z_0 + A\exp\left[-\frac{1}{2}\left(\left(\frac{x-x_0}{\sigma_x}\right)^2 + \left(\frac{x-x_0}{\sigma_y}\right)^2\right)\right]$$

   The parameters $Z_0, A, x_0, y_0, \sigma_x$ and σ_y are determined by the fit. The centre of the 2D Gaussian is at (x_0, y_0) which is used for further analysis.

4. After fitting to one spot region, the previously determined coverage area around the spot is set to a value of 0, eliminating the fluorescence signal in that region.

5. All remaining spots above the specified intensity threshold are fitted by repeating the steps above.

All spot centre positions are saved for further analysis.

2.7.2 Single-particle tracking

The position and tracks of individual labelled peptides are computed with a program implemented in Matlab. The code was written and provided by Dr. Matthew Cheetham. The program is accessed by a Graphic User Interface (GUI) and the steps of the tracking process are as follows:

1. The GUI is opened in Matlab. To initialise the program, the frame time and pixel size of the dataset to be analysed are specified to initialise the program. The frame time is 20 ms and the pixel size is 270 nm for all experiments.

2. A dataset consisting of 1000 frames in TIF-format and containing fluorescence images of labelled peptides is loaded within GUI. Prior to executing the track-

ing algorithm, the following parameters are specified: Signal threshold, spot diameter, maximum linking distance, minimum track length

3. The signal threshold is determined in Trackmate using the preview function to ensure all spots are recognised. The approximate spot diameter is determined using the same preview function. The maximum linking distance sets the maximum distance in pixels between two frames that is considered to be part of one track. It is set to 5 pixels given that the spot diameter is 3 pixels and assuming that one spot does not move further than twice its diameter between two frames. The minimum track length sets the smallest possible length for a track in number of frames. It is set to 3 in order to exclude peptides that only bind to the bilayer for a short duration.

4. The tracking process is automated and initially calls the tracking program *Trackmate* which is implemented in Fiji, a distribution of ImageJ [113]. The detection algorithm uses a Laplacian of Gaussian (LoG) detector and all calculations are made in Fourier space [114]. The LoG is a standard method for spot detection [115]. A Gaussian filter is applied to the image for smoothing and a Laplacian (second derivative) is applied to enhance and detect edges [116].

5. Linking between spots to create tracks is carried out with a LAP (Linear Assignment Problem) algorithm. After determining all spot locations in each frame, spot locations between frames are linked using a cost matrix. The costs for all possible assignments are calculated initially and the actual tracks are obtained from minimising the total cost. The details of the method implemented in trackmate have been reported in the literature [117].

6. Once spot locations and tracks are obtained, the mean position $\langle x_N \rangle$ and mean square displacement $\langle x_N^2 \rangle$ are calculated to determine the diffusion constant D.

For two-dimensional diffusion, mean square displacement after N steps and diffusion constant are related via $\langle \Delta x_N^2 \rangle = 4Dt_N$, where $t_N = N\Delta t$ and Δt is the time step. Starting with N=1, the mean-square displacement between each unit time step is calculated for the entire track. The same calculation is carried out for higher N up to the length of the track. The same procedure is applied to all tracks. The diffusion constant is proportional to the slope of curve for the mean-square displacement depending on the time-step.

All data analysis results are saved as Matlab-files for further analysis.

Chapter 3

Imaging potassium-flux through individual electropores

Abstract

This chapter shows the development of a novel technique for potassium-flux imaging through individual electropores. The indicator dyes APG-2, APG-4 and KS2 are characterised with fluorescence spectroscopy and detailed imaging analysis is carried out for APG-4. Dynamic fluorescence response to an applied voltage protocol can be observed while monitoring several pores in parallel. The response time of APG-4 is between 2.5-10 s and the minimum resolvable current is estimated to be -2 nA. These results show the limitations of potassium-flux imaging with currently available indicator dyes.

Part of the work presented in this chapter has been published in BBA Biomembranes (Marc Szabo and Mark I Wallace. Imaging potassium- flux through individual electropores in droplet interface bilayers. *Biochimica et Biophysica Acta (BBA)-Biomembranes*, 2015). Where referenced, figures in this chapter are reproduced from this publication.

Contribution

All experimental design, experimental work and data analysis was carried out by Marc Szabo. The DIB protocol was previously developed in the lab as reported in the literature [34]. The indicator dye KS2 was obtained from a collaborator (see Materials section in chapter 2).

3.1 Introduction

As stated, optical measurements of ion flux have become an important single-channel technique with the potential for higher throughput than patch-clamping when studying the functional properties of ion channels [95, 96, 97]. More efficient screening methods are important in the context of drug discovery in order to test a broad range of potential targets [80]. Parallel recordings of oSCR from several channels or pores are also easier than parallel electrical recordings where specialised electronics and highly skilled staff are required

There is a broad variety of reports on oSCR with calcium-flux. Examples include channel imaging of nicotinic acetylcholine receptors or Aβ peptide pores expressed in Xenopus occytes [101, 102]. Planar lipid bilayer systems have also proven useful for calcium-flux imaging of cardiac ryanodine receptors [99]. The droplet interface bilayer system used in the this thesis has previously been used for imaging of calcium-flux through alpha-hemolysin and alamethicin pores. [97, 33, 118].

Despite providing a powerful tool for parallel single-channel fluorescence recordings, calcium-flux imaging is not applicable to the important class of potassium channels, because they obviously do not conduct Ca^{2+}-ions. Specific malfunctions in potassium channels have been linked to a wide range of diseases including neonatal epilepsy, deafness, and the heart condition long QT syndrome [2, 119, 120, 121]. There are more than 90 genes coding for the α subunit of potassium channels and the

largest variety can be found in the brain and heart tissue [122].Their high abundance compared to all other types of channels makes the development of high-throughput screening methods highly desirable. The major obstacle for imaging potassium-flux is the lack of potent indicator dyes that are able to detect small changes in the concentration of potassium while also showing high ion selectivity [96]. Since monovalent binding is weaker than divalent binding, affinities of potassium indicator dyes are smaller compared to calcium indicator dyes. Potassium-binding benzofuran isophthalate (PBFI) has been widely applied for bulk fluorescence assays to assess the intracellular concentration of potassium. Shortly after its development, it was used to monitor intracellular potassium homeostasis in mesangial cells [123]. In a more recent study, the intracellular concentrations of potassium and calcium were monitored simultaneously with PBFI as the potassium indicator dye [124]. When assessing the intracellular change in concentration of K^+ due to the pore forming toxin CyaA, it was concluded that fluorescence based methods with PBFI are inferior to inductively coupled plasma mass spectrometry (ICP-MS), which was shown to have higher sensitivity to changes in potassium concentration. Despite its use in many efflux experiments, the major disadvantages of PBFI are its UV excitation spectra and low signal response to changes in potassium concentration. A major reason for the poor response of PBFI is selectivity for both potassium and sodium which can cause an overestimate of the potassium concentration [125]. Recently developed indicator dyes such as KS2 [126] or the Asante Potassium Green (APG) series (Teflabs) are promising alternatives. APG-1 was chosen for a study observing the changes of potassium concentration in astrocytes during glutamate transport [127]. Apart from potassium, intracellular changes in sodium concentrations have also been monitored with the indicator dye Sodium Green [128].

Due to the relatively poor performance of potassium sensitive dyes compared to calcium sensitive ones, imaging methods with surrogate ions such as thallium or ru-

bidium are often chosen as alternatives when measuring the activity of K^+ channels with fluorescence. While there are many examples where thallium flux assays have been successfully applied [129, 130, 131], several drawbacks, not least the health and safety risks associated with thallium, and low solubility in Cl^- -buffers make alternatives favourable. Moreover, thallium and rubidium can alter channel properties compared to potassium: Thallium decreases the opening time of a Kir 2.1 channel, most likely due to changing the conformation of the selectivity filter [132]. For rubidium, drug potencies were higher in an hERG efflux screening assay compared to patch-clamp measurements with potassium [133].

Unlike for calcium flux, there are so far no oSCR of potassium or thallium flux. All optical thallium assays monitor the bulk fluorescence inside the entire cell. The shortage of effective methods for potassium imaging stands in stark contrast to the abundance and importance of potassium channels for all living organisms. It is hence important to explore the possibilities and limitations of optical assays with potassium indicator dyes that are currently available, particularly the potential for oSCR of potassium flux. The indicator dyes APG-2, APG-4 (both Teflabs) and KS2 (obtained from collaborators [126]) were chosen for further investigation. Even recently developed potassium indicator dyes have relatively low affinity compared to calcium indicator dyes that have been used for oSCR studies. For example, the calcium indicator dye Fluo-8 used for oSCR through αHL pores [97] has K_D=290nM while APG-2 and APG-4 have values of K_D=18 mM and K_D=6.5 mM, respectively. It is therefore expected that the signal and resolution for potassium-flux experiments are significantly lower compared to similar studies with calcium. Thus, rather than attempting to image potassium channels or pore-forming proteins, it was decided to image potassium-flux through high-conductance electropores. This approach provides the flexibility to quantitatively assess the sensitivity of potassium flux imaging from individual pores with high fluorescence signal due to large cur-

rents. As described in detail in chapter 1, electroporation is the permeabilization of the membrane due to an applied transmembrane electric field [134]. It is widely used as a method to introduce molecules into cells, particularly for transfection [55, 39]. However, the details of its mechanism are still relatively poorly understood. It is believed to proceed via the formation of toroidal pores in the membrane[135]. As such it can produce pores with high (≈1-13 nS [136]) conductance in comparison to a typical potassium channel (e.g. 50-100 pS for KcsA [137]). Electroporation has been studied extensively in Black Lipid Membranes (BLM) and the theoretical description predicts the formation of transient pores [134]. Although this model is generally accepted, non-pore forming models predicting membrane rupture due to compression have also been suggested [56].

Prior to imaging experiments in droplet interface bilayers, fluorescence spectroscopy is used to assess the potential of each indicator dye for oSCR based on ion selectivity and signal-to-background yield. Based on the result from bulk fluorescence, oSCR are imaged with TIRF microscopy while simultaneously recording electrical currents through the bilayer. The performance of APG-4 is analysed in detail to determine the overall response and sensitivity.

3.2 Potassium indicator dyes

To develop an assay for potassium-flux imaging in a DIB system, potential indicator dyes need to be soluble in an aqueous environment. Furthermore, excitation wavelengths should be accessible with a visible laser light. Based on these criteria, three potassium indicator dyes were chosen for further investigation to develop a technique for potassium-flux imaging. APG-2 and APG-4 are commercially available from Teflabs, whereas KS2 was obtained from our collaborator (details in the materials section of chapter 2). PBFI was not considered, because it requires UV-

excitation. The structures and properties of the selected indicator dyes are briefly described in this section.

3.2.1 APG-2

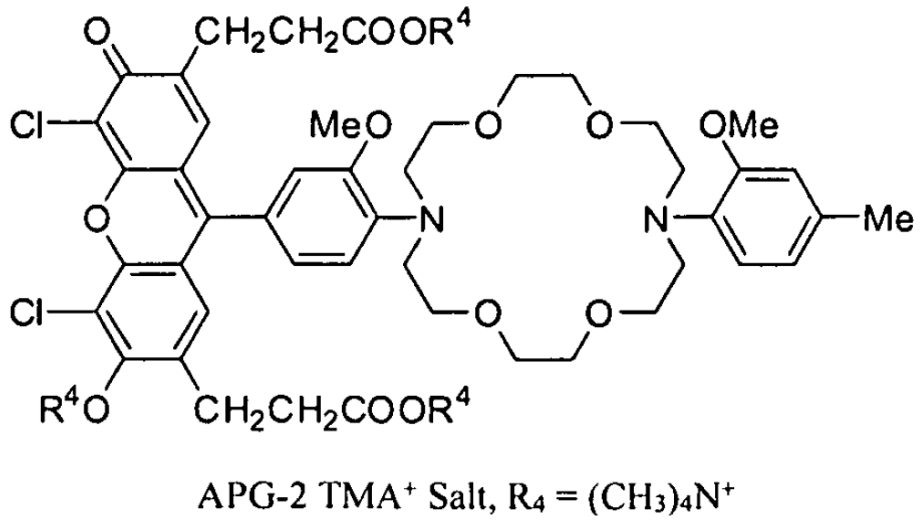


Figure 3.1: Structure of APG-2, consisting of a fluorescein dye attached to an 18-Crown-6 potassium chelator. Reproduced from[138]

According to manufacturer's data (www.teflabs.com) the dissociation constant of APG-2 is K_D = 18mM and it has a selectivity of 1.2 to 1 for K^+ over Na^+. The molecular weight is 1100 g/mol (1100 Da). The maximum excitation wavelength is 517 nm and the maximum emission wavelength is 540 nm. The structure of APG-2 is shown in Fig.3.1. It is composed of the potassium chelating crown ether 18-Crown-6 with a fluorescein dye attached to the side.

3.2.2 APG-4

APG-4 is a cryptand based indicator dye with complete selectivity for potassium and dissociation constant K_D = 6.5 mM (according to personal communication with Teflabs). The maximum excitation wavelength is 517 nm and the maximum emis-

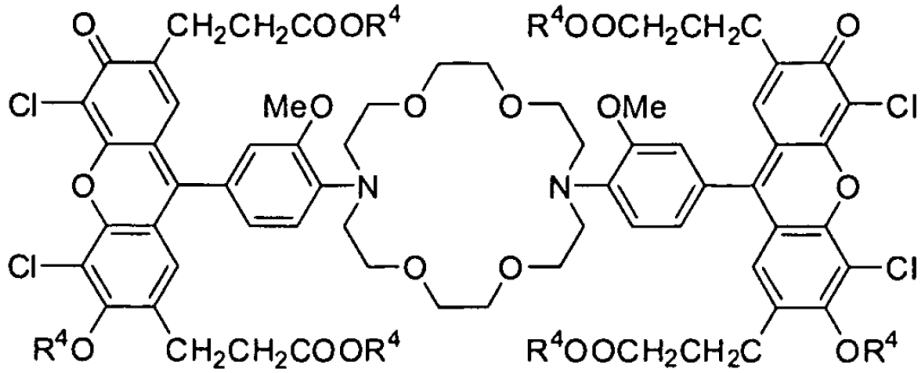


Figure 3.2: Structure of APG-3 which is similar to APG-2 but with two fluorescein molecules attached to 18-Crown-6. According to the manufacturer, APG-4 is an improved version of APG-3 with 18-Crown-6 replaced by [2.2.2]-Cryptand, a more selective chelator for potassium. However, its specific structure is not published. Reproduced from [138]

sion wavelength is 540 nm. There is no structure available for APG-4. According to the manufacturer (Teflabs) it is an improved version of the 18-Crown-6-based dye APG-3, where the crown ether is replaced with a [2.2.2]-Cryptand that is more selective for potassium. The structure for APG-3 is shown in Fig.3.2.

3.2.3 KS2

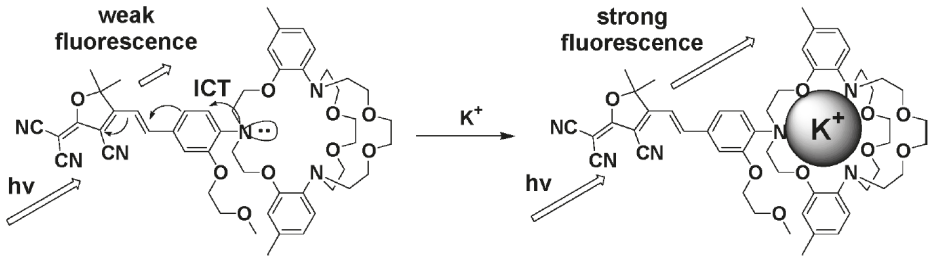


Figure 3.3: Schematic of KS2 indicator dye composed of 2-dicyanomethylene- 3-cyano-4,5,5-trimethyl-2,5-dihydrofuran (TCF) and a triazacryptand ligand. Binding to potassium ions causes an increase in fluorescence signal. Reproduced from [126]

The design and synthesis of KS2 has been reported in the literature [126]. The structure of KS2 is composed of triazacryptand (TAC) aniline derivative attached to 2-dicyanomethylene- 3-cyano-4,5,5-trimethyl-2,5-dihydrofuran (TCF). The TAC ligand is a strong electron donating group responsible for sensing potassium ions, whereas TCF is a strong electron-withdrawing group. Binding of potassium ions to TAC leads to intramolecular charge transfer, causing an increase in fluorescence signal. KS2 has high selectivity for potassium over sodium and other ions and the dissosciation constant reported is K_D = 88mM. The maximum excitation wavelength is 561 nm and the maximum emission wavelength is 650 nm.

3.3 Experimental details and data analysis

3.3.1 Fluorescence spectroscopy

The structure for the three indicator dyes used here are described in section 2.4. The detailed conditions for the fluorescence spectroscopy experiments are given below.

3.3.1.1 APG-2

APG-2 comes in powder form and is dissolved in MilliQ water to a concentration of 1 mg/ml. The selectivity of APG-2 is tested for sodium, potassium, calcium and magnesium. The fluorescence response is measured when titrating solutions with the respective ions into a buffer containing 10 mM HEPES and 5 μM APG-2 at pH 7. Based on the results of the titrations, magnesium is chosen as the counter-ion to potassium in the DIB setup. A titration of 0.5 M KCl into buffer containing 1 M $MgCl_2$ and APG-2 shows the response of the dye to potassium in a magnesium environment. The effect of Kryptofix-222 is shown in an additional titration. An excitation and emission spectrum is also recorded.

3.3.1.2 KS2

KS2 is available in powder form and dissolved in DMSO to make up a 300 μM stock solution. To test the response to potassium, a titration is performed into buffer containing 10 mM HEPES and 18 μM KS2. Since F127 (Pluronic) improves the solubility of KS2, the same titration is repeated with 0.1 % F127 present in the buffer. A titration with Pluronic into 1.5 M KCl and 18 μM is performed to test the signal increase. The excitation wavelength is at 560 nm and emission is taken at 650 nm. An excitation and emission spectrum is also shown.

3.3.1.3 APG-4

The tetramethyl ammonium (TMA) salt of APG-4 is dissolved is MilliQ water to make a 1 mg/ml stock solution. After testing selectivity for sodium, titrations of potassium into buffer containing 10 mM Hepes, 3 M NaCl, and 1.75 μM APG-4 with various concentrations of Kryptofix-222 are shown to demonstrate its effect on signal yield. The effect is also shown in an additional titration of Kryptofix-222 into 3 M KCl, 10 mM Hepes and 1.75 μM APG-4. The excitation spectrum is shown as well as emission spectra for buffers with various concentrations of KCl.

3.3.2 DIB formation

DIBs are formed according to the protocol provided in chapter 2. The schematic of the setup is shown in Fig.3.4a. The conditions for substrate and buffer composition are different for potassium-flux imaging experiments with APG-2 and APG-4. The lipid composition is the same for all experiments with 8.7 mg/ml DPhPC dissolved in 95% [v/v] hexadecane and 5% [v/v] silicone oil AR 20. The mechanism for potassium-flux imaging through electropores is depicted in Fig.3.4b. Ion-conducting pores typically start forming above ±120 mV and bilayers with pores are usually sta-

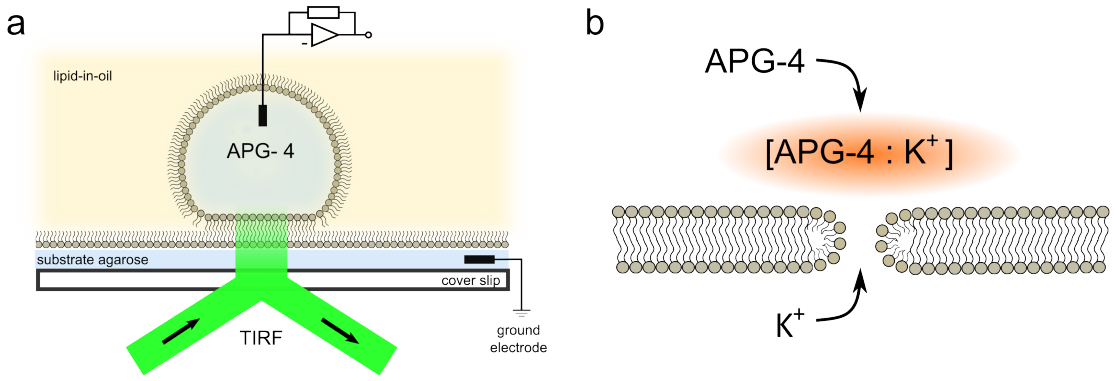


Figure 3.4: **(a)** Schematic of the DIB setup for potassium-flux imaging. The droplet contains the indicator dye APG-2 or APG-4 as well as Kryptofix-222. For APG-2 the counter-ion is magnesium, for APG-4 it is sodium. The substrate contains potassium buffer dissolved in 2% low-melting agarose.**(b)** At high voltages, electropores form in the bilayer allowing potassium ions from the substrate to translocate into the droplet region. Upon binding to APG-2 or APG-4, an increase in fluorescence is observed.

ble up to ± 250 mV. When applying a negative voltage, positively charged potassium ions are transported from the substrate across the bilayer into the droplet. Since the droplets contain either APG-2 or APG-4, there is an increase in fluorescence signal when binding to potassium ions coming through the pores. The fluorescence is imaged by TIRF microscopy using a 532 nm laser.

3.3.2.1 APG-2

Based on the results from fluorescence spectroscopy,as described in section 3.4.1, magnesium is chosen as a counter-ion for potassium in the droplet buffer. The experimental conditions for DIB formation are as follows:

- Droplet buffer: 1 M $MgCl_2$, 10 mM HEPES, 12.5 mM Kryptofix-222, 5 µM APG-2, pH 7
- Substrate buffer: 2 M KCl, 10 mM HEPES, 1.75% [w/v] low melting point agarose, pH 7 (heated to 95 ℃)

- Droplets are incubated for 20 min and transferred into a well in the PMMA device. Bilayer usually form within 1-2 mins

3.3.2.2 APG-4

With the results from fluorescence spectroscopy experiments, DIBs are formed with the following conditions:

- Droplet buffer: 3 M NaCl, 10 mM HEPES, 12.5 mM Kryptofix-222, 1.75 μM APG-4, pH 7
- Substrate buffer: 3 M KCl, 10 mM HEPES, 1.75% [w/v] low melting point agarose, pH 7 (heated to 95 ℃)
- Droplets are incubated for 20 min and transferred into a well in the PMMA device. Bilayers usually form within 1-2 min

3.3.3 Electrical recordings

Following bilayer formation, the tip of a 100 μm diameter Ag/AgCl electrode is dipped in 0.75% (w/v) low melt agarose solution, mounted on a micromanipulator, and inserted into the droplet. Coating with agarose facilitates penetration of the bilayer and insertion into the droplet. A corresponding ground electrode is inserted in the PMMA device.

The transmembrane voltage can be controlled with the patch-clamp amplifier and recorded with WINEDR (Strathclyde Electrophysiological Software, courtesy of J. Dempster, University of Strathclyde, UK). For experiments with APG-4, several voltage protocols are generated with WINEDR and electrical recordings are triggered by data acquisition with the EMCCD camera. Firstly, a squarewave potential alternating between 0 and -250 mV is applied to examine the binding response of APG-4 to potassium. Secondly, the sensitivity of APG-4 is examined by applying a

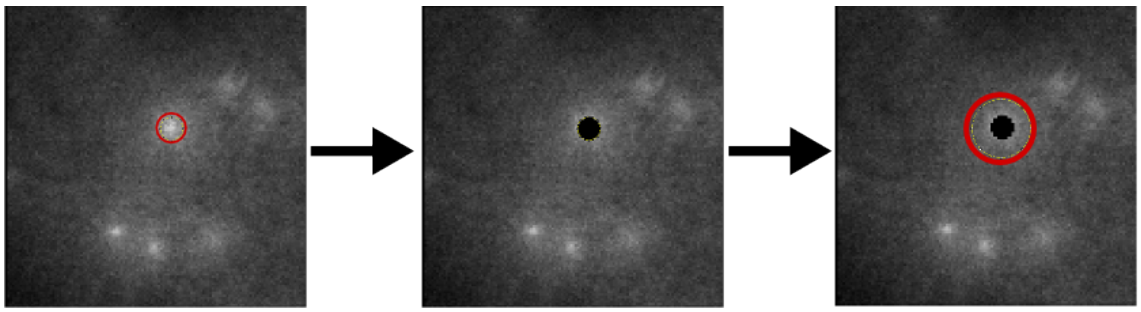


Figure 3.5: Analysis and background correction for pore imaging data. The average fluorescence is monitored for every frame in a region of interest. The region is subsequently blacked out for analysis of background signal which is obtained by selecting an annulus of 4 µm width. Images are 40 µm × 40µm

step potential starting at 0 mV and increasing up to -240 mV with step sizes of -20 mV. Voltage, current and fluorescence signal are all measured simultaneously with parallel readout.

3.3.4 Data analysis

For the analysis of APG-4 experiments, the electrical data collected with WINEDR is exported to a text file containing the voltage and current data as well as time with a resolution of 1 ms. The text file is then imported into Matlab for further analysis with fluorescence data.

The raw imaging data is saved in tiff format and initially analysed with ImageJ. The appearance and dissapearance of pores is monitored by selecting a region of interest around the centre of the pore and subsequently extracting the average fluorescence intensity in the selected region. The radius of the region is twice the full width half maximum of the fluorescence from the spots. In order to correct for background fluorescence, the previously selected region was blanked out and an annulus of 4 µm was selected for normalisation of the signal (see Fig.3.5). This is a compromise between obtaining an actual background and avoiding error due to neighbouring pores. The corrected signal is calculated by dividing the fluorescent spot signal by

the background signal.

3.4 Results

3.4.1 APG-2

3.4.1.1 Fluorescence spectroscopy

The titrations in Fig.3.6, show the fluorescence increase of APG-2 when adding potassium (3-fold), sodium (1.6-fold) and calcium (5-fold). Magnesium on the other hand, causes a decrease in signal compared to pure buffer with only APG-2. The DIB setup requires the presence of a counter-ion in the droplet to balance potassium in the substrate. Since all ions causing a fluorescence response of APG-2 are not suitable as counter-ions, magnesium was subsequently used as a balancing salt. Prior to imaging in DIBs, the bulk conditions were tested by a titration of KCl into buffer with 10 mM HEPES, 1 M $MgCl_2$, 5 µM APG-2 and 12.5 mM Kryptofix-222. As shown in Fig.3.7, the maximum signal to background increase is 40-fold. Kryptofix-222 increases the overall signal (Fig.3.7a) and also the signal to background response (Fig.3.7b). The maximum signal-to-background response for the KCl titration is 10-fold compared to 40-fold when adding 12.5 mM of the potassium chelator Kryptofix-222.

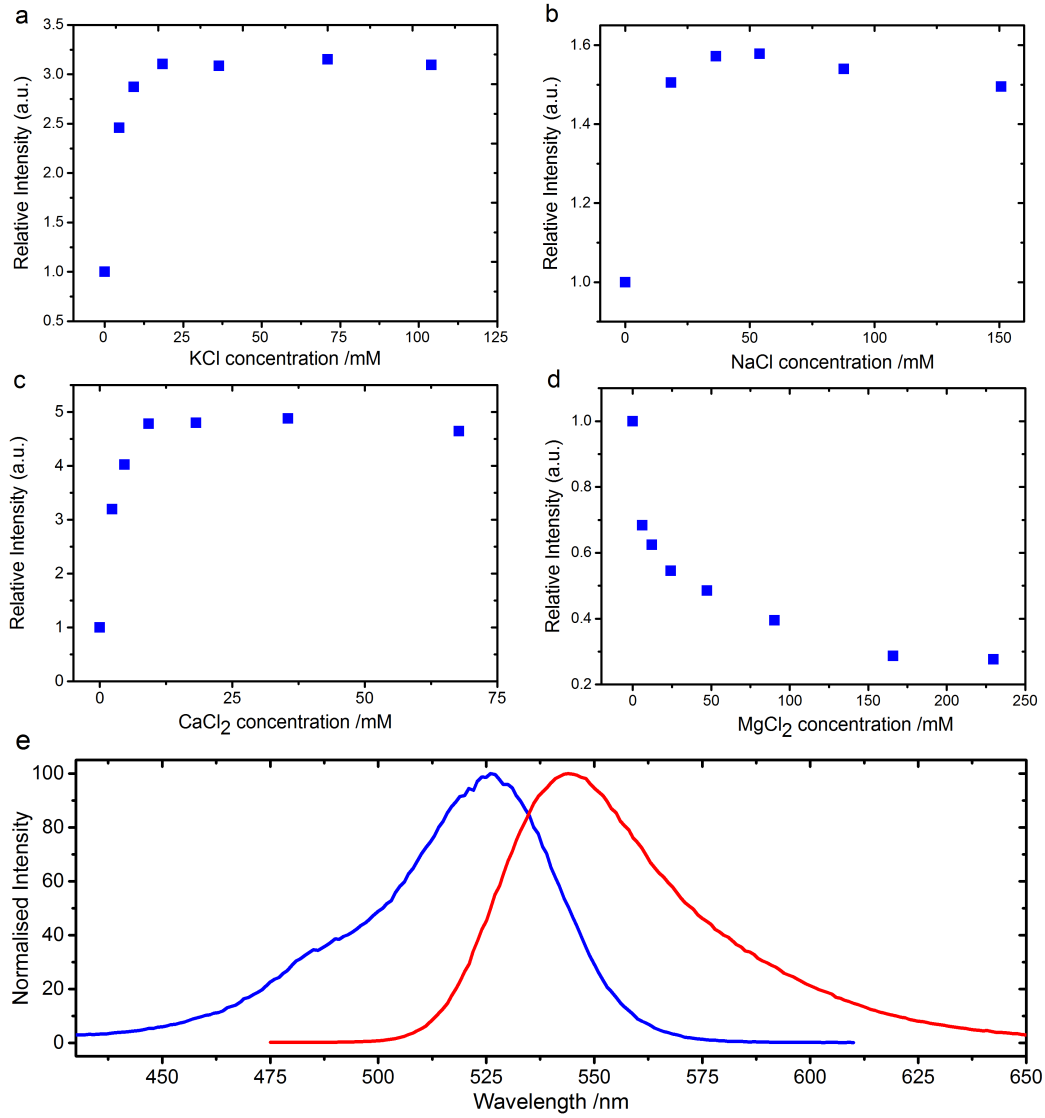


Figure 3.6: Titrations of salt solutions into buffer containing 10 mM HEPES and 5µM APG-2 at pH 7 **(a)** The titration of KCl shows a clear response of APG-2 with a maximum signal to background reached at 25 mM. **(b)** There is a small but considerable response to sodium with a 1.6-fold signal to background increase **(c)** APG-2 also shows a strong response to calcium with a 5-fold signal to background increase that is reached at around 12.5 mM. **(d)** The titration with $MgCl_2$ shows a decrease in signal due to an increase in ionic strength when adding magnesium. Since there is no increase in fluorescence, it can be concluded that APG-2 is not sensitive to magnesium. Data points represent emission signal intensity at 550 nm with excitation at 520 nm **(e)** Excitation and emission spectrum of APG-2. The data in all panels show the results for only one titration. Therefore error bars do not apply.

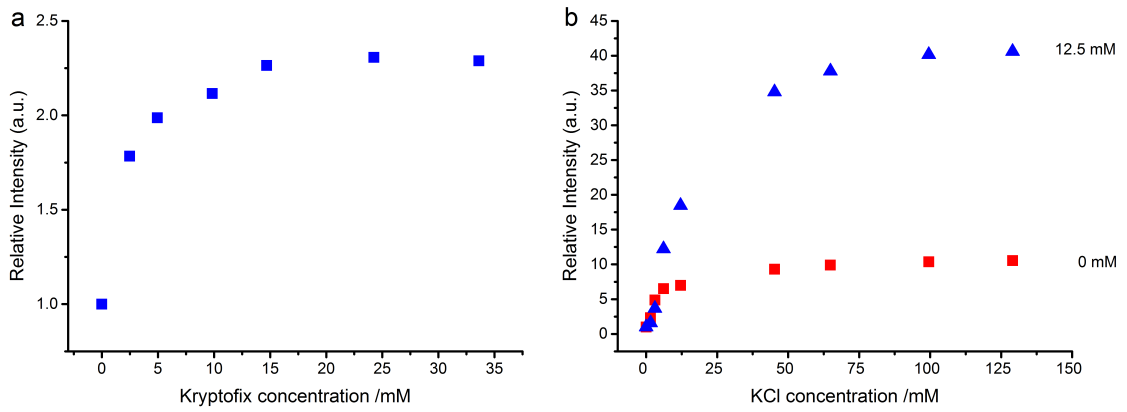


Figure 3.7: **(a)** Titration of Kryptofix-222 into buffer with 5µM APG-2, 1.5 M KCl and 10 mM HEPES at pH 7. There is a 2.25-fold signal increase upon adding Krpytofix-222 to the buffer with high potassium concentration which reaches its maximum at roughly 15 mM. Kryptofix-222 can therefore be used to improve the signal yield in potassium-flux imaging experiments **(b)** Titration of potassium into buffer with 5µM APG-2, 1 M $MgCl_2$ and 10 mM HEPES at pH 7. One titration is carried out without any added Kryptofix-222 and one with 12.5 mM Kryptofix-222. The maximum signal to background response is 40-fold with Kryptofix-222 compared to 10-fold without Kryptofix-222. The data in all panels show the results for only one titration. Therefore error bars do not apply.

3.4.1.2 Potassium-flux imaging

With the conditions obtained from fluorescence spectroscopy, potassium-flux can be imaged in DIBs as shown in the montage of Fig.3.8. A squarewave potential switching between 0 and -250 mV is applied and a corresponding alternation between high and low fluorescence around the pore-region can be observed. In panel **(b)** and **(c)**, the voltage is increased from -150 mV to -250 mV which causes the formation of several pores and an increase in fluorescence signal in the region of individual pores.

After successful implementation of potassium-flux imaging with APG-2, more potent dyes were tested to achieve a better signal-to-noise ratio. Furthermore, a major limitation of APG-2 is its sensitivity to other ions such as sodium and calcium. The requirement of $MgCl_2$ is less physiologically relevant compared to alternatives

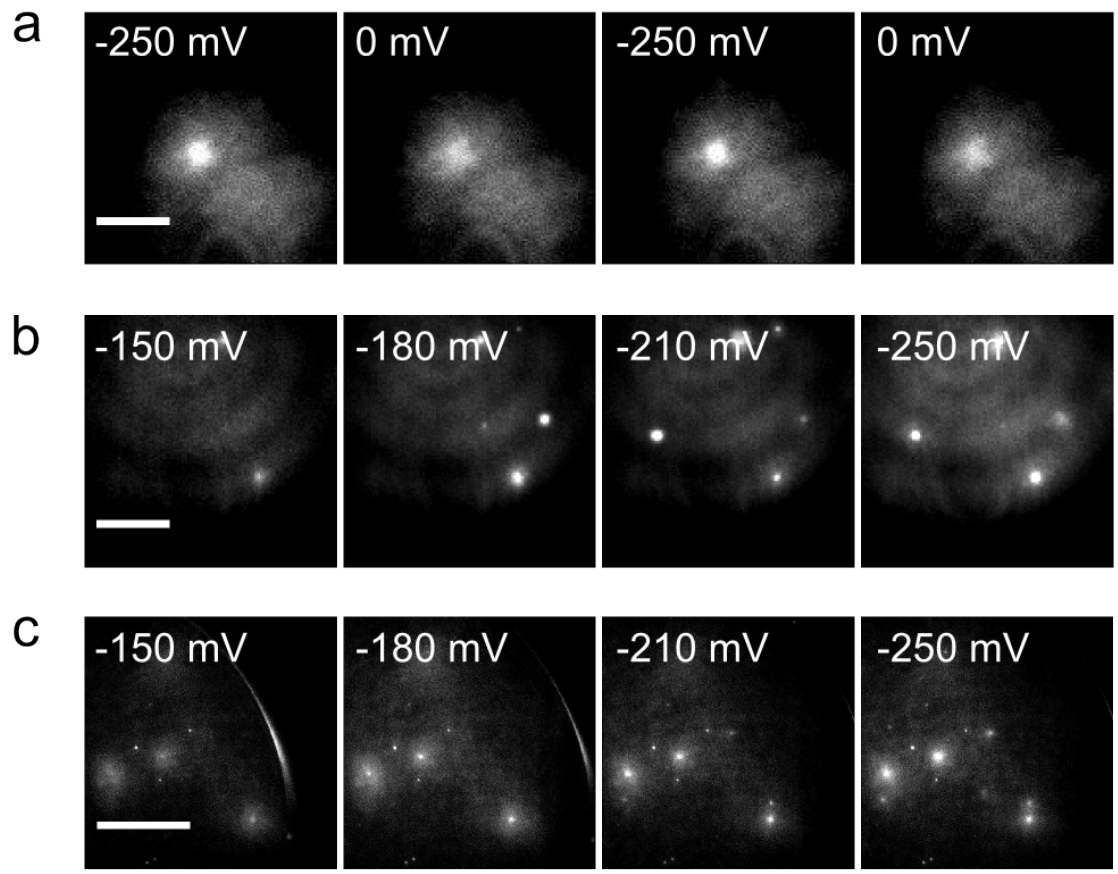


Figure 3.8: Montages of 3 recordings of potassium imaging with APG-2 **(a)** The voltage is switched between 0 mV and -250 mV. Regions of lower fluorescence correspond to 0 mV and higher fluorescences can be seen when -250 mV is applied. The remaining fluorescence at 0 mV is due to residual binding of potassium ions to APG-2 around the pore region. **(b)** Pore regions with high fluorescence due to potassium flux when increasing the voltage from -150 mV to -250 mV **(c)** The same change in voltage is applied in this recording with similar increase in fluorescence and number of pores. Scale bars are 10 μm for all images. Frame rate is 20 ms and EM gain is 300 for all datasets.

such as NaCl.

3.4.2 KS2

Comparing the response of KS2 in the presence and absence of potassium shows no difference (Fig.3.9b). The signal is very noisy and even at high voltage settings of

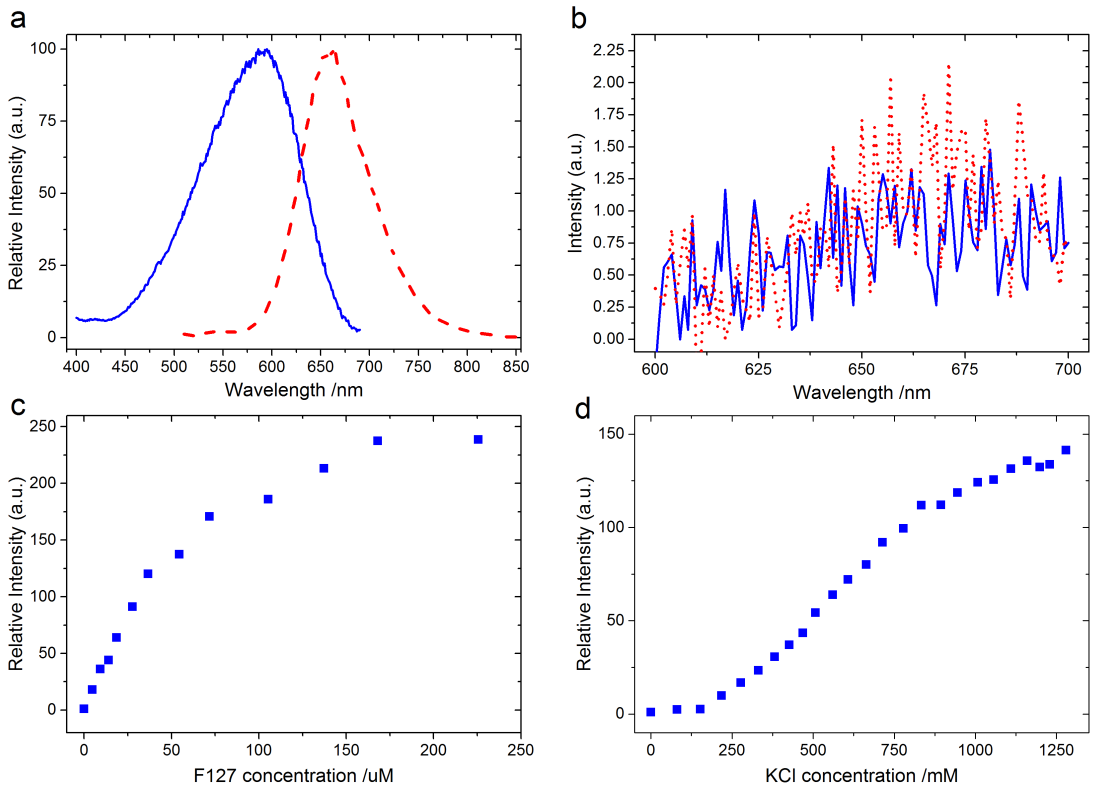


Figure 3.9: **(a)** Excitation and emission spectrum normalised to maximum intensity of each respective spectrum. The maximum wavelength for excitation is 590 nm and 660 nm for emission **(b)** Comparison of the response of KS2 in solution without potassium (dashed line) and in presence of 1.5 M KCl (solid line). There is no difference between both measurements showing that KS2 does not respond to potassium **(c)** Titration of F127 into buffer containing 1.5 M KCl and 18 µM KS2. The surfactant Pluronic improves solubility of KS2 causing a 250-fold increase in signal **(d)** Titration of KCl into buffer with 18 µM KS2 and 75 µM Pluronic. KS2 shows good response to potassium in the presence of Pluronic reaching a 150-fold signal to background at 1250 mM added KCl. The concentration of KS2 and Pluronic are kept constant during the entire titration. Data points represent signal intensity at 660 nm with excitation at 560 nm. The data in all panels show the results for only one titration. Therefore error bars do not apply.

the detector, it is very low. This is contrary to the results reported in the literature for this dye [126], where a 50-fold increase in signal was reported when adding potassium. The addition of Pluronic F127 (Poloxamer 407) is required to improve responsiveness to potassium. Pluronic is a surfactant which increases the solubility of KS2 in an aqueous environment. A titration of Pluronic into buffer with 1.5 M

KCl, 18 μM KS2 and 10 mM HEPES results in a 250-fold signal increase at 250 μM (Fig.3.9c). Based on this result, a titration of potassium into buffer with 10 mM HEPES, 18 μM KS2 and 75 μM Pluronic was performed and the maximum signal to background response is 150-fold. Since Pluronic is a surfactant, it was unfortunately not possible to form stable bilayers even at a low concentration of 4.7 μM. Since KS2 does not function as a potassium indicator without added Pluronic, potassium-flux imaging experiments with KS2 were not pursued after initial characterisation with bulk fluorimetry.

3.4.3 APG-4

3.4.3.1 Fluorescence spectroscopy

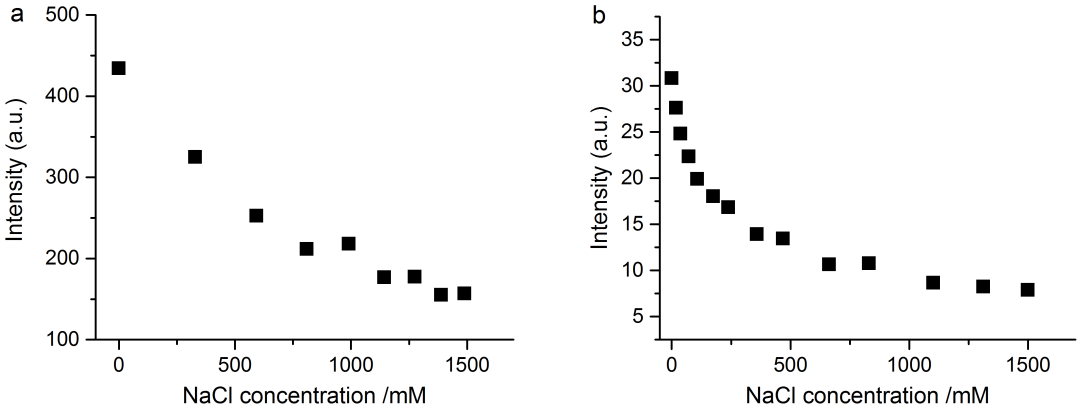


Figure 3.10: (**a**) Titration of NaCl into APG-4 in the presence of KCl (1.5 M KCl, 1.75 μM APG-4, 10 mM HEPES, pH 7). All concentrations apart from NaCl are kept constant during the titration. (**b**) Titration of NaCl into APG-4 in the absence of KCl (10 mM HEPES, 1.75 μM APG-4, pH 7). Excitation is at 520 nm and emission is at 550 nm. In both (a) and (b) the fluorescence decreases due to increasing ionic strength. The absolute fluorescence intensity is significantly higher in the presence of KCl, even as NaCl concentration is increased, demonstrating the selectivity of APG-4 for potassium over sodium. The data in all panels show the results for only one titration. Therefore error bars do not apply. Reproduced from [139]

After initial success with APG-2, the improved dye APG-4 is chosen for further

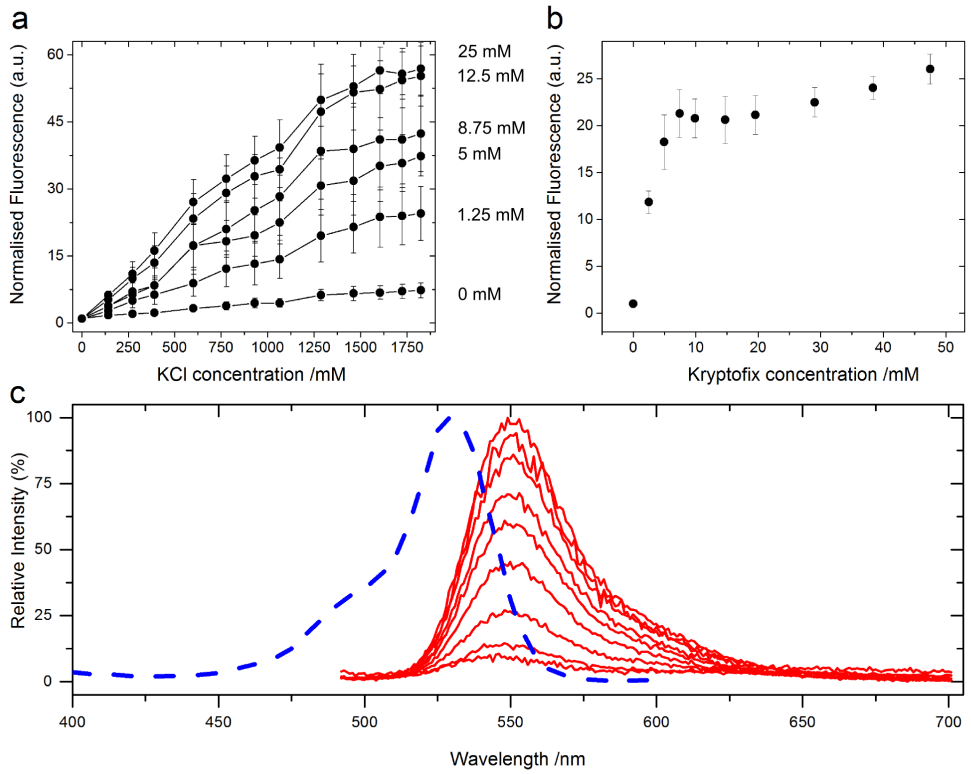


Figure 3.11: (**a**) Titration of KCl into buffer (3 M NaCl, 10 mM HEPES, 1.75 µM APG-4, pH 7) to test response of APG-4 to potassium. Fluorescence is normalised to the base level with no added potassium to show the relative increase in signal. Kryptofix-222 is also added with increasing concentrations to show the increasing effect on signal to background. (**b**) Titration of Kryptofix-222 into potassium buffer (3 M KCl, 10 mM HEPES, 1.75 µM APG-4, pH 7). The increase in fluorescence signal starts to saturate around 10 mM. Further addition of Kryptofix-222 causes no further increase. Error bars represent the standard deviation from the average of 5 data points. Reproduced from [139]

experiments due to higher affinity for potassium (K_D=6.5 mM) and because there is no selectivity for sodium. To choose an appropriate counter-ion for the DIB setup, it needs to be tested whether there is any selectivity for sodium. After confirming that sodium does not cause any fluorescence response (Fig.3.10), sodium is chosen as a counter-ion for potassium instead of magnesium. In a buffer with 3 M NaCl, the maximum signal to background response for potassium is 10-fold when adding around 1.5 M KCl. Similar to APG-2, there is a considerable increase in signal

response when adding the potassium chelator Kryptofix-222. The exact mechanism by which Kryptofix-222 causes a signal increase is currently unclear. 3.11a shows titrations of potassium into buffer containing 3 M NaCl, 10 mM HEPES and 1.75 μM APG-4 with different concentrations of Kryptofix-222. For 0 mM Kryptofix-222, the maximum response is 10-fold and for 12.5 mM it is 60-fold. In Fig.3.11b, Kryptofix-222 is titrated into buffer with 3 M KCl, 10 mM HEPES and 1.75 μM APG-4. The increase in fluorescence saturates above 10 mM and adding Kryptofix-222 no longer has any significant effect. For the appropriate choice of excitation wavelength and emission filters, the spectra for APG-4 are measured and the emission for increasing concentrations of KCl are shown in Fig.3.11c.

3.4.3.2 Potassium-flux imaging

With the conditions stated in section 3.2.2.2, bilayers are formed in a PMMA device and placed in a setup where imaging and electrical recordings can be performed in parallel. When applying a potential across the bilayer, electropores start forming above a certain threshold (typically ±120 mV in DPhPC). In order to test the response and binding of APG-4, a square-wave potential alternating between 0 and -250 mV is applied with a duration of 10 s for each voltage. The duration of 10 s is chosen in order to reach the maximum fluorescence signal after on-set of the voltage. The current and optical response are recorded in parallel as summarised in Fig.3.12. The snapshots of the pore in Fig.3.12b show regions of minimum and maximum fluorescence aligned with the corresponding regions of the potential in (a) and the current in (d). The maximum current that is resolvable in this measurement is -10 nA, as indicated by the dashed line. The fluorescence profile of an individual pore over time is obtained by selecting a circular region of interest around the pore and displaying the average signal (after correcting for background fluctuations).

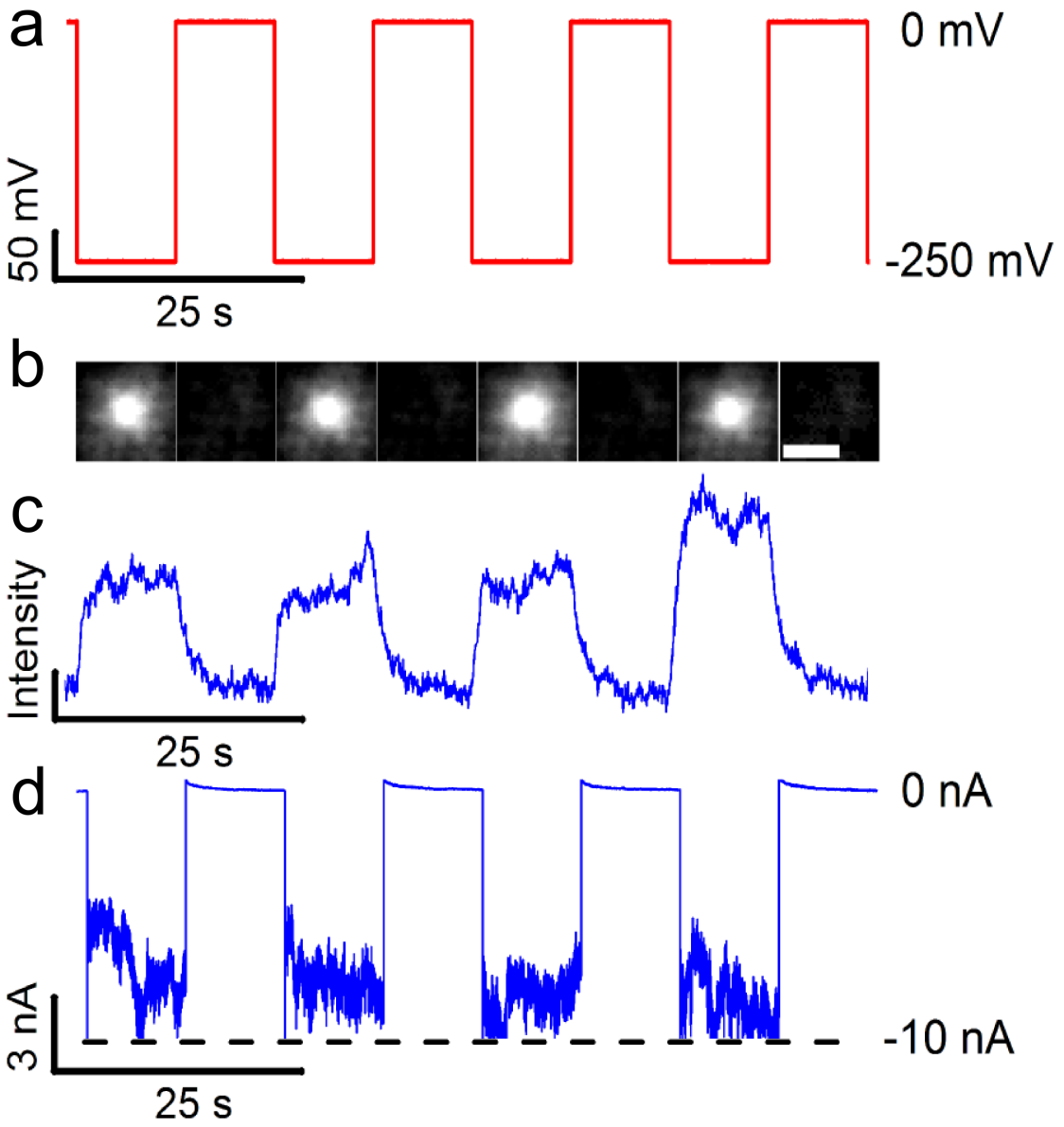


Figure 3.12: (**a**) Applied square-wave potential alternating between 0 mV and -250 mV with a full cycle time of 20 s (**b**) Optical measurement of potassium-flux through a representative pore. Each image is an average of 50 frames (20 Hz acquisition) from periods corresponding to minimum and maximum applied potential. Scale bar 5 µm (**c**) Fluorescence profile of individual pore over 4 cycles when applying the square- wave potential. Pore formation is a stochastic process and the fluctuating shape of the profiles are due to changes in conductance of individual pores. (**d**) Overall current through the bilayer. The maximum resolvable current is -10 nA, as indicated by the dashed line. Reproduced from [139]

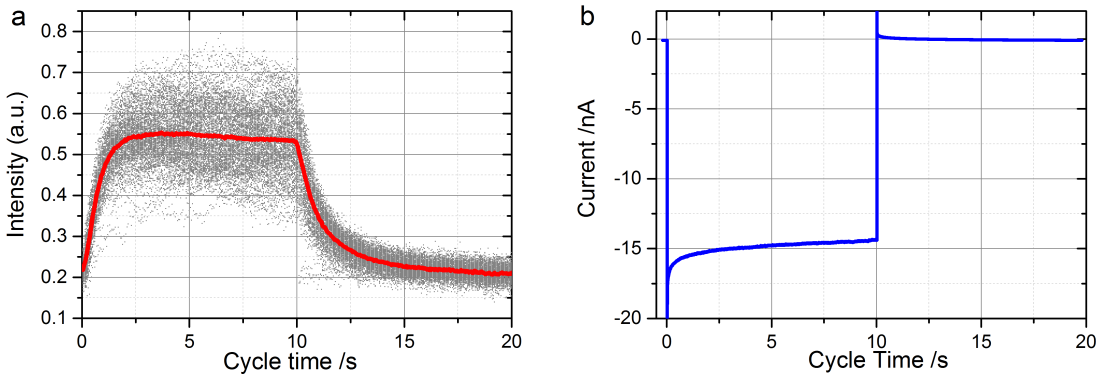


Figure 3.13: **(a)** Mean fluorescence profile averaged for 100 pores and data points from individual pores. The maximum signal is reached about 2.5 s after switching on a voltage of -250 mV. The fluorescence signal returns to its original level 10 s after turning off the voltage. **(b)** Electrical signal average for 100 measurements while applying the same voltage protocol that was used to generate the fluorescence profile. After stepwise changes of the voltage there are transition regions in the current profile due to capacitative charging of the bilayer. Reproduced from [139]

In addition to the individual pore profiles shown in Fig.3.12c, the response of APG-4 to the alternating voltage can be quantified when averaging the fluorescence profiles of several pores. The response time is a crucial indicator for resolution and hence the potential applicability of APG-4 to image potassium-flux through channels. The line in Fig.3.13a shows the mean profile of 100 individual pore fluorescence traces with cycle time 20 s (10 s at -250 mV and 10 s at 0 mV). Furthermore, all data points from individual traces are depicted to show the overall variation in fluorescence signal. To determine the on- and off- rates (time constants for reaching maximum dye response and returning to the base level after the voltage is turned off), both regions are each fitted to an exponential function. For an applied potential step of 250 mV, the time constants are t_1 =0.65 $\pm$ 0.01 s, and t_2 =1.32 $\pm$ 0.02 s. The errors are the Standard Error of the fit. The mean current response to the applied voltage is shown in Fig.3.13b for comparison with the fluorescence signal. The pore formation and disappearance seems instantaneous within the given time resolution of 1 ms. In contrast, the time it takes for the optical signal to reach its

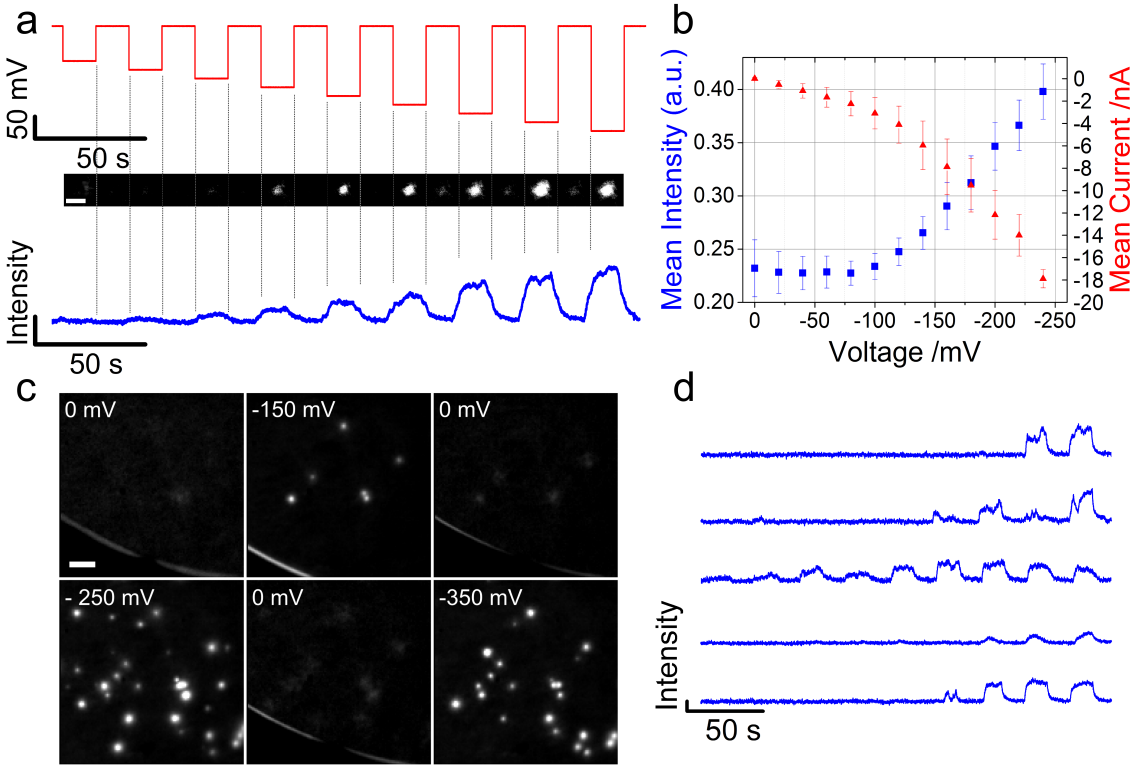


Figure 3.14: Imaging multiple electropores. **(a)** Electropores increase in brightness when applying the potential shown in the upper panel (red). Each image is the mean of 150 frames (20 Hz acquisition) from the selected region showing increasing size and brightness of the pore area as the applied potential becomes more negative. The corresponding intensity profile is depicted in the lower panel (blue). Scale bar 10 µm. **(b)** Comparison of fluorescence-voltage (squares) and current-voltage (triangles) response from electropores. Data is averaged over 13 measurements. There is no fluorescence response above -100 mV and a linear response between -100 mV and -240 mV **(c)** Image series from a different data set than the one in panel **(a)** showing the appearance of multiple pores as the applied potential is decreased. Each image is an average of 100 frames (20 Hz acquisition). Up to 30 pores are monitored simultaneously. Most bilayers are unstable below -250 mV but some remain stable down to -350 mV as shown here. Scale bar 5 µm. **(d)** The fluorescence profile of 5 individual pores while applying step potential shown in **(a)** shows pores appearing at different times. Reproduced from [139]

maximum is about 2.5 s and after turning off the voltage, it takes around 10 s to return to the base level.

To quantify the sensitivity for electropore detection using APG-4, a sequence of increasing potential steps is applied (0 to -240 mV, increment -20 mV). The fluores-

cence and current response from several pores are detected simultaneously. Fig.3.14a shows the signal of a representative pore when applying the voltage protocol shown in the upper panel. The images show that electropores clearly increase in brightness with higher potentials and go back to the base level when applying 0 mV. In order to compare the current and corresponding fluorescence response, the maximum average for both are depicted in Fig.3.14b for each voltage. Up to -100 mV there is no discernible fluorescence response while the current at -100 mV is around -4 nA. Between -100 mV and -240 mV there is a linear increase of fluorescence with voltage and the current goes down to -18 nA. Fig.3.14c shows a bilayer from a different data set where up to 30 pores are imaged in parallel. With increasing voltage, more pores form and become visible. Bilayers normally rupture below -250 mV but occasionally they remain stable up to -350 mV, like in this case. On average, the fluorescence of pores increases with voltage. However, pores appear in the bilayer at various times over the course of the measurement. This can be seen more clearly in Fig.3.14d where individual profiles are shown for 5 pores emerging at different times.

3.4.3.3 Estimate of minimum detectable current

The fluorescence response of pores when applying a step potential was shown to be proportional to the applied voltage below -100 mV, which corresponds to -4 nA. Currents through pores below this threshold cannot be resolved. Since several pores are present in the bilayer, a remaining open question is the minimum current through a single pore that can be detected by APG-4. An estimate of the minimal resolution is an important guideline for the applicability of potassium-flux imaging to pore-forming proteins. One way of characterising the minimum detectable current is a parallel optical and electrical measurement of a bilayer with only one pore present. When potassium flux through the pore becomes visible, the corresponding current

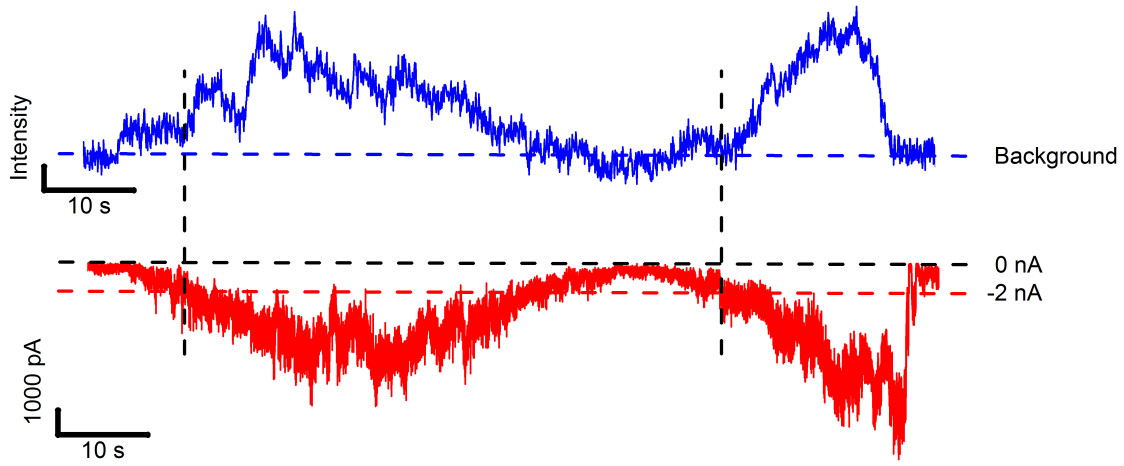


Figure 3.15: Fluorescence (blue) and electrical (red) signals from a DIB with small membrane region where only one spot is visible. By comparing current and the corresponding single-pore fluorescence level, it is concluded that no dye response is discernible above an equivalent current of approximately -2 nA (dashed line). Reproduced from [139]

gives the minimum threshold. Fig.3.15 shows the current and fluorescence trace, indicating an approximate threshold of -2 nA below which no fluorescence response can be discerned against the background.

The measurements from the step potential can be used to further substantiate the minimum detectable current estimate. As shown in Fig.3.14, no fluorescence response is visible between 0 mV and -100 mV. Therefore, the current through individual pores at this voltage needs to be calculated to obtain a minimal threshold. At -240 mV the mean overall current through the entire bilayer is -18 nA. The average number of pores visible in the bilayer at this point is 2.8 $\pm$ 1.2, which is calculated from the final frames for each of the 13 measurements (Fig.3.16). This corresponds to a -6.5 $\pm$ 2.8 nA per pore and hence a mean conductance of 27 $\pm$ 11 nS (error calculated from error propagation). The minimum conductance can be estimated when considering that a fluorescence response in only observable above

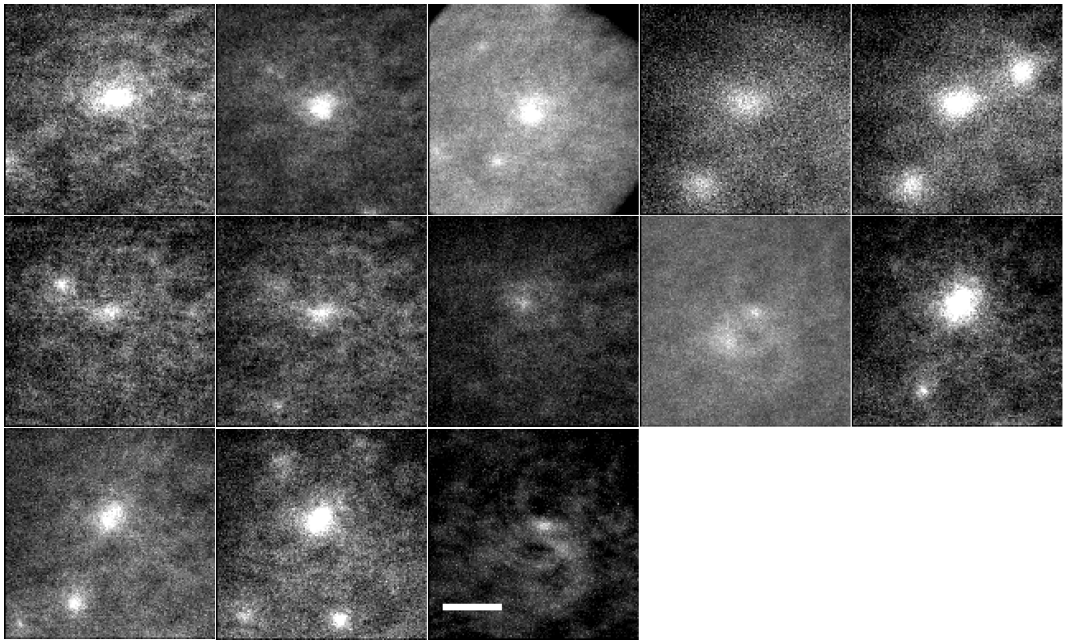


Figure 3.16: Images of all individual electropores analysed in Fig.3.14. Scale bar 10 µm, applied potential -240 mV. Reproduced from [139]

-100 mV. At -100 mV the mean conductance of 27 ± 11 nS corresponds to a limiting detectable current of -2.7 ± 1.1 nA. This is calculated from $G = I/U$ where G is the conductance, I the current and V the voltage.

3.5 Discussion

The results of this chapter show the first successful implementation of potassium-flux imaging through individual electropores. Several potassium indicator dyes are available on the market with varying selectivity and signal response to potassium ions. APG-4 is arguably the most potent candidate due to its high selectivity for potassium over sodium and other ions, as well as its comparatively high affinity (K_D=6.5 mM). While potassium-flux imaging was successfully implemented with APG-2, it is still favourable to use APG-4 due to higher affinity for potassium and the absence of response to sodium. It was shown that Kryptofix-222 improves the maximum signal to background level by roughly a factor of 6. The exact mechanism

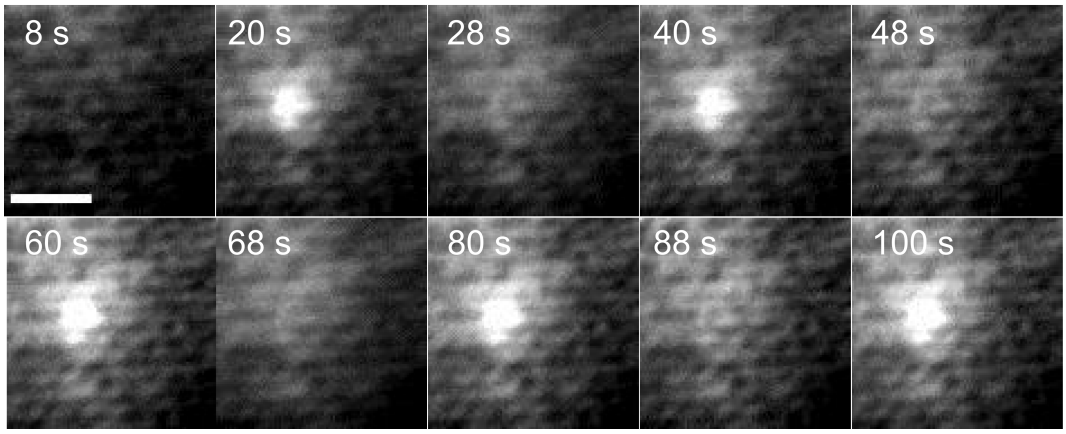


Figure 3.17: Imaging electropores in the absence of Kryptofix-222. In order to rule out the possibility that Kryptofix-222 itself was causing the fluorescence observed in the presence of an applied potential, pores were imaged in the absence of Kryptofix-222, albeit with degraded signal to noise. While it cannot be exclude that Kryptofix-222 influences the formation of electropores, it is not the cause of such pores. Each image is the sum of 80 frames recorded at 20 Hz. Scale bar is 10 μm.

of signal enhancement by Kryptofix-222 remains unclear. It was originally chosen to chelate remaining potassium ions in solution and therefore reduce background fluorescence. This is similar to using EDTA for background reduction in Ca^{2+} imaging experiments. The most likely reasons are an increase in solubility of APG-4 in the presence of Kryptofix-222 or a direct interaction between the dye and Kryptofix-222 (the maximum emission frequency shifts from 545 nm to 550 nm in the presence of Kryptofix-222). It cannot be excluded that Kryptofix-222 influences the formation of electropores, but it should be noted that potassium-flux can also be observed without the presence of Krpytofix-222 as shown in Fig.3.17.

The response of APG-4 between the onset of a voltage change and reaching its maximum signal is around 2.5 s as shown in Fig.3.13. Similarly, the decay period from the maximum signal is around 10 s. Unfortunately these timescales are still too long for potential imaging of ion channel activity where gating typically takes places on a timescale of milliseconds [140].

The step-potential measurements show a good correspondence between optical and

electrical response below -100 mV, where the increase in fluorescence is linear with voltage as shown in Fig.3.14. The maximum voltage is limited by bilayer stability, since the rupture potential of DPhPC bilayers under the conditions used here is typically around -250 mV. The minimum detectable current is calculated with two approaches, giving similar results (-2 nA and -2.7 nA). Both estimates are however somewhat crude, because it cannot be excluded that undetectable pores are present in the bilayer when considering the optical signal from only one pore. Furthermore, optical resolution of electropores is diffraction limited and therefore it is possible that punctate events are from several pores in close proximity. The number of pores giving rise to a single fluorescent spot could be investigated further by looking for discrete changes in electrical conductance or by multi-peak fitting of oSCR signals. However, theoretical studies have predicted that pores are unlikely to form in close proximity to each other. Due to a local drop in potential in the region of an existing pore, the probability of additional pore formation is reduced in that region [141].

The estimates calculated here are supported by attempts to image ion flux through αHL pores, where the signal response of APG-4 was insufficient to observe any changes in fluorescence. α-hemolysin has a conductance of approximately 900 pS [142]. At -250 mV this corresponds to a current of -225 pA through individual α-hemolysin channels. Comparing this to -2.7 nA, it is concluded there is roughly one order of magnitude difference between the minimum optically detectable current and the maximum realizable current through α-hemolysin pores.

The primary limitation in sensitivity arises from the properties of APG-4. Sensitivity depends on a combination of factors, principally the fluorescence enhancement upon ion chelation, the strength of binding, and the kinetics with which ions can be exchanged with the environment [143]. In the bulk ensemble experiments (Fig.3.11), a 55-fold signal increase upon K^+ binding can be observed, and a response time of seconds. The dissociation constant (K_D) for APG-4 is 6.5 mM. These values are

in contrast to the properties reported for the best Ca^{2+} indicators. For example, Fluo-8 exhibits a 100-fold signal increase with significantly higher affinity (K_D = 290 nM). Theoretical estimates for calcium-flux suggest that an optimal dissociation constant would be in the region of 1-5 μM [143]. Comparing this to APG-4, it is concluded that significant improvements with respect to both signal yield and ion affinity are necessary to image potassium-flux through protein pores or ion channels. More rapid reaction kinetics would also be vital if attempting to resolve ion channel gating.

Imaging experiments with KS2 were not pursued after initial testing with bulk fluorimetry. The titration of Pluronic into solution with KS2 and 1.5 M KCl showed a 250-fold increase in signal. It became evident that concentrations of Pluronic in the region of at least several micromolar are essential for KS2 to function properly. Once 75 μM Pluronic is added, KS2 shows very good response potassium and a signal-to-background yield that is around 150-fold. While this response is about 3 times higher compared to APG-2 and APG-4, the requirement of the detergent Pluronic is detrimental when forming droplet interface bilayers. It is not possible to form stable bilayer even at Pluronic concentration below 1 μM. Since KS2 does not show good response to potassium without added Pluronic, it was concluded that it was unsuitable for potassium-flux imaging in system involving lipid bilayers.

In summary, the method presented here is the first successful implementation of a technique for imaging potassium-flux through individual electropores in droplet interface bilayers. The results show that fluorescence responds dynamically to voltage changes across the bilayer and the limitations are shown with estimates of the minimum detectable current. While previous studies have successfully implemented calcium-flux imaging, there are so far no methods for potassium-flux imaging. The major limitation of this technique is the requirement of currents that are two orders

of magnitude larger than typical currents of single potassium channels. In order to implement parallel optical screening of potassium channel activity, a detection sensitivity in the region of 10-100 pA would be required. At this stage, none of the potassium indicator dyes available are potent enough to achieve this resolution. The results and estimates shown in this chapter are nevertheless an important starting point for future studies, and the technique developed is readily transferable to future indicator dyes. Incorporation of improved dyes would be very easy as long as they are compatible with a lipid bilayer system and show good solubility in aqueous solutions. Based on a theoretical study of oSCR ([143]) it is concluded that the most crucial limiting factor of APG-4 and APG-2 is the affinity to potassium ions. Although APG-4 has a higher affinity compared to previous generation dyes (K_D= 6.5 mM compared to K_D=18 mM for APG-2) it is still much weaker than calcium indicator dyes such as Fluo-8 (K_D=290 nM). In order to perform single-channel experiments similar to calcium-flux experiments ([97, 102]) it is concluded that potassium indicator dyes with K_D values in the region of micromolar are necessary [143].

Chapter 4

Electrophysiology and pore formation imaging of AMPs

Abstract

In this chapter, four antimicrobial peptides (melittin, magainin 2, alamethicin, indolicidin) are investigated in the droplet interface bilayer system. Electrophysiological characterisations show an increase in membrane permeabilisation and destabilisation in the presence of all peptides apart from indolicidin. Pore formation is visualised by calcium-flux imaging combined with single-molecule imaging of labelled peptides. Radial distribution functions show a uniform distribution of peptides on the membrane surface. Punctate poration events observed with calcium-flux most likely originate from barrel-stave (alamethicin) or toroidal pores (melittin and magainin 2). There is no evidence for pore formation by indolicidin.

Contribution

Electrical recordings, imaging experiments with melittin, alamethicin and indolicidin as well as all data analysis was done by Marc Szabo. Imaging experiments with magainin 2 were performed in collaboration with Jason Sengel. The analysis program for single-particle tracking was developed by Dr. Matthew Cheetham.

4.1 Introduction

The majority of AMPs have a positive net charge resulting in electrostatic interaction with negatively charged lipids of bacterial membranes. While the antibacterial efficacy and the structure of many AMPs are very well characterised, the pore forming mechanism is less clear [38]. The three main models for cell permeation by AMPs are the barrel-stave model, the toroidal pore model and the carpet model [68, 79]. Furthermore there are also mechanisms of intracellular killing that require translocation across the membrane without causing pore formation and subsequent cell lysis[74]. The current evidence for specific pore formation models mostly relies on structural studies from X-ray scattering, circular dichroism spectroscopy, NMR spectroscopy, atomic force microscopy, electron microscopy and also MD simulations. Pore models have also been suggested based on electrical studies in Black Lipid Membranes [144, 145]. Recently, laterally expanding pores on a scale of nano to micrometers have been visualised in SLBs with AFM and nanoscale secondary ion mass spectrometry [146].

In general, it is difficult to correlate electrical information showing membrane permeation to structural information showing the location of peptides in the membrane. Efflux experiments in vesicles with fluorescent indicator dyes provide direct evidence of leakage through a bilayer, but the position of peptides in the membrane cannot be obtained simultaneously [147, 148, 149].

Recently, a method for optical single-channel recordings of calcium-flux in supported droplet interface bilayers was developed to image currents through α-hemolysin and alamethicin pores [97, 33, 118]. The location of individual pores can be imaged while simultaneously controlling the transmembrane voltage and measuring the current through conducting pores. Here, a similar technique for calcium-flux imaging is adapted to image pore formation by AMPs. In addition to the pore location, the

spatial position of fluorescently labelled peptides is imaged with TIRF microscopy of the membrane region. When combining both methods, the distribution of peptides around the position of conductive pores can be obtained. Four peptides with different suggested modes of action have been selected for investigation: melittin (carpet model and toroidal pore model), magainin-2 (toroidal pore model), alamethicin (barrel-stave model), and indolicidin (intracellular cell killling mechanism). In the following sections, a brief review of all peptides is presented.

.

4.1.1 Melittin

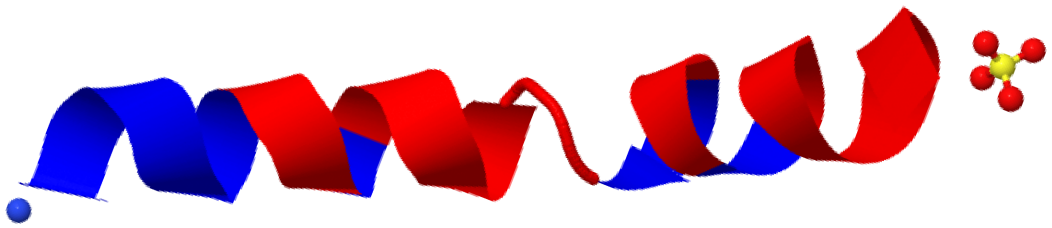


Figure 4.1: Structure of melittin which is an α-helix and composed of 26 residues. Blue represents hydrophobic regions and red hydrophilic regions. The net charge is +6 and the sequence is GIGAVLKVLTTGLPALISWIKRKRQQ. Image from the RCSB PDB [150]

The first AMP to be characterised is melittin, which is the major toxin from the bee venom. The structure as determined by X-Ray crystallography comprises of two-alpha helices connected by a bend and an overall monomer chain length of 26 (Fig.4.1). The conformation shows hydrophobic and hydrophilic regions as indicated by the colours. Melittin is well known to lyse red blood cells (hemolytic activity) but is also able to kill prokaryotic and eukrayotic cells [151]. An early model membrane study of melittin with asolectin (lipid from soybeans) found voltage-gated channel formation with conductance levels of at least 7-10 pS. In the same study, it was also

concluded that pores can have a tetrameric structure [71]. However, this was only observed under certain conditions and there is further evidence for alternative pore structures which are dependent on the lipid composition of the membrane [152]. It is generally accepted that melittin induces pore formation in membranes. Evidence stems from electrical studies as well as fluorescence efflux assays showing leakage through vesicles in the presence of melittin [147, 153]. Moreover, it was shown that melittin can cause fusion of liposomes [154] and form lipid-peptide micelle structures. Melittin has also been reported to have anticancer effects [155].

There has been considerable debate regarding the pore formation mechanism of melittin. An early study suggested a barrel-stave mechanism, similar to alamethicin, with a tetrameric pore structure [156]. However, the orientation and the pore forming mechanism of melittin in the lipid bilayer remained inconclusive [157]. While there is still some uncertainty, it is now generally accepted that melittin forms toroidal pores and can also exihibit a detergent-like carpet mechanism. Similar to magainin 2, short-lived pores with a dynamic size range that depend on peptide to lipid ratio were observed using fluorescence efflux methods [158]. Orientation sensitive experiments with neutron diffraction and oriented circular dichroism showed that the behaviour of melittin is in agreement with the toroidal pore model [159]. Further evidence comes from molecular dynamics simulations of bilayers, showing hydrophilic pore structures where lipids are translocated from the surface into the pore region [160]. Transmission electron microscopy experiments were able to visualise ring-like structures in PC/CH liposomes indicating toroidal pore formation by melittin [161].

Despite the growing evidence for toroidal pores, it is somewhat difficult to generalise the mode of action for melittin, due to the strong dependence of membrane activity on bilayer composition. An interesting study that used surface plasmon resonance compared the interaction of melittin with zwitterionic and negatively charged mem-

branes, and found separate modes of action for both compositions [162]. In the initial step, peptides bind to the membrane surface through electrostatic interactions. For zwitterioninc PC/CH membranes, this is followed by transmembrane pore formation in the hydrophobic part of the bilayer similar to a barrel-stave mechanism. For negatively charged PE/PG membranes, peptides were found to be aligned with the lipid head-groups, and act as a detergent or carpet-like mechanism, eventually leading to membrane disruption. It was also confirmed that the binding affinity of melittin is about 100-fold higher towards negatively charged membranes compared to zwitterionic ones. A different study suggested that the the presence of cholesterol affects pore formation. For DOPC and POPC membranes, it was concluded that toroidal pores are responsible for membrane permeabilisation in the absence of cholesterol. Adding cholesterol resulted in structural changes leading to open structure in bilayers [148]. Interestingly, it was also suggested that melittin has a higher binding affinity for curved lipid surfaces [163].

In summary, melittin has clearly shown to exhibit hemolytic and antibacterial activity. It causes permeation of both zwitterionic and negatively charged membranes with significantly higher affinity for the latter. The mechanism of pore formation is more elusive. While it seems generally accepted that melittin causes cell lysis by a two-state process (binding to the membrane surface followed by insertion [164]), there is various evidence that points towards the formation of toroidal pores and a carpet or detergent mechanism. It can be said for certain, that pore formation and membrane lysis is strongly dependent on membrane composition and peptide concentration.

4.1.2 Magainin 2

The peptide family consisting of magainin 1 and magainin 2 was originally discovered in 1987 [166]. Magainin 2 occurs naturally in the skin of the Xenopus laevis

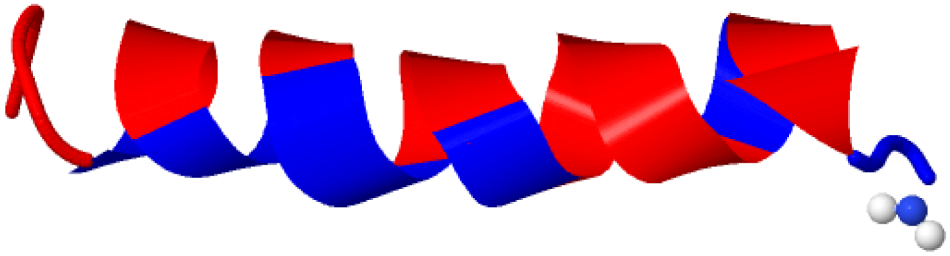


Figure 4.2: Structure of magainin 2 which is an α-helix and composed of 23 residues. Blue represent hydrophobic regions and red hydrophilic regions. The net charge is +3 and the sequence is GIGKFLHSAKKFGKAFVGEIMNS. Image from the RCSB PDB [165]

frog and has similar properties as melittin. Its structure is alpha-helical and it has positive net charge (Fig.4.2). Similar to other AMPs it shows strong antibacterial activity against a range of organisms such as *E.coli* and *S.aureus* with minimum inhibitory concentrations (MICs) in the range of micromolars [166]. Contrary to melittin, it does however not show any hemolytic activity. The lack of interaction with erythrocytes can be explained by the presence of zwitterionic lipids in the outer leaflet, abundance of cholesterol and absence of a transmembrane potential [167].
A model membrane study using PE/PS lipids found cation selective channels at a concentration of 10 µM [144], which also provided evidence that magainin 2 acts more strongly on membranes with negatively charged lipids. Strong antibacterial activity and the membrane permeation raised further questions regarding peptide-lipid interactions and the exact mechanism of pore formation. Solid-state NMR studies show that magainin 2 folds into an alpha-helical conformation and binds parallel to the membrane surface [168]. Furthermore, X-Ray diffraction experiments showed a membrane thinning effect dependent on magainin 2 concentration also indicating membrane surface binding [169]. However, conflicting evidence suggests transient

pore formation and peptide translocation across the bilayer [149]. Oriented circular dichroism spectroscopy provided a concentration dependent two-state model for magainin 2, with parallel orientation at low concentrations and perpendicular insertion at high concentrations. The apparent evidence for two state binding led to the proposal of toroidal pore formation. Increased lipid flip-flop across the membrane in the presence of magainin 2 indicated a pore model with lipids moving between both leaflets along the pore region [170]. This was independently suggested from neutron in-plane scattering experiments [171]. The strong effect of magainin 2 towards negatively charged lipids compared to zwitterioninc ones has been attributed to the formation of toroidal pores in charged membranes. The weaker binding to neutral bilayers results in a carpet-like binding parallel to the surface [172]. Recent experiments with Giant Unilamellar Vesicles (GUVs) have shown a mechanical aspect of magainin 2 action, where pore formation was related to stretching of the inner monolayer [173]. It has also been suggested that apart from membrane lysis, magainin 2 can activate apoptotic factors in *E.coli* leading to cell killing [174].

The evidence for toroidal pores seems substantial in the case of magainin 2 compared to other peptides such as melittin. While there is evidence for a two-state model with transition from parallel binding to pore formation, there has been no direct observation of toroidal pores. The observation of ion permeability at low lipid-to-peptide ratios raises questions regarding the validity of the toroidal pore model, which suggest the more generalised detergent model could be an alternative [68]. Within this model, smaller transient membrane openings are the cause of ion conductance, which include the possibility of step-wise conduction events which have also been observed in the presence of detergents [75].

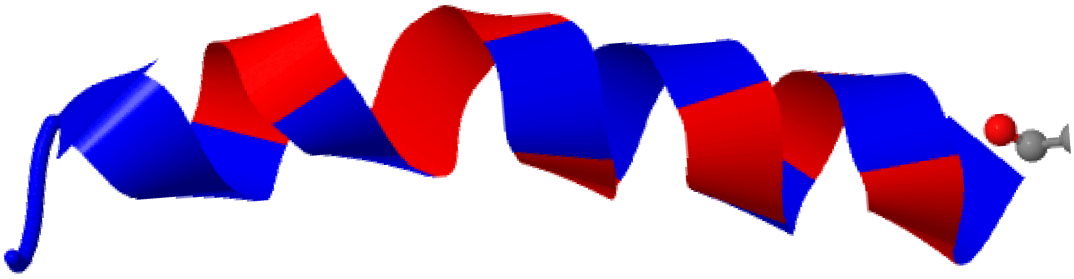


Figure 4.3: Structure of alamethicin which is an alpha-helix and composed of 18 residues. Blue represent hydrophobic regions and red hydrophilic regions. The net charge is -1 and the sequence is PAAAAQAVAGLAPVAAEQ. Image from the RCSB PDB [175]

4.1.3 Alamethicin

Alamethicin is an extensively studied peptide molecule with model membrane studies dating back to 1968 [176]. It is an alpha-helical peptide originally extracted from the fungus *Trichoderma viride*. Similar to other AMPs it shows a broad range of antibacterial and anti-fungal activity. There seems to be a small effect against gram-negative bacteria, possibly due to lipopolysaccharides (LPS) in the outer membrane [177]. Various studies confirmed the existence of single-channel traces, with discrete conductance steps, suggesting an oligomeric complex formation in lipid bilayers [145, 178]. Macroscopic alamethicin currents were shown to be voltage-dependent with much lower conductance for negative voltages compared to positive voltages. It should be noted that there are several naturally occuring alamethicin isomers, usually differing by one or two amino acids. They have been characterised by chromatography and the most frequent forms are F30 (acidic alamethicins) and F50 (neutral alamethicins) [179], with further subcategories for both groups.

The channel-like behaviour of alamethicin lead to the proposal of the barrel-stave model for pore formation [145, 180], which was supported by X-ray crystallography [181]. A pore consisting of several oligomers was suggested with hydrophilic regions facing inward and forming an aqueous core region. Several other studies using meth-

ods such as NMR or Raman spectroscopy confirmed the conformational properties of an alpha-helix with a kinked structure near the C-terminus [177]. Similar to previously discussed AMPs, alamethicin appears to show a two-state binding process with initial binding to the membrane surface followed by insertion, which occurs above a critical concentration. X-ray diffraction showed membrane thinning below a critical concentration followed by an increase in thickness above a critical concentration caused by insertion [182]. Membrane thickening due to pore formation was also observed for membrane interactions with peptidyl-glycylleucine- carboxyamide (PGLa) indicating that peptide insertion does not necessary cause membrane thinning [183]. Due to its resemblance to membrane proteins, alamethicin has become a popular model protein that has been widely studied in model membrane systems [184, 69]. Recently, calcium-flux imaging experiments in DIBs were able to resolve multiple conductance states optically while also monitoring diffusion of individual alamethicin pores [118]. While not applicable to many other known AMPs, the barrel-stave model is generally accepted as the mode of action for alamethicin.

4.1.4 Indolicidin

Indolicidin was first purified from the cytoplasmic granules of bovine neutrophils. Compared to other AMPs, it is fairly short (13 amino acids), and also has an unusual composition including 5 tryptophan and 3 proline residues. It shows strong antibacterial activity against a broad range of Gram-positive and Gram-negative bacteria, as well as fungi. [186]. The high number of tryptophan and proline in the sequence raised the question whether these are crucial for the activity of the peptide. Creating analogs showed that antibacterial function is still conserved when both residues were replaced, but hemolytic activity is lost in the absence of tryptophan [187]. There is some evidence for channel formation in planar lipid bilayers with activity around -80 mV and conductances of 0.05-0.15 nS [188]. A different study found conductance

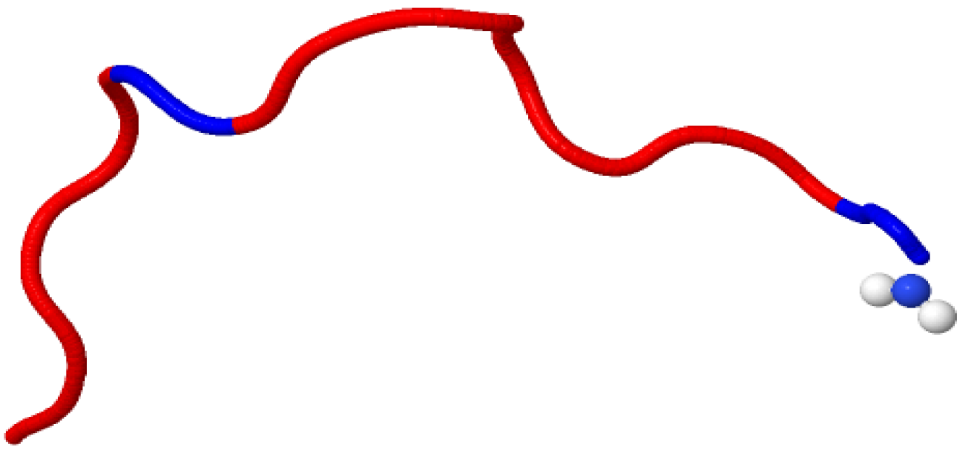


Figure 4.4: Structure of indolicidin which is extended and composed of 13 residues. Blue represent hydrophobic regions and red hydrophilic regions. The net charge is +4 and the sequence is ILPWKWPWWPWRR. Image from the RCSB PDB [185]

levels of 2.5-25 pS which were smaller compared to other peptides investigated. Interestingly, indolicidin actually had a stabilising effect on a model membrane with intact bilayers up to -330 mV [189]. However, it was suggested early on that indolicidin's mode of action does not involve cell lysis and that it's conformation is not alpha-helical but extended. Due to its short length, an extended conformation seems much more realistic than more complex structures. Despite initial observations allowing for the interpretation of a helix structure [188] or $\beta-$hairpins [190], there is conclusive evidence from NMR studies showing an extended wedge structure with a hydrophobic core and polar residues close to the termini [191]. While there is undoubtedly some interaction and binding of indolicidin to membranes, it has been shown that its antibacterial effect is due to introcellular killing mechanisms. One example is the formation of filaments in *E.coli* due to inhibition of DNA synthesis. In order to reach the intracellular domain, indolicidin needs to penetrate and permeate the inner and outer cell membrane. Insertion is enabled by its extended conformation along with its amphiphilic structure [188, 192]. Based on efflux ex-

periments with liposomes, it has also been suggested that indolicidin facilitates dye transport across membranes by acting as an organic anion carrier [193]. Molecular dynamics simulations indicate a membrane thinning effect caused by the presence of indolicidin and atomic force microscopy showed destruction of bilayer structures [194, 195].

It seems reasonable to conclude that indolicidin does not fall into the category of cell lysing AMPs. While the observation of bilayer binding and small channels clearly indicate interactions of indolicidin with membrane structures, the antibacterial effect stems from a transmembrane carrier mechanisms along with inhibition of DNA and protein synthesis, leading to filamentation of bacterial membranes [67]. Indolicidin based drugs have already been developed for therapeutic use [79].

4.1.5 Summary

The four peptides discussed here all show antibacterial activity and, apart from indolicidin, presumably act by means of pore formation leading to cell lysis. The exact mechanism of pore formation does however remain controversial. Toroidal pore formation has been suggested for magainin 2 and melittin along with a detergent or carpet mechanism depending on peptide concentration and lipid composition. The barrel-stave model is generally established as the mode of action for alamethicin and indolicidin has been shown to act on an intracellular level rather than forming pores. Part of the reason why there is still ambiguity regarding pore forming models is the inability to observe pore and peptide locations simultaneously in real-time. While conductive channels have been measured electrically in model membranes, the corresponding pore location in the membrane cannot be obtained from these experiments. Leakage through membranes is usually visualised with fluorescence efflux experiments without an electrical readout. In this chapter, an experiment allowing transmembrane voltage control and electrical readout combined with oSCRs

and single-molecule imaging of peptides is realised. Supported DIBs are used as a model membrane system allowing flexible control of lipid composition and peptide concentration. In the first part, electrophysiological measurements are performed to characterise the interactions of all four peptides with the membrane. All peptides are characterised electrically in a lipid mixture containing 69:29:2 POPE:POPG:CL. This composition mimics the inner membrane of *E.coli* bacteria. Due to the negatively charged head-groups of POPG and CL, this lipid composition is expected to have strong interactions with positively charged AMPs. From the electrical data, current-voltage-(IV) curves are produced and the rupture potential (voltage at which bilayers burst) is shown for increasing AMP concentrations. In the second part, a dual-colour setup with two lasers is used for measurements of calcium-flux oSCR through individual pores in the membrane combined with imaging of fluorescently labelled peptides. Sequential image acquisition allows the calculation of radial distribution functions showing the spatial distribution of peptides around the pore region. These experiments are the first where pore and peptide locations are imaged in the same system.

4.2 Electrophysiology

In this section, all four AMPs are characterised according to their interactions with DIBs when applying potentials and varying the AMP concentration. The setup for electrical recordings is described in chapter 2. A voltage protocol is applied starting from 0 mV and increasing in increments of $\pm$ 5 mV. This increment is chosen to obtain enough data points for the IV-curves while also ensuring feasible duration of each experiment which is typically 3 hours. The sequence of voltage in each recording is therefore as follows.

-5 mV	0 mV	+5 mV	0 mV	-10 mV	0 mV	+10 mV	...
3 min	30 s	3 min	30 s	3 min	30 s	3 min	...

Table 4.1: First steps of the voltage protocol used for electrical measurements.

The voltage is increased further in increments of ±5 mV until the bilayer ruptures. At each voltage level, the measurement period lasts 3 minutes with rest periods in between at 0 mV which last 30 seconds. The duration of 3 minutes ensures a sufficiently long waiting time for the formation of pores. The rest period of 30 seconds is chosen in order to prevent rapid changes in voltage magnitude between positive and negative values. The current is averaged for all voltages to create IV-curves showing the membrane activity of each peptide for different concentrations. In order to eliminate transition effects when switching the current on and off, 5 seconds are excluded at the beginning and end of each cycle. Each data point therefore represents the average current over 170 s. Furthermore, the absolute average rupture potential is shown depending on the concentration of each AMP. Finally, a representative electrical trace is depicted for each peptide showing the current response to an applied voltage. A representative cycle is depicted in Fig.4.5 and shows the averaging of the electrical trace when applying the voltage protocol.

DIBs are formed as described in chapter 2. The lipid composition ratio used for all experiments in this section is 69:29:2 of POPE:POPG:CL at 3.5 mg/ml in hexadecane. Stock solutions are prepared for all peptides and diluted down depending on the final concentration desired. The droplet solution prepared to form DIBs is composed of buffer (1.5 M KCl, 10 mM HEPES at pH 7) and varying concentrations of peptides. The concentration of the rehydrating substrate agarose is 2.0 % dissolved in buffer (1.5 M KCl, 10 mM HEPES at pH 7) and heated to 90℃.

As stated in the Materials section, labelled melittin, magainin 2 and indolicidin

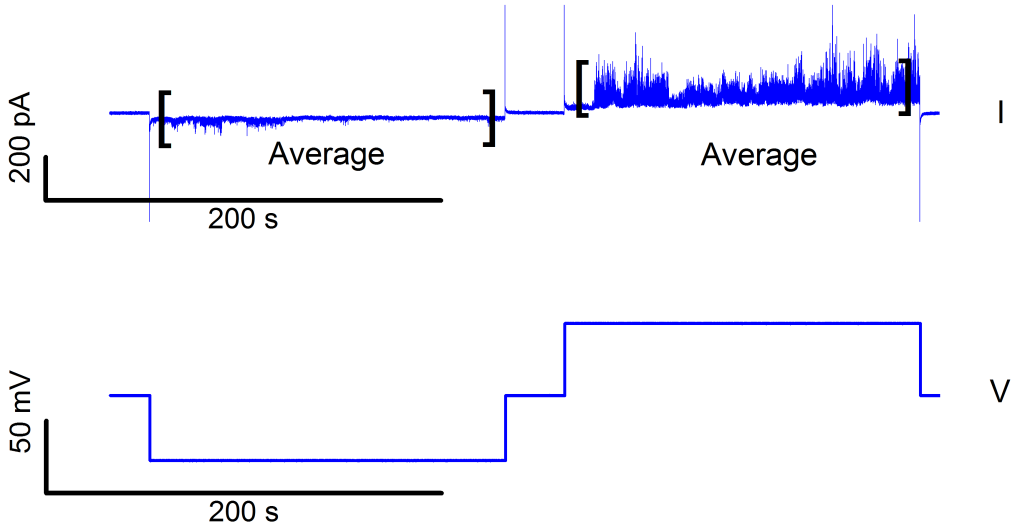


Figure 4.5: A representative cycle of the voltage protocol recording at -50 mV, 0 mV and +50 mV that is applied to DIBs to produce IV-curves for each peptide. The same cycle is applied for voltage levels starting at ±5 mV and increased in increments of ±5 mV until the bilayer ruptures. Positive and negative voltages are applied for 180 s with a rest period of 30 s at 0 mV between each step. For each recording, one data point is created for each voltage by averaging 170 s of the current data. At the beginning and the end of each trace, 5 s are excluded in order to eliminate transition effects that occur due to change of voltage.

were custom-made by Lifetein (Somerset,NJ,USA). Unlabelled melittin, magainin 2 and indolicidin were purchased from Bachem (Bubendorf, Switzerland). Unlabelled alamethicin was purchased from Sigma Aldrich and labelled alamethicin was synthesised by a collaborator from the Darren Dixon group (Department of Chemistry, University of Oxford).

4.2.1 Melittin results

TAMRA labelled melittin comes in powder form. It is dissolved in Milli-Q water and shows good solubility up to at least 5 mg/ml which corresponds to a concentration of 1.47 mM. The electrical characterisation of melittin is shown in Fig.4.6. The IV curves show a concentration of 0 nM and 400 nM. For 400 nM there is no consider-

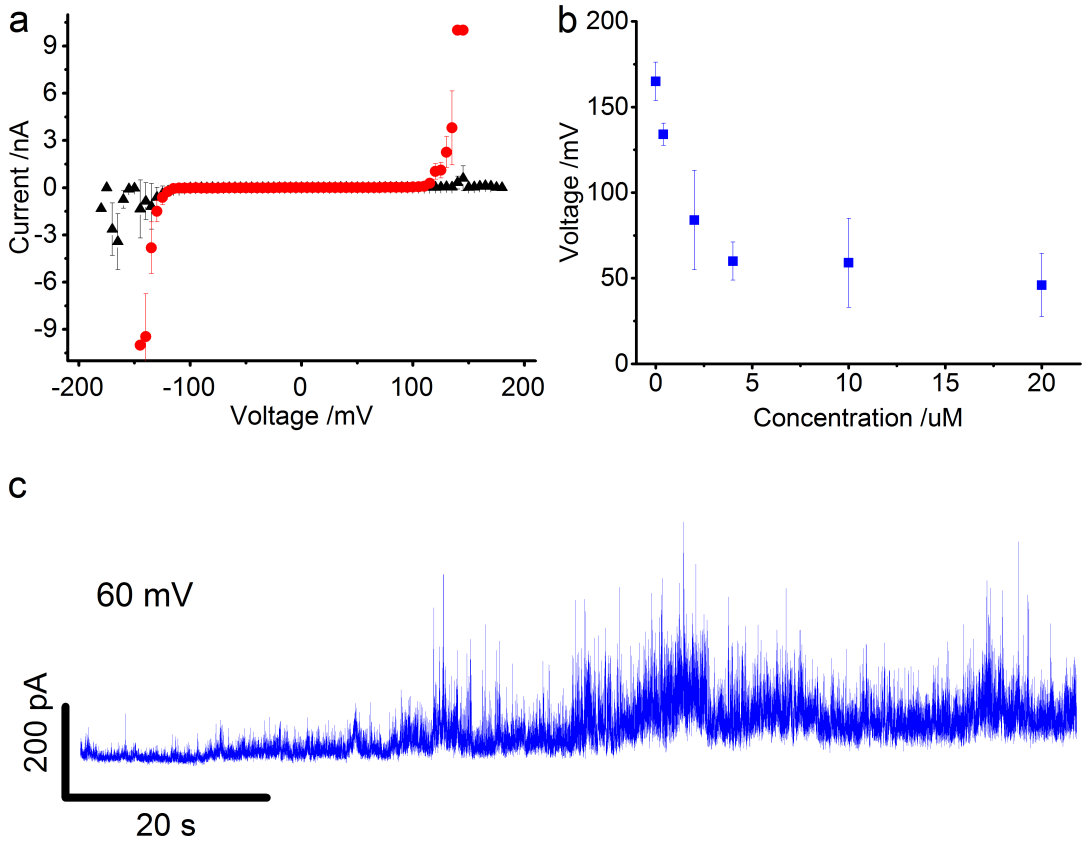


Figure 4.6: (**a**) IV-curves showing the membrane activity for 0 nM (black triangles) and 400 nM melittin (red circles) over a range of potentials in steps of ±5 mV. (**b**) Applying the same voltage protocol used to generate the IV-curves, the absolute values of rupture potentials are shown for increasing concentrations of melittin.(**c**) Representative current trace of melittin measured at 60 mV. Data points in (**a**) and (**b**) are averaged over 5 measurements. Error bars represent the standard deviation from the average for each data point.

able membrane activity below about ±120 mV followed by a noticable increase in transmembrane current. The threshold for ion conductance is clearly decreased in the presence of melittin and higher currents can be seem at lower potentials.

To further assess the stability of bilayers with increasing concentration of melittin, the absolute values of the average rupture potentials are shown in Fig.4.6b. Up to 5 µM there is a steep decrease in rupture potential from about 160 mV to 55 mV. Between 5 µM and 20 µM, the rupture potentials remains stable around

50 mV. Fig.4.6c shows a representative trace of melittin activity which is typically characterised by burst-like current patterns.

4.2.2 Magainin 2 results

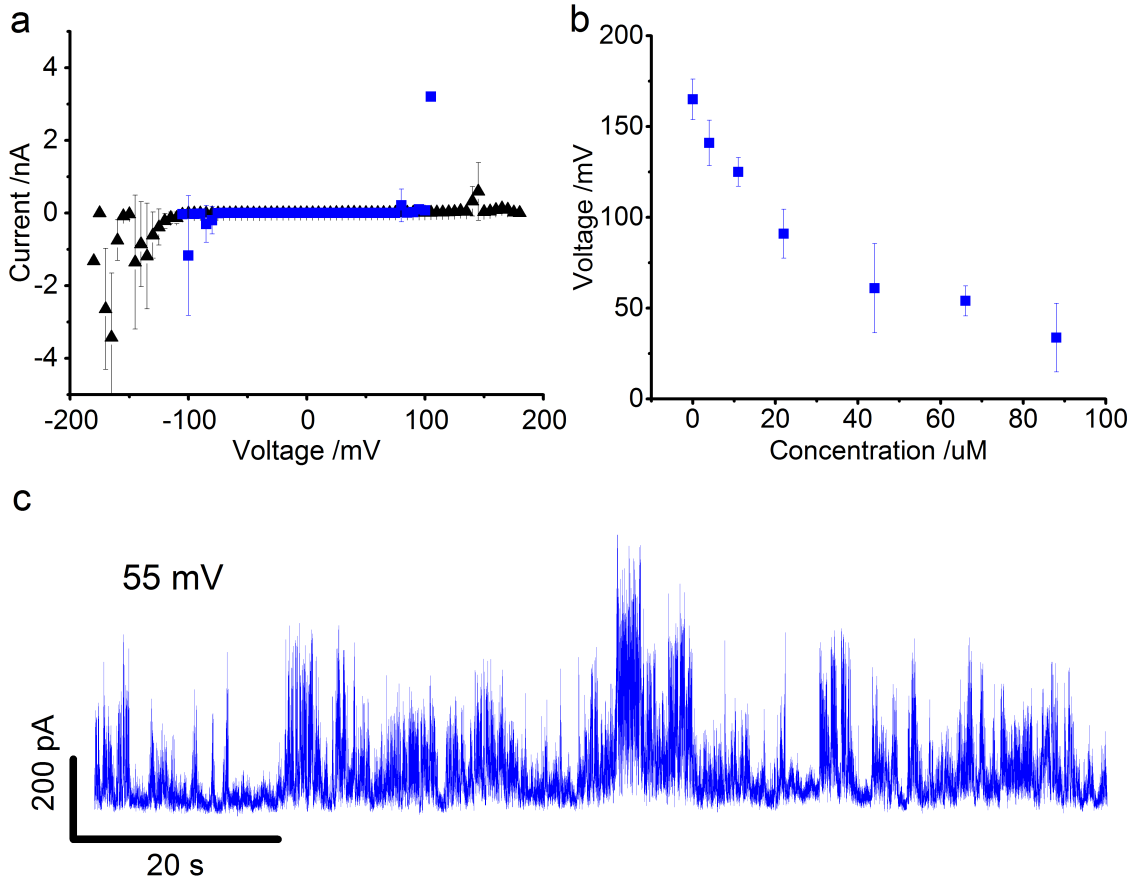


Figure 4.7: (**a**) IV-curves showing the membrane activity for 0 µM (black triangles) and 22 µM (blue squares) magainin 2 over a range of potentials in steps of ±5 mV. (**b**) Absolute values of rupture potentials are shown for increasing concentrations up to 88 µM.(**c**) Representative current trace of magainin 2 measured at 55 mV. Data points in (**a**) and (**b**) are averaged over 5 measurements. Error bars represent the standard deviation from the average for each data point.

TAMRA labelled magainin 2 is dissolved in Milli-Q water and shows good solubility up to at least 5 mg/ml which corresponds to a concentration of 1.66 mM. In Fig.4.7, the electrical characterisation of magainin 2 is shown. The IV curve

compares the current response to increasing voltages for 0 μM and 22 μM magainin 2 showing a clear increase in activity. The average burst potentials shown in Fig.4.7b decrease for increasing concentrations of magainin 2. Above about 40 μM the rupture potential decreases only slightly and ranges around 50 mV. A representative trace of electrical activity in the presence of magainin 2 is shown in Fig.4.7c. The electrical traces show frequent spikes and burst-like patterns. This is caused by opening and closing of individual magainin 2 pores and the formation of new pores in the bilayer. This is in agreement with previous studies of channel formation by magainin 2 in BLM where current fluctuations and discrete conductance levels were observed [144, 73] .

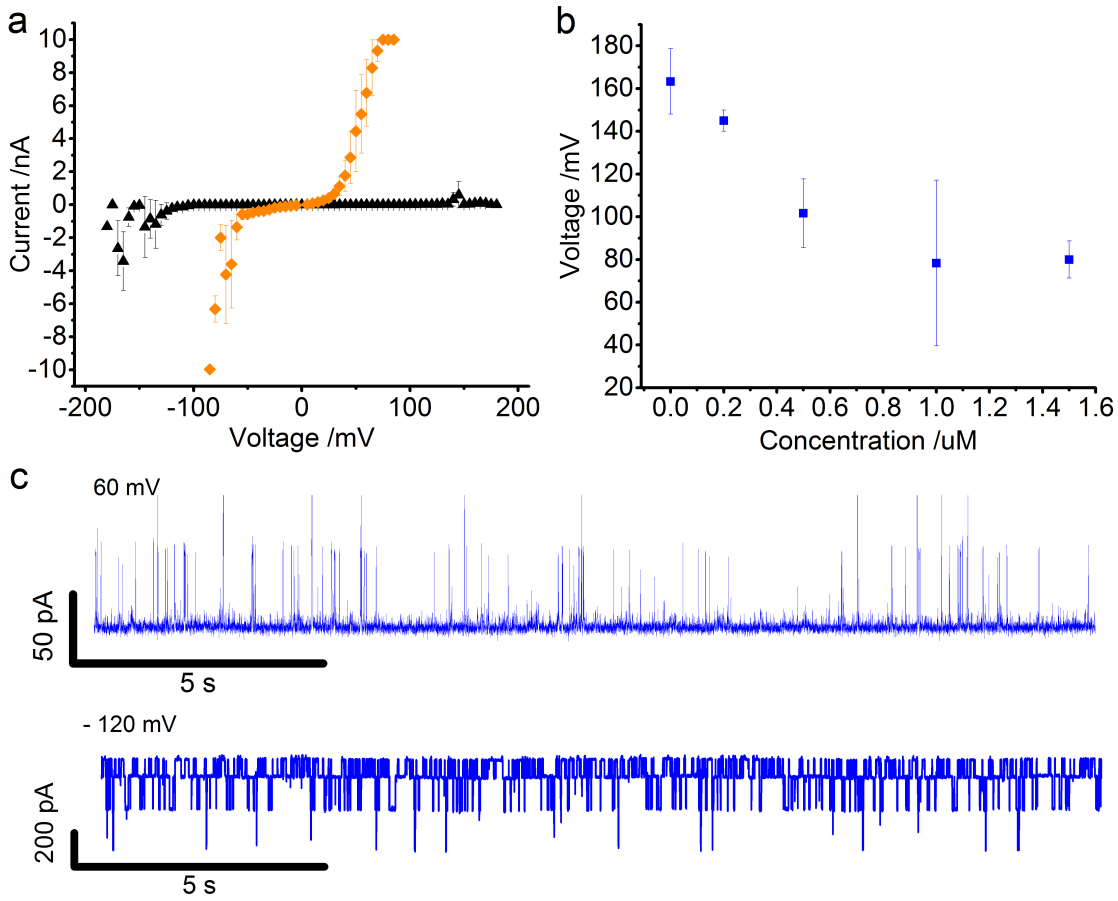


Figure 4.8: (**a**) IV-curves showing the membrane activity for 0 µM (black triangles) and 1.5 µM (orange squares) alamethicin over a range of potentials in steps of ±5 mV. (**b**) Absolute values of rupture potentials are shown for increasing concentrations of alamethicin up to 1.5 µM.(**c**) Representative current trace of alamethicin for a positive current at 60 mV and a negative current at -120 mV. Data points in (**a**) and (**b**) are averaged over 3 measurements. Error bars represent the standard deviation from the average for each data point.

4.2.3 Alamethicin results

Unlabelled alamethicin comes in powder form and is dissolved in a solution of Milli-Q water and 20% Methanol to make a stock solution of 0.833 mg/ml which corresponds to 0.42 mM. For electrical experiments, the stock solution is further diluted to appropriate concentrations only using Milli-Q. The IV-curve in Fig.4.8 shows the current response over a range of positive and negative voltages for 0 µM

and 1.5 μM alamethicin. There is a clear increase in current and distinct conductance levels for increasing voltages. Alamethicin shows asymmetric response to applied voltages with higher currents for positive compared to negative voltages. The rupture potentials shown in Fig.4.8b decrease with higher concentrations up to 1 μM and no considerable change at 1.5 μM. Droplet formation was difficult above 1.5 μM. The conductance patterns are different for positive and negative voltages and therefore two traces are shown in Fig.4.8. For positive voltages, the current response shows frequent spikes and burst-like patterns over a relatively flat base-level. For negative voltages, the current is fluctuating with occasional, channel-like gating events. Variation in conductance behaviours for different isomers of Alamethicin has been observed previously and the different isomers F50/5 and F50/7 are responsible for the asymmetry seen here [196].

4.2.4 Indolicidin results

TAMRA labelled indolicidin comes in powder form and is dissolved in Milli-Q water. Solubility is good up to 2.5 mg/ml which corresponds to a concentration of 1.02 mM. Above 2.5 mg/ml, aggregates form in the solution. The IV-curve in Fig.4.9 shows the current response without indolicidin and with 11 μM present in the buffer. Indolicidin appears to stabilise the membrane with activity shifted to higher potentials above 200 mV. Similarly, the average burst potentials are higher in the presence of indolicidin but there is no clear dependence of burst potential on concentration. The highest burst potentials were observed for 11 μM at 250 mV. A representative trace is shown in Fig.4.9c and shows the typical pattern of electroporation. Indolicidin is not reported to be a pore-forming AMP, and since there is no decrease in stability, the currents observed are concluded to be due to normal electroporation of the membrane. Similar traces of conductive pores formed only by the presence of an electric field across a membrane have been reported previously

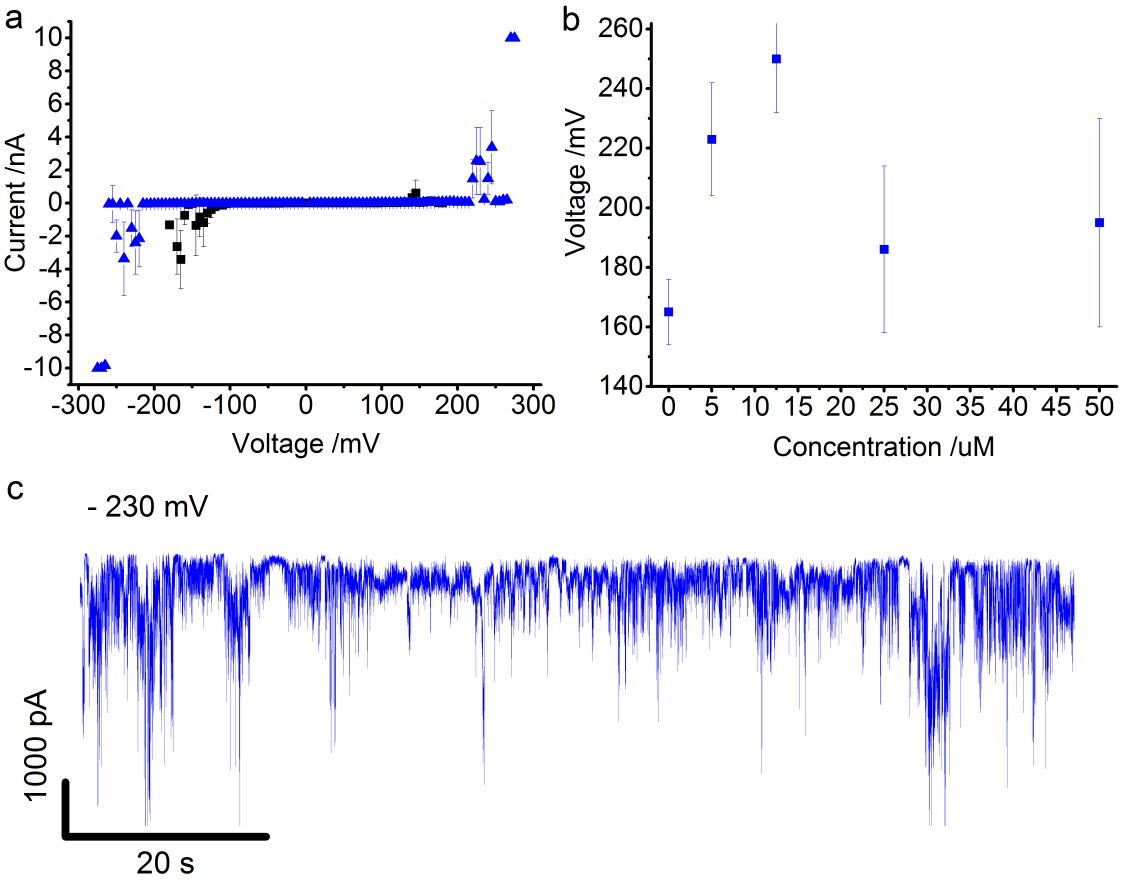


Figure 4.9: (**a**) IV-curves showing the current response for 0 µM (black squares) and 11 µM (blue triangles) indolicidin over a range of potentials in steps of ±5 mV. (**b**) Absolute values of rupture potentials are shown for increasing concentrations of indolicidin up to 50 µM.(**c**) Representative current trace of indolicidin measured at -230 mV. Given that pore formation occurs only at high voltages, the current level is also higher. Data points in (**a**) and (**b**) are averaged over 5 measurements. Error bars represent the standard deviation from the average for each data point.

[197].

4.2.5 Effect of calcium

The electrical recordings in this section are performed with 1.5 M KCl in the substrate and droplet buffer. For calcium-flux imaging, the setup must be modified such that the substrate contains 0.75 M $CaCl_2$. The droplet buffer contains 1.5 M

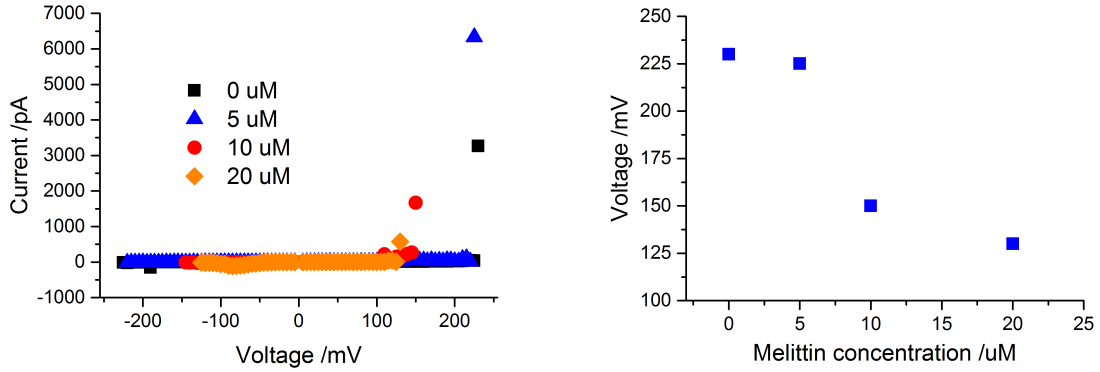


Figure 4.10: IV-curves and average burst potential for $CaCl_2$ substrate in the absence of AMPs and for 3 concentrations of melittin. Bilayers are considerably more stable compared to substrates with KCl buffer. The data in all panels show the results for only one recording. Therefore error bars do not apply.

KCl as well as the calcium indicator dye Fluo-8 and the calcium chelator EDTA. In order to test the effect of these changes on bilayer stability, three concentrations of unlabelled melittin are tested using the same voltage protocol as before to create IV-curves. Fluo-8 (19 µM) and EDTA (400 µM) are also present in the solution to reproduce the conditions for calcium-flux imaging. Four IV -curves and a the average burst potential are shown in Fig.4.10 . The concentrations are 0 µM, 5 µM, 10 µM and 20 µM melittin.

Bilayers are significantly more stable in the presence of 0.75 M $CaCl_2$ in the substrate. The burst potential for bilayers in the absence of AMPs is around 160 mV, whereas 230 mV was measured for bilayers without AMPs when using $CaCl_2$ substrates. Increased stability is also observed in the presence of melittin. While the burst potential still decreases with increasing concentration of melittin, it is 130 mV at 20 µM melittin compared to 50 mV when using 1.5 M KCl in the substrate.

This control experiments shows that with 0.75 M $CaCl_2$ in the substrate, AMPs still have a destabilising effect on bilayers and cause permeation but the events overall occur at higher voltages. For combined calcium-flux and labelled AMP experiments, this means that higher voltages will be required to cause pore formation compared

to the ones shown in the electrical studies of this section.

4.2.6 Discussion

The electrical recordings to characterise the four AMPs in this section clearly show increased membrane conductance in the presence of melittin, magainin-2 and alamethicin. For indolicidin, an overall increase in membrane stability was observed with no dependence of membrane permeability on peptide concentration. It should be noted that all peptide concentrations reported here are the bulk concentrations in aqueous solution. Only a fraction of the peptides usually partitions into the bilayer which can be quantified by the partition coefficient. There are several reports in the literature for the peptides discussed here [198, 199, 200, 190]. It would however be challenging to determine the exact concentrations of membrane-bound peptides in this system, because no reports are available for the lipid composition used here. Furthermore, the concentration of lipids in the bilayer is also uncertain. In order to compare the results from electrical studies in this section, minimum inhibitory concentrations (MIC) reported in the literature for each peptide are discussed below.

The electrical traces for melittin and magainin 2 show patterns that are similar to membrane electroporation events rather than channel activity with specific conductance levels. Alamethicin shows different current traces depending on whether positive are negative voltages are applied. The traces for indolicidin are most likely not caused by permeabilisation through peptides but through normal electroporation. The increase in stability is believed to be caused by indolicidin binding to the membrane surface and thereby making it more rigid.

There is some variability with respect to membrane activity among the other peptides. Alamethicin appears to be the most membrane active with increased conductance and reduced stability at a concentration of 200 nM and very low bilayer stability above concentrations of 1.5 μM. Melittin shows increased membrane con-

ductance beginning at concentrations around 1 μM. There is a strong decrease in membrane stability up to 5 μM and little change in rupture potential up to 20 μM. The membrane activity starts at slightly higher concentration for magainin-2, where a decrease in stability starts around 5μM and burst potentials of 50 mV are observed up to 90 μM. Antimicrobial peptide activity is commonly characterised by the minimum inhibitory concentration (MIC) which is the minimum concentration required to inhibit bacterial growth. The MIC reported for *E.coli* is 2 μM for melittin [201] and 20 μM for magainin 2 [202], which is in agreement with the trend observed here. The MIC for alamethicin reported in *E.coli* is 130 μM, which is considerably higher compared to the concentrations used here. It has been suggested that the outer-membrane acts as strong barrier to alamethicin, explaining the low antimicrobial activity towards gram-negative bacteria. Since the lipid composition used here mimics the inner membrane of *E.coli*, there is no barrier effect which explains the low concentrations observed in the electrical characterisations here. Indolicidin is known to have an intracellular killing effect due to inhibition of DNA synthesis rather than a pore forming and membrane lysing mechanism[74]. While it can trespass through the membrane into the cell, it is not known to destabilise membrane structures. BLM experiments using a mixture of anionic and zwitterionic lipids showed very stable bilayers up to -330 mV in the presence of indolicidin [189] and low activity, which is consistent which the results observed here.

The system used for calcium-flux imaging with 0.75 M $CaCl_2$ in the substrate does not change the destabilising effect of increasing AMP concentrations. However, the overall stability is greater as shown in the control experiment. Since there is no activity below 200 mV in the absence of AMPs, any currents observed below this voltage in subsequent experiments are assumed to be caused by pore formation of AMPs.

4.3 Calcium-flux oSCR and single-molecule peptide imaging

The electrical characterisation showed a membrane destabilising effect for melittin, magainin 2 and alamethicin and none for indolicidin. In this section, fluorescence imaging is used to localise pore formation in the bilayer region combined with single-molecule tracking of labelled peptides. The combination of both allows the visualisation of peptide binding to the membrane and their distribution around the respective pore regions. The toroidal pore and barrel-stave model both predict the pores that are composed of peptide structures in the membrane. Accumulation of peptides at a pore location would cause increased fluorescence from labelled peptides in the pore region. This is the first attempt to combine calcium-flux and single-molecule imaging for AMPs and the DIB system is ideal for the purpose of these experiments. Not only does it allow imaging of the bilayer region with multiple laser excitation wavelengths, but also parallel electrical recordings and voltage control across the membrane.

4.3.1 Experimental details and analysis

The setup is described in chapter 2 and conditions are identical for all peptides that are investigated. The substrate is composed of 2.0% agarose dissolved in buffer (0.75 M $CaCl_2$, 10 mM HEPES, pH 7). The droplet contains a mixture of labelled and unlabelled peptide solution, 400 μM EDTA, 19 μM of the calcium indicator dye Fluo-8 and 1.5 M KCl at pH 7. TIRF imaging is carried out by identifying pore regions in the bilayer using blue laser excitation followed by single-molecule imaging of peptides with green excitation in the same region. Both imaging sequences are recorded as one file at 20 ms exposure time and EM gain 150. The imaging data is subsequently analysed with Fiji (ImageJ) followed by tracking and further analysis in

Matlab. The spot locations from calcium-flux imaging are determined by Gaussian fitting implemented in Igor. Figures are created with Origin and Inkscape.
The following analysis steps are carried out for all AMP datasets:

1. Z-stack projection of the standard deviation for the blue channel to show the spot location and of the green channel to show the cumulated fluorescence from labelled AMP molecules. An individual frame from the green channel is also depicted to shown the distribution of labelled molecules. The tracking procedure is indicated in an additional graph showing purple circles around detected spots.

2. Calculation of radial distribution functions (RDFs) for peptide locations around the centre of a spot from a conductive pore. The peptide locations are tracked for 1000 frames and the RDF up to a radius of 30 pixels around the spot is calculated. The approximate spot diameter used for tracking is 3 pixels (810 nm). For the RDFs, a radial distance step size of 2 pixels is chosen which corresponds to a radius of 4 pixels and ensures that the step size is at least the width of a fluorescent spot. For each radial distance between 2 and 30 pixels (1 pixel= 270 nm), the RDF is calculated by counting the number of tracked spots within each distance. The number of spots is normalised to the surface are $4\pi r^2$ and to the average spot density according to the equation

$$R(r) = \frac{N(r)}{4\pi r^2 \rho(r)}$$

   where N(r) is the number of spots for the area of a given radius, r is the radius and $\rho(r)$ is the average spot density. The RDF show if there is a change in peptide density in the region of a pore compared to other regions

3. For a separate set of experiments, the total number of tracked spots are de-

termined for a range of voltages between 0 mV and -150 mV. For the same voltages, the diffusion constant is also calculated. This is to show whether there is an increase in membrane binding and peptide motility depending on the voltage.

4.3.2 Melittin results

4.3.2.1 Imaging and tracking

Imaging experiments for melittin are performed at a concentration of 10 μM with 4nM labelled peptide. 5 datasets were analysed and for each the pore locations and particle tracks were obtained. The applied voltage was in the region of -90 mV to -150 mV where stable poration events can be observed. One representative dataset is shown in Fig.4.11 with a Z-stack projection of the standard deviation for the pore locations and the labelled peptide images. Furthermore, a frame with single-molecules and the resulting tracked locations are also shown. There is a distribution of brightness among the individual fluorescent spots. It is therefore possible that brighter spots represent complexes of more than one peptide. This could be analysed in more detail by carrying out an intensity calibration or by photobleaching of individual spots. The Z-stack from the green channel shows mostly uniform fluorescence with several brighter regions. These spots indicate peptides that are temporarily stuck in the membrane. Since their location does not coincide with a spot location from the blue channel, it is concluded that they do not represent conductive pores. There is no visible increase in fluorescence signal around the pore region therefore indicating no increase in peptide concentration or complex formation. Fluorescent spots are tracked with the following parameters: Threshold=30, Spot diameter=3, Max linking distance=5, Min track length=3. To determine the sensitivity of the tracking process to the parameters, the following tables shows the number of tracks obtained from one melittin dataset. The parameter values are individually varied while keeping the other parameters constant at the values stated above.

Threshold (a.u.)	Number of tracks	Spot size (px)	Number of tracks
20	19455	2	29366
30	15785	3	15785
40	12552	4	10941

Max linking dist (px)	Number of tracks
2	20345
5	15785
8	10897

Min track length (frames)	Number of tracks
1	19817
3	15785
5	11380

The number of tracks obtained from an image stack depends on all the parameters. Increasing the intensity threshold for spot detection reduces the number of tracks, because fewer spots are considered. When increasing the spot size, the number of tracks decreases because bigger spots cover a larger area. Increasing the maximum linking distance causes a decrease in track number, because more spots are considered for each track. Therefore longer tracks are produced and the overall number of tracks is smaller. Similarly, when increasing the minimum track length, the number of tracks also decreases, because shorter tracks below the specified threshold are not considered.

4.3.2.2 Radial distribution function

The average RDF from 5 pores is shown in Fig.4.12a along with the average RDF for 5 control location in the membrane with no pore present. Both distributions show

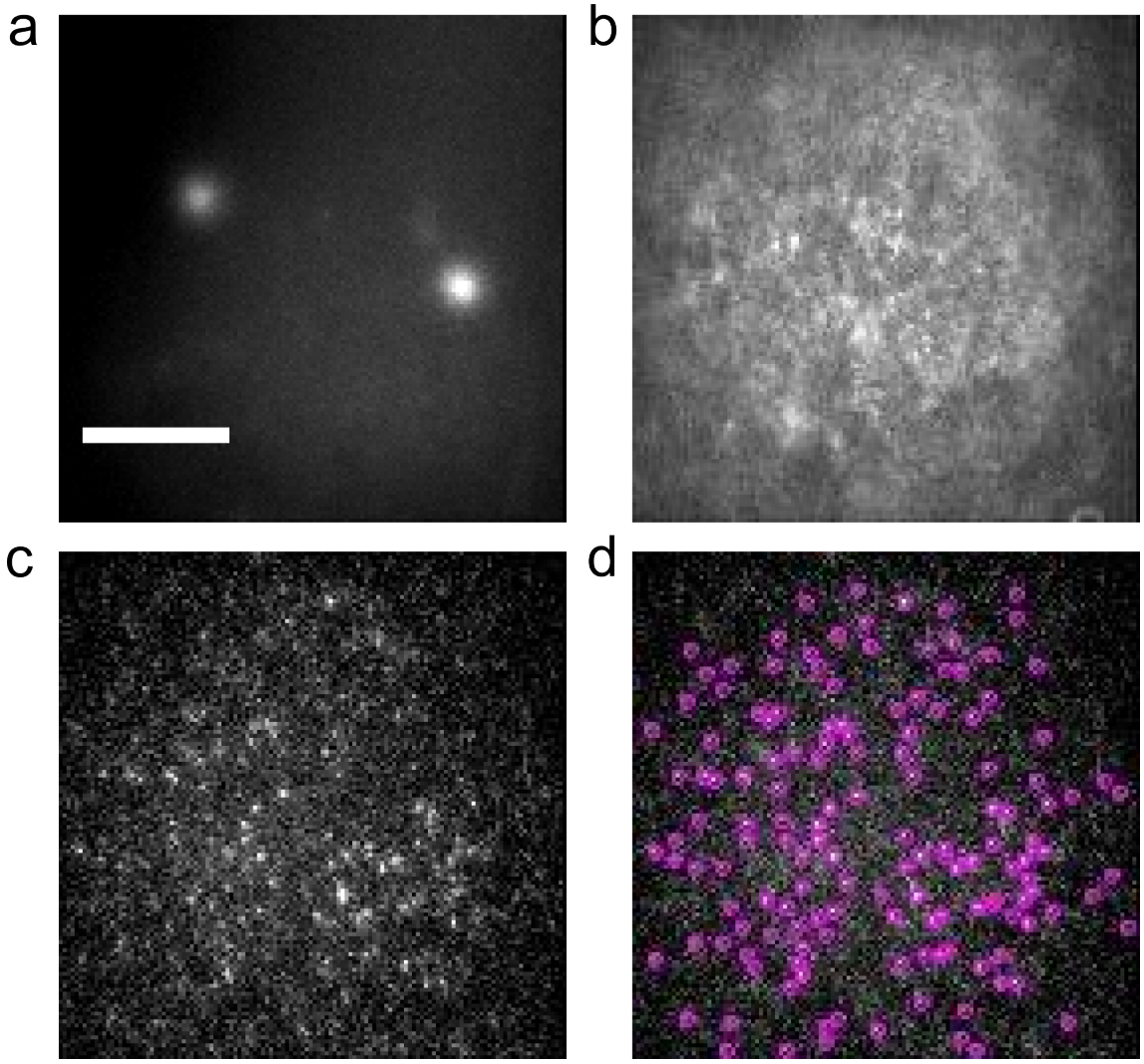


Figure 4.11: **Melittin(a)** Stack projection of the blue channel showing the location of several pores in the membrane. The applied voltage is -150 mV **(b)** Stack projection of the same area in the green channel showing the fluorescence from labelled peptide molecules **(c)** Individual frame from green channel showing the presence of labelled AMP molecules **(d)** Tracking procedure for a single frame in the green channel in order to obtain positions of peptides on the membrane surface. Purple circles are the spots selected by the tracking algorithm. Scale bar is 10 μm and the same for all images.

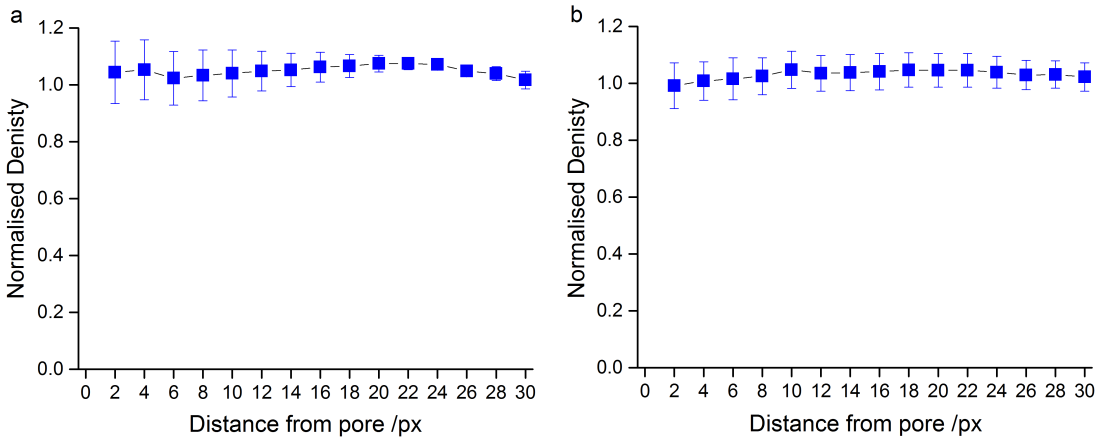


Figure 4.12: **Melittin (a)** Average RDF for peptide distances around 5 pores showing no change in peptide density around the pore region. **(b)** Average RDF for 5 control locations in the membrane without any pores present. The pore and control RDF do not show any different behaviours with respect to peptide distributions. Error bars represent the standard deviation from the average of 5 data points. 1 pixel corresponds to 270 nm.

values around one and don't change considerably with distance up to 30 pixels. This indicates that no increase in peptide concentration or accumulation around the pore region can be detected. The distribution is not different from the distribution of control points as shown in Fig.4.12b. There is uniform binding of melittin to the

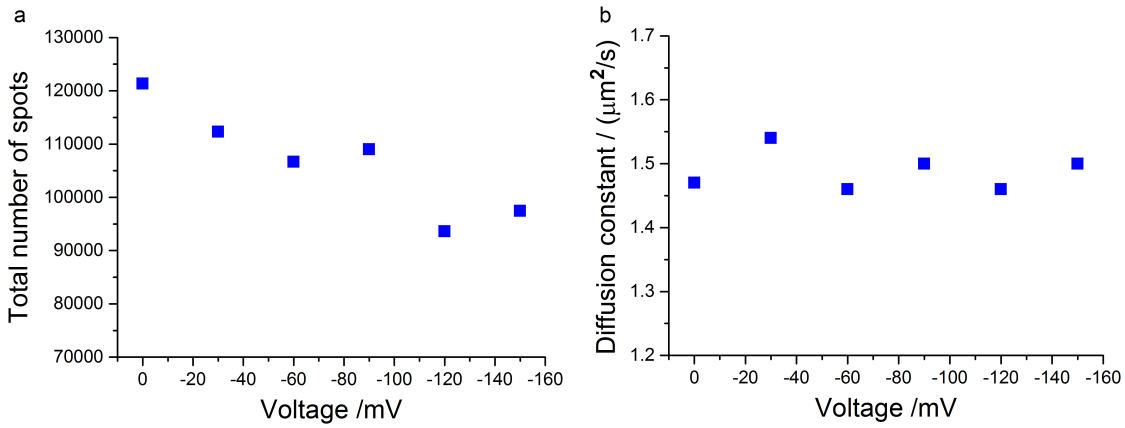


Figure 4.13: **Melittin (a)** Total spots identified in stack of 1000 frames depending on voltage.**(a)** Diffusion constant for each voltage calculated from 1000 frames. Each data point is calculated from only one dataset. Therefore errorbars do not apply.

membrane region with no preference for pore locations.

4.3.2.3 Spot count and diffusion analysis

The total spot count and diffusion constant for melittin with varying voltages are shown in Fig.4.13. Between 0 and -150 mV there is roughly a 20% decrease in spot count from melittin molecules with a small 2% increase at -90 mV. The diffusion constant is relatively constant between 1.46-1.54 $\mu m^2/s$ for all voltages with some minor fluctuations. The plots of mean square displacements against time steps in Fig.4.14 show good agreement with the fitted line up to about 0.5 s. Above this time step, there are deviations for all voltages shown. Therefore, the diffusion constants, which are proportional to the slope of the line, are only valid up to these time steps. The tracking parameter for the analysis of this dataset are: Threshold=7, Spot diameter=3, Max linking distance=5, Min track length=3.

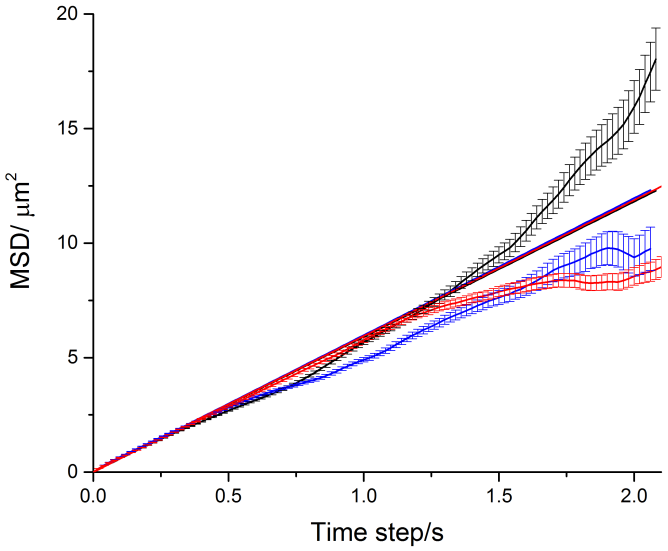


Figure 4.14: **Melittin** Mean square displacement of tracks against time steps. The data shown is for 0 mV (black), -90 mV (blue) and -150 mV (red). The lines are linear fits to each data set. Error bars are the standard deviation from the average for each time step.

4.3.3 Magainin 2 results

4.3.3.1 Imaging and tracking

For single-molecule imaging of magainin 2, the concentration is 20 μM with 4nM labelled peptide. The overall concentration was chosen based on the electrical recordings to ensure that it is high enough to cause pore formation. The concentration of labelled peptides was chosen to be in a region where individual molecules can be distinguished. Pore locations from 5 datasets were analysed along with particle tracks from labelled peptides. The applied voltage is between -130 mV and -150 mV where stable poration events can be observed.The results for one representative dataset are shown in Fig.4.15 with a Z-stack projection of the standard deviation for the pore locations from the blue channel and the labelled peptide images from the green channel. Furthermore, a frame with single-molecules and the resulting tracked locations are also shown. There is a distribution of brightness among the individual fluorescent spots. It is therefore possible that brighter spots represent complexes of more than one peptide. This could be analysed in more detail by carrying out an intensity calibration or by photobleaching of individual spots. One stable pore is visible in the membrane and there is no visible increase in fluorescence signal in the pore region compared to other regions of the membrane. While there are some bright areas in the green channel, they do not coincide with the fluorescent spot region of the blue channel. The tracking parameter for the analysis of this dataset are: Threshold=20, Spot diameter=3, Max linking distance=5, Min track length=3. The average intensity of each frame of the green channel is shown in Fig.4.16 for all 5 datasets. There is an initial decline in intensity due to photobleaching after which the intensity level remains relatively stable over 600-1000 frames. Since the signal from labelled peptides is stable over the duration of the data acquisition, tracking can be carried out for at least 1000 frames. When comparing the number

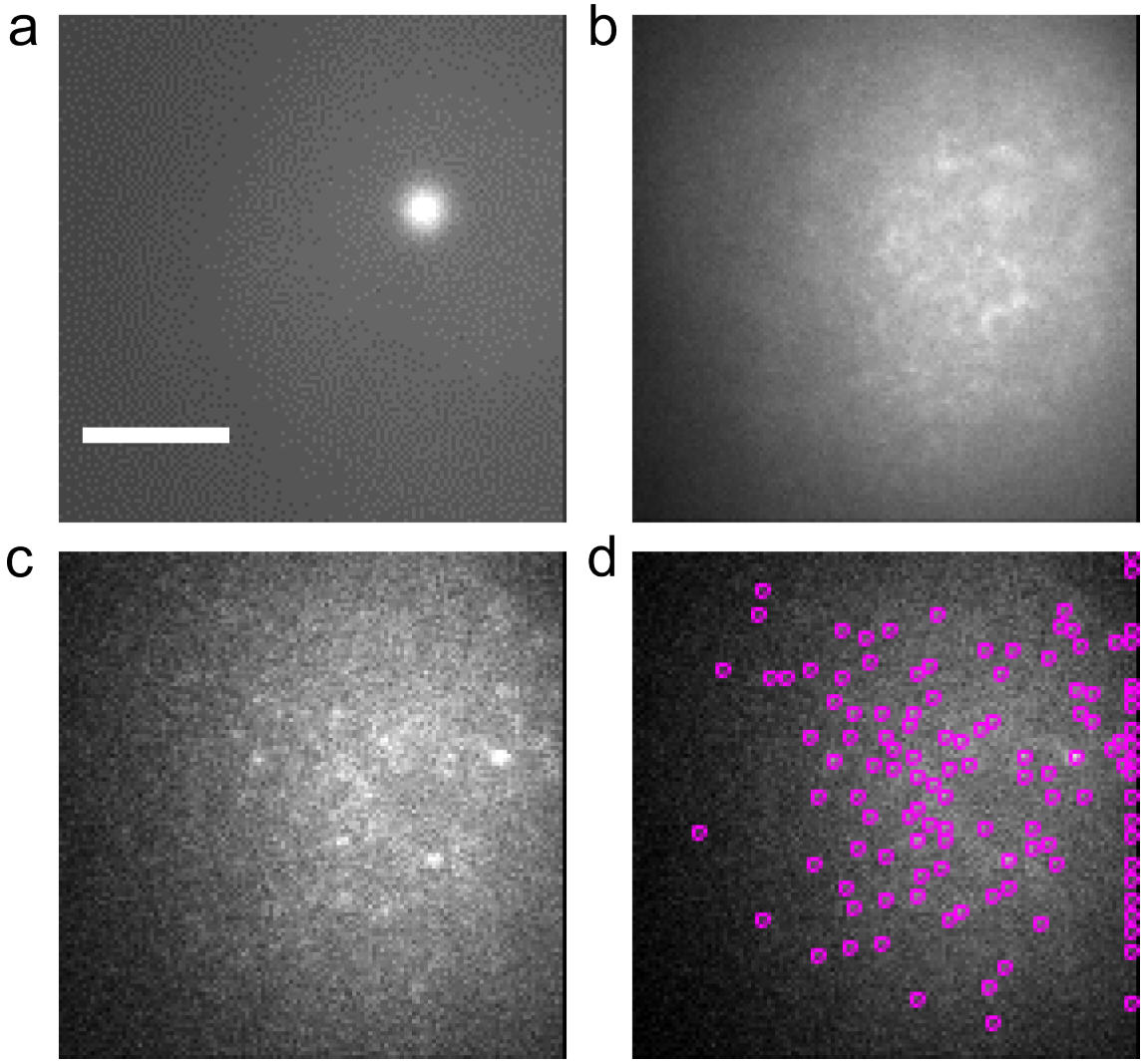


Figure 4.15: **Magainin 2** **(a)** Stack projection of the blue channel showing the location of one pore in the membrane. The applied voltage is -130 mV **(b)** Stack projection of the same area in the green channel showing the fluorescence from labelled peptide molecules **(c)** Individual frame from green channel showing the presence of labelled AMP molecules **(d)** Tracking procedure for a single frame in the green channel in order to obtain positions of peptides on the membrane surface. Purple circles are the spots selected by the tracking algorithm. Scale bar is 10 μm and the same for all images.

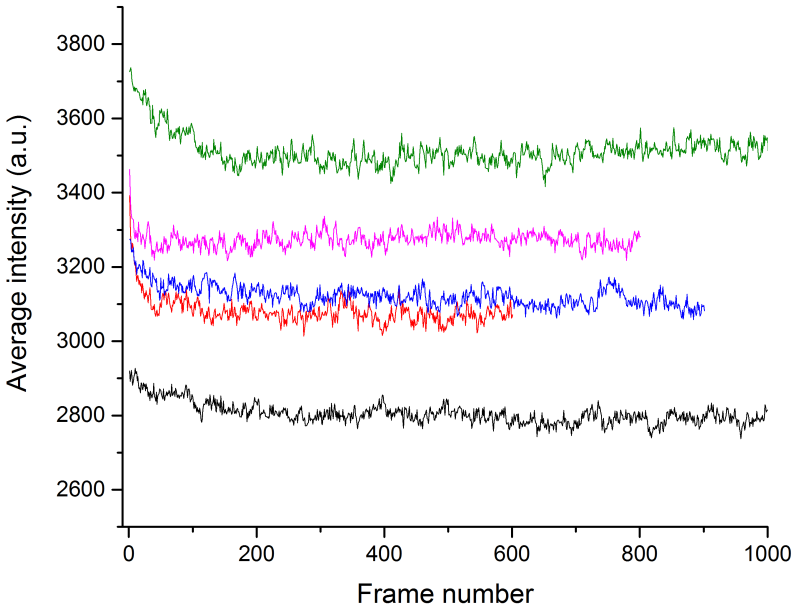


Figure 4.16: Average signal intensity for each frame of the green channel over time.

of detected spots in the first frame with the final frame, the decrease only ranges between 4-15 %. Hence, even with photobleaching there is a sufficient number of spots present over the course of the measurement.

4.3.3.2 Radial distribution function

To further analyse the peptide density around pores, the RDF of peptide locations are considered for the pore region. In Fig.4.17 two average RDFs are shown. Panel **(a)** is the average for 5 pores in the presence of magainin-2 and panel **(b)** shows a control distribution for 5 points in the membrane with no pore formation. Both functions look uniform and a range around one, indicating an even distribution of peptides on the membrane surface with no difference in the pore region. Both RDFs slightly decrease at larger distances, which is due to the illumination profile of the laser.

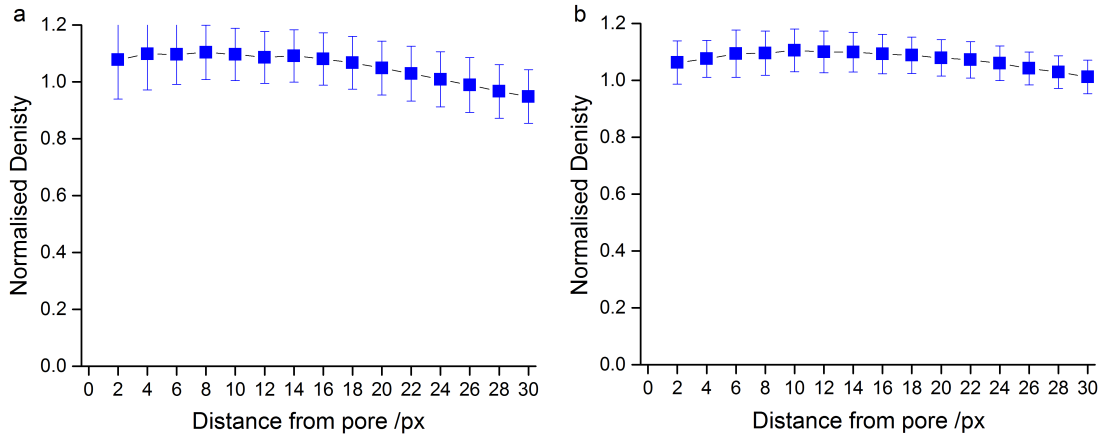


Figure 4.17: **Magainin 2 (a)** Average RDF for 5 pores formed in the presence of magainin 2. There is no change in spot density near the pore region **(b)** Control for 5 points on the bilayer with no pore present showing a uniform distribution of peptides. Error bars represent the standard deviation from the average of 5 data points. 1 pixel corresponds to 270 nm.

4.3.3.3 Spot count and diffusion analysis

The total spot count and diffusion constants for magainin 2 with varying voltages are shown in Fig.4.18. There is a clear decrease in spot count between 0 and -150 mV

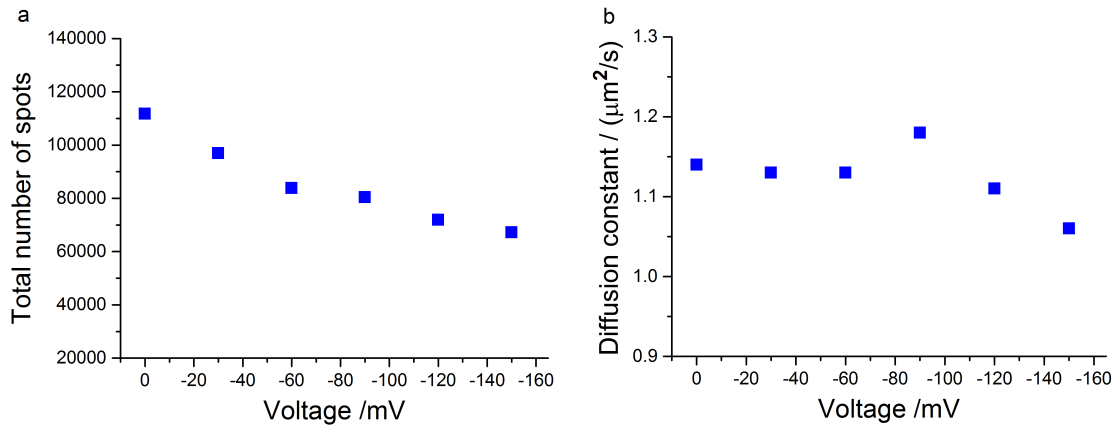


Figure 4.18: **Magainin 2 (a)** Total spots identified in stack of 1000 frames depending on voltage. **(b)** Diffusion constant for each voltage calculated from 1000 frames. Each data point is calculated from only one dataset. Therefore errorbars do not apply.

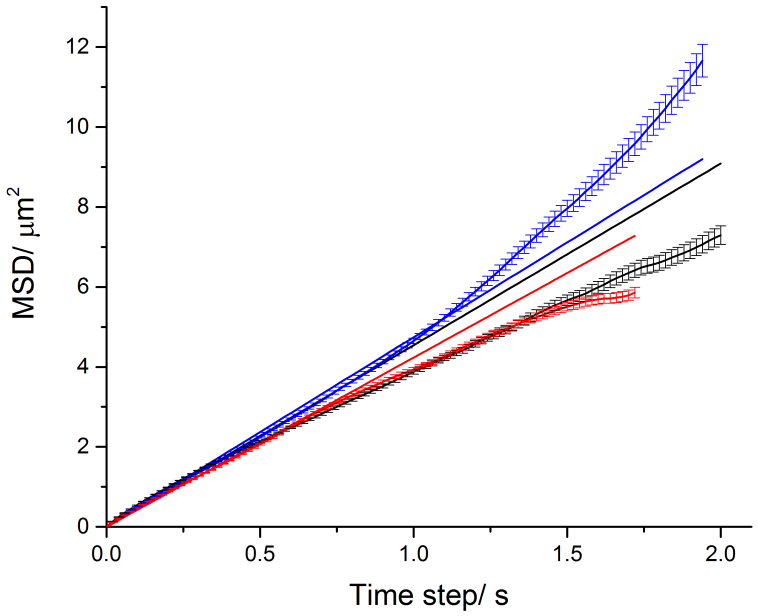


Figure 4.19: **Magainin 2** Mean square displacement of tracks against time steps. The data shown is for 0 mV (black), -90 mV (blue) and -150 mV (red). The lines are linear fits to each data set. Error bars are the standard deviation from the average for each time step.

from a total of about 1100000 to 70000 spots. The diffusion constant is relatively constant around 11.5 $\mu m^2/s$ with a marked increase at -90 mV. Overall the motility of magainin 2 molecules does not seem to be affected by an increase in voltage. The plots of mean square displacements against time steps in Fig.4.19 show good agreement with the fitted line up to about 0.5 s. For -90 mV there is better agreement up to about 1 s. Therefore, the diffusion constants, which are proportional to the slope of the line, are only valid up to these time steps. The tracking parameter for the analysis of this dataset are: Threshold=8, Spot diameter=3, Max linking distance=5, Min track length=3.

4.3.4 Alamethicin results

4.3.4.1 Imaging and tracking

Imaging of labelled alamethicin was performed at a concentration of 1 μM unlabelled and 4 nM labelled peptide. The unlabelled peptide consists of two isomers F50/5 and F50/7, whereas only the F50/7 isomer is labelled. The applied voltage was between -130 mV and -150 mV. The pores imaged with calcium-flux were very stable and long-lived and could therefore be easily localised. The Z-stack from the green channel shows uniform fluorescence with several bright spots visible. These spots indicate peptides that are temporarily stuck in the membrane. There is a distribution of intensities among the individual fluorescent spots. It is therefore possible that brighter spots represent complexes of more than one peptide. This could be analysed in more detail by carrying out an intensity calibration or by photobleaching of individual spots. Since their location does not coincide with the location of the fluorescent spot from calcium-flux imaging, it is concluded that they do not represent conductive pores. The pore region itself does not show any visible increase in fluorescence signal therefore indicating no increase in peptide concentration or complex formation. Fluorescent spots are tracked with the following parameters: Threshold=25, Spot diameter=3, Max linking distance=5, Min track length=3.

4.3.4.2 Radial distribution function

In Fig.4.20b, there are no bright spots or an increase in fluorescence visible around the pore region. To quantify the distribution of peptide molecules around the pore region, the RDF is show in Fig.4.21. The average RDF for 5 pore locations in panel **(a)** does not show any difference to the control distribution for non-pore locations. Both indicate a uniform distribution of peptides within a radius of 30 pixels.

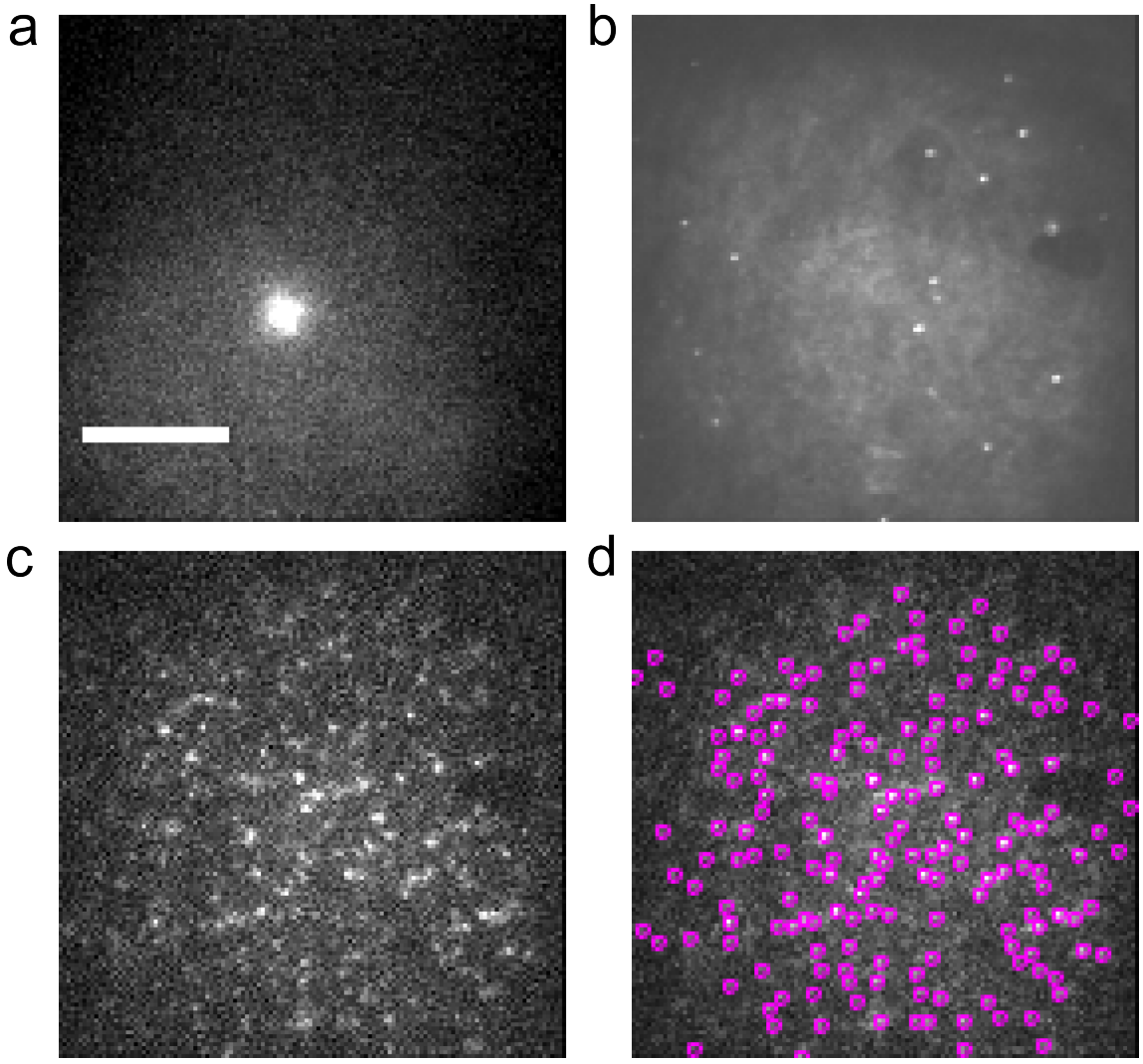


Figure 4.20: **Alamethicin (a)** Stack projection of the blue channel showing the location of one pore in the membrane. The applied voltage is -150 mV **(b)** Stack projection of the same area in the green channel showing the fluorescence from labelled peptide molecules. **(c)** Individual frame from green channel with labelled AMP molecules visible **(d)** Tracking procedure for a single frame in the green channel to obtain positions of peptides on the membrane surface. Purple circles are the spots selected by the tracking algorithm. Scale bar is 10 μm and the same for all images.

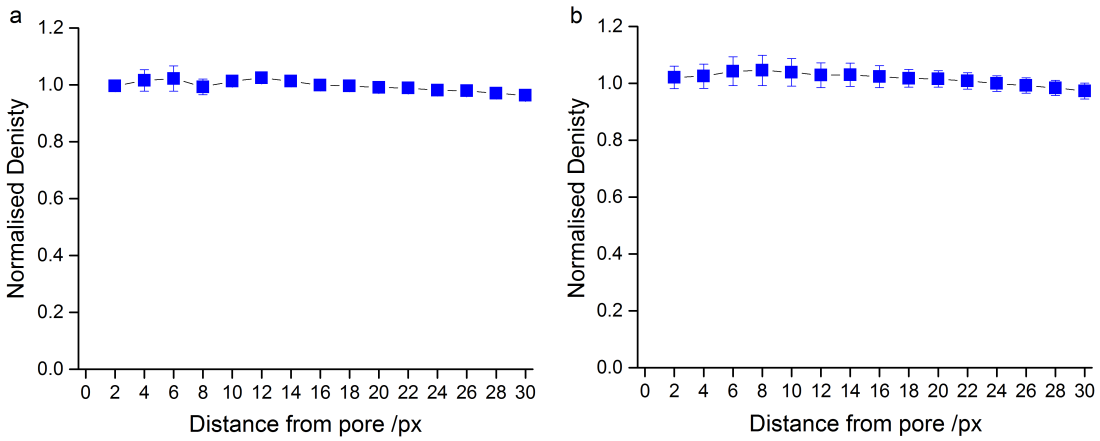


Figure 4.21: **Alamethicin (a)** Average RDF for 5 pores forming in the presence of alamethicin **(b)** Average control distribution for 5 locations with no pore formation. Error bars represent the standard deviation from the average of 5 data points. 1 pixel corresponds to 270 nm.

4.3.4.3 Spot count and diffusion analysis

The total spot count and diffusion constant for alamethicin with varying voltages are shown in Fig.4.22. There is a sharp decrease in spot count between 0 to -30 mV from about 100000 to 650000 count. Between -30 mV and -150 mV there are some fluc-

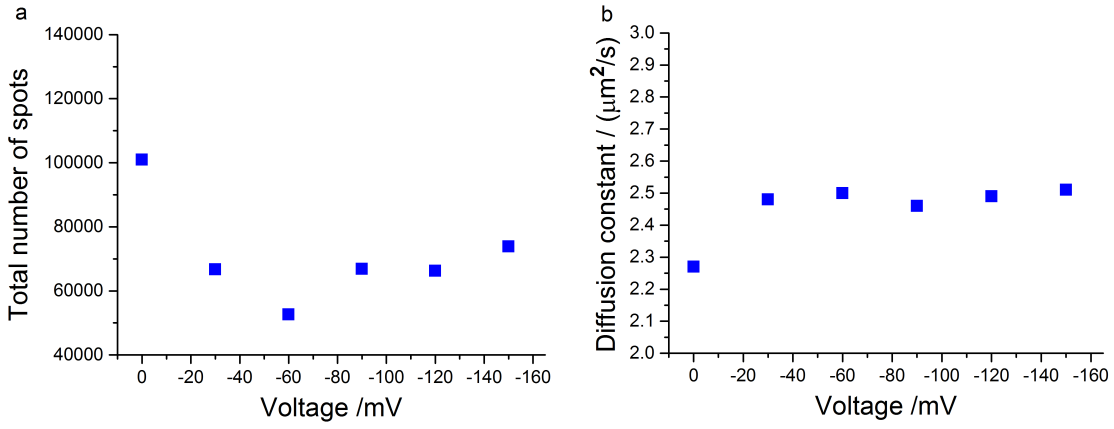


Figure 4.22: **Alamethicin (a)** Total spots identified in stack of 1000 frames depending on voltage.**(b)** Diffusion constant for each voltage calculated from 1000 frames. Each data point is calculated from only one dataset. Therefore errorbars do not apply.

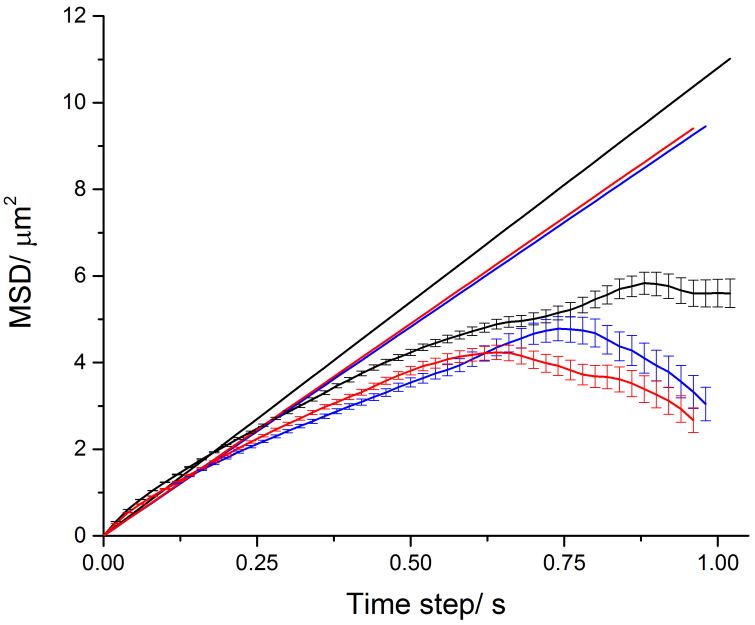


Figure 4.23: **Alamethicin** Mean square displacement of tracks against time steps. The data shown is for 0 mV (black), -90 mV (blue) and -150 mV (red). The lines are linear fits to each data set. Error bars are the standard deviation from the average for each time step.

tuations but the spot count remains in the region of 60000. Similarly, the diffusion constant increases from 2.25 $\mu m^2/s$ to 2.5 $\mu m^2/s$ between 0 and -30 mV. For the remaining voltages the diffusion constant ranges between 2.46- 2.51 $\mu m^2/s$. Apart from the initial increase, the diffusion constant of alamethicin molecules vary by no more than 2.5 % when increasing the voltage. The plots of mean square displacements against time steps in Fig.4.23 only show limited agreement with the fitted line up to 0.25 s. The relationship between mean square displacement and time steps appears non-linear. Therefore, the diffusion constants, which are proportional to the slope of the line, are mostly an overestimate of the actual behaviour of tracked spots. The tracking parameter for the analysis of this dataset are: Threshold=20, Spot diameter=3, Max linking distance=5, Min track length=3.

4.3.5 Indolicidin results

4.3.5.1 Imaging and tracking

The indolicidin concentration used for imaging is 11 μM unlabelled and 4 nM labelled peptide. The applied voltages are between -300 mV and -330 mV. At normal potentials, there were no poration events. Two pores are visible in Fig.4.24 and the Z-stack of the green channel shows an even fluorescence from labelled peptides. Pores are thought to be from normal electroporation and not caused by indolicidin. There are a few bright spots visible in the bilayer which indicate that some molecules were temporarily stuck in one location. None of the bright spots correspond to the locations of fluorescent spots in the blue channel, so they do not cause conductive pores. There is a distribution of intensities among the individual fluorescent spots. It is therefore possible that brighter spots represent complexes of more than one peptide. This could be analysed in more detail by carrying out an intensity calibration or by photobleaching of individual spots. Labelled molecules are tracked with the following parameters: Threshold=30, Spot diameter=3, Max linking distance=5, Min track length=3.

4.3.5.2 Radial distribution function

The RDFs are calculated to show the peptide distribution around the pore region. The distribution of peptides around 5 pores are averaged and the same is done for 5 control regions in the bilayer. Both RDFs show uniform distribution of peptides in the membrane region and therefore indicating no increase around the pore region.

4.3.5.3 Spot count and diffusion analysis

The total spot count and diffusion constants for indolicidin with varying voltages are shown in Fig.4.26. The spot count shows some irregularities with an increase

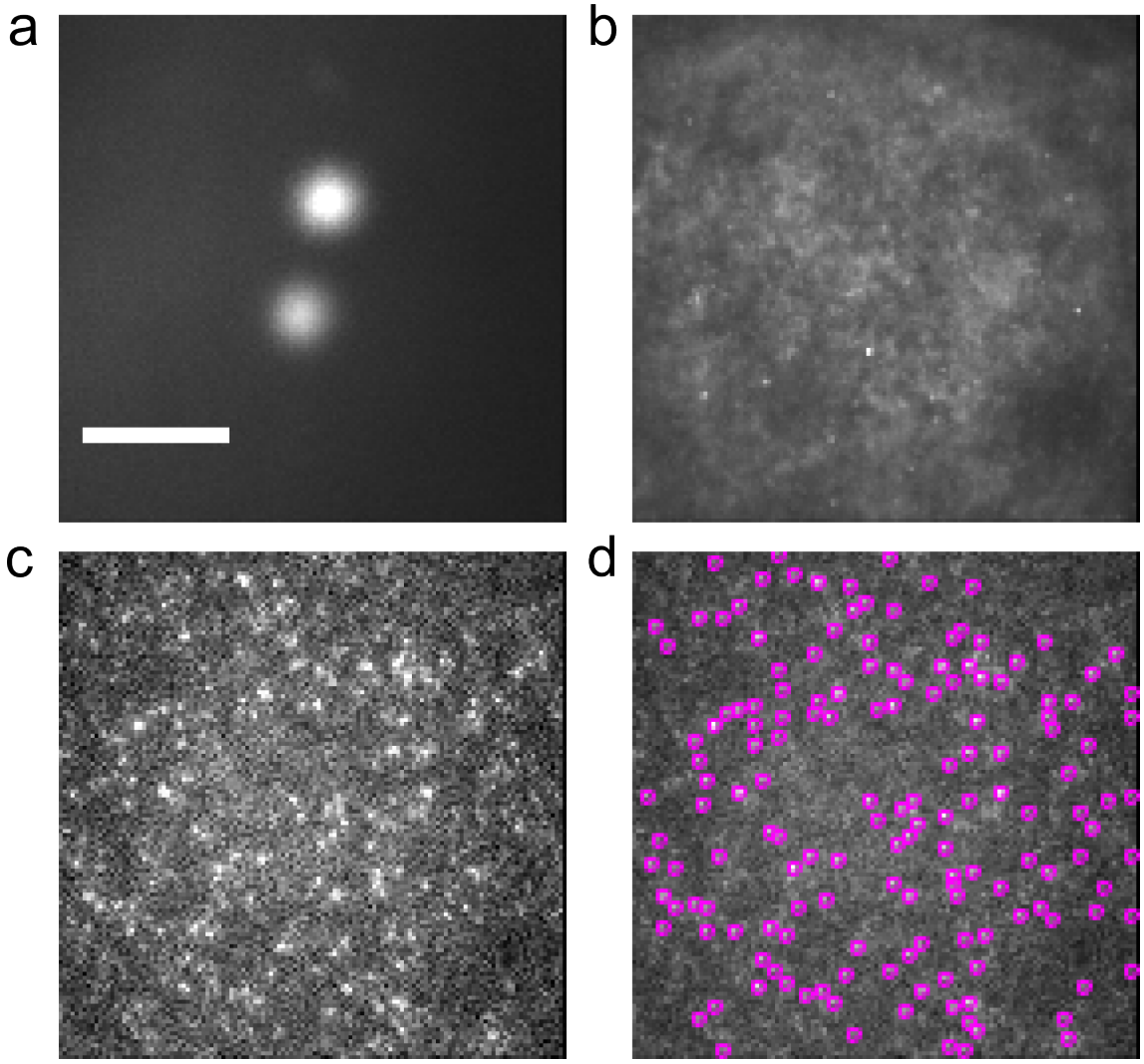


Figure 4.24: **Indolicidin (a)** Stack projection of the blue channel showing the location of two pores in the bilayer. The applied voltage is -300 mV **(b)** Stack projection of the same area in the green channel showing the fluorescence from labelled peptide molecules **(c)** Individual frame from green channel showing the presence of labelled AMP molecules **(d)** Tracking procedure for a single frame in the green channel to obtain positions of peptides on the membrane surface. Purple circles are the spots selected by the tracking algorithm. Scale bar is 10 μm and the same for all images.

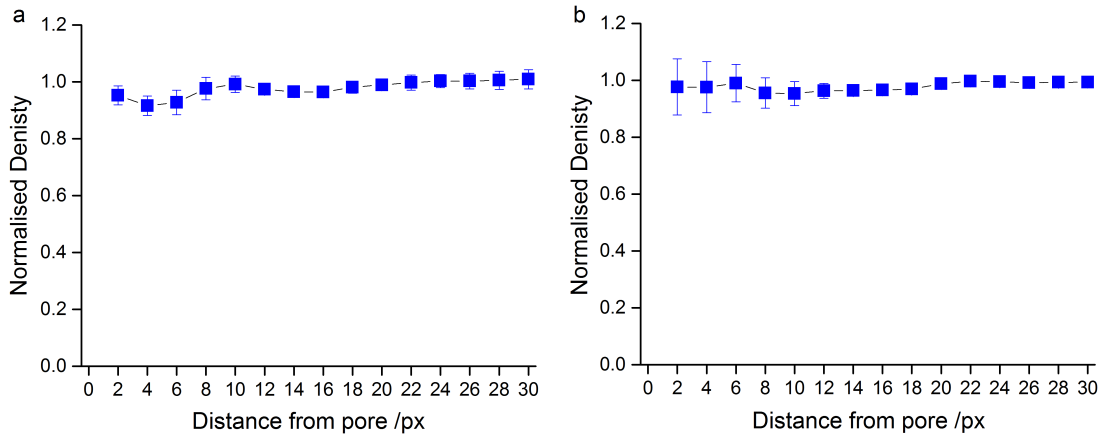


Figure 4.25: **Indolicidin (a)** Average RDF for 5 pores formed in bilayers in the presence of indolicidin **(b)** Average control distribution for 5 locations with no pore formation. Error bars represent the standard deviation from the average of 5 data points. 1 pixel corresponds to 270 nm.

between 0 and -30 mV and a decrease at -150 mV and -180 mV. There is no clear trend recognisable but there seems to be a decrease from -30 mV to -180 mV. The diffusion constant is fairly constant around 1.5 $\mu m^2/s$ with two increased values of 1.6 $\mu m^2/s$ at -60 mV and -180 mV. The plots of mean square displacements against time steps in Fig.4.27 only show limited agreement with the fitted line up to

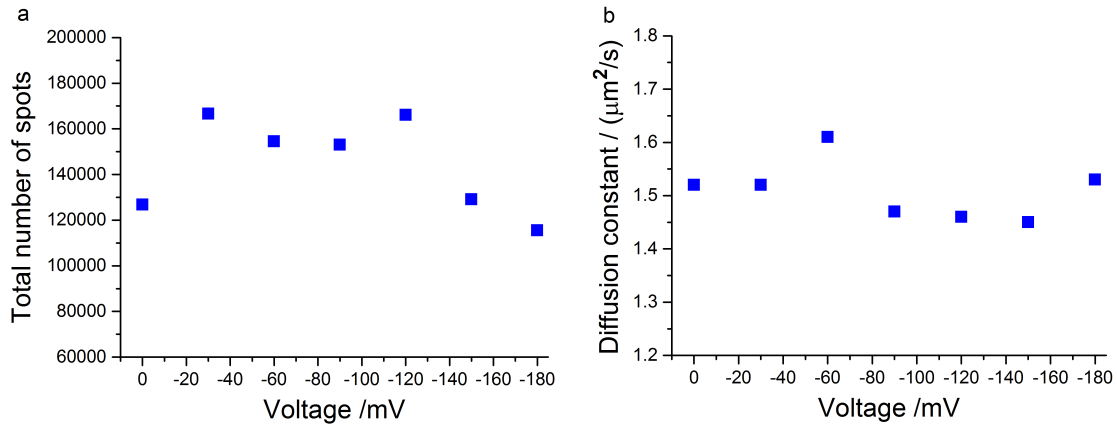


Figure 4.26: **Indolicidin (a)** Total spots identified in stack of 1000 frames depending on voltage.**(b)** Diffusion constant for each voltage calculated from 1000 frames. Each data point is calculated from only one dataset. Therefore errorbars do not apply.

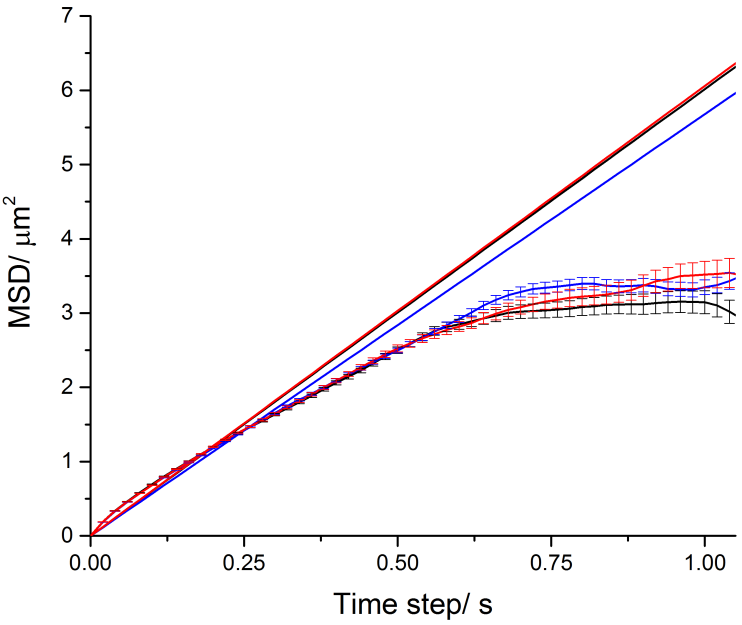


Figure 4.27: **Indolicidin** Mean square displacement of tracks against time steps. The data shown is for 0 mV (black), -90 mV (blue) and -180 mV (red). The lines are linear fits to each data set. Error bars are the standard deviation from the average for each time step.

0.25 s. The relationship between mean square displacement and time steps appears non-linear. Therefore, the diffusion constants, which are proportional to the slope of the line, are mostly an overestimate of the actual behaviour of tracked spots. The tracking parameter for the analysis of this dataset are: Threshold= 15, Spot diameter=3, Max linking distance=5, Min track length=3.

4.3.6 Discussion

The experiments described in this section show sequential imaging of pore locations and single AMP molecules in a DIB system. Imaging and analysis was carried out for four different AMPs using the same setup and image acquisition procedure. For all AMPs, pore locations could be easily identified using the highly sensitive calcium indicator dye Fluo-8, as shown in previous studies [97, 118, 33]. The pore behaviour

is similar for melittin and magainin 2. For both peptides, pores are stable on a scale between seconds to a few minutes. While some pores are very short-lived and transient, others are more stable. Alamethicin on the other hand, shows very well defined pores that remain stable for a long period of time once they have formed with a stable fluorescence signal from calcium-flux. This is agreement with a previous study on alamethicin [118]. Pores are also observed in the presence of indolicidin, but it is reasonable to assume that pore formation is not caused by indolicidin. Electrical studies in the previous section show that there is no relationship between indolicidin concentration and membrane permeation. Furthermore, pores are only observed above -200 mV, which is the region where normal electroporation occurs when using calcium substrates. All other pores are observed in the region of -90 mV to -150 mV. Since there is no significant electropore activity below -200 mV in the absence of peptides, it is safe to assume that the pores observed for magainin 2, melittin and alamethicin are caused by membrane interactions with those AMPs. All labelled peptides can be readily imaged at nanomolar concentration with green excitation. Z-stack projections of 1000 frames with single-molecules show a relatively uniform distribution of peptides in the membrane. For some projections (e.g. alamethicin) there are bright spots visible. These spots most likely represent aggregates formed of peptides. However, none of the spot projections coincide with fluorescent spots from calcium-flux imaging and it can therefore be concluded that they are not conductive pores. More likely, they arise from peptide molecules that are temporarily stuck under the membrane. None of the images indicate an increase in peptide density around pore locations which is confirmed by evaluating the tracks from single peptide molecules to calculate radial distribution functions around pore regions. All RDFs show a flat profile indicating a uniform distribution of peptide molecules that is unchanged around the pore location. For indolicidin this is expected, since it is not thought to be a pore forming peptide and acts on an intracellular level, which

requires binding to the membrane prior to entering the cell. The pore characteristics from calcium-flux imaging and the electrical data indicate a stable pore conformation with discrete conductance levels for alamethicin. It would therefore be expected to find an increase in peptide concentration due to complex formation. It should be noted that the available labelled peptide is only composed of the F50/7 isomer, whereas the unlabelled sample contains a mixture of F50/5 and F50/7. It is possible that alamethicin complexes preferentially form with F50/5 isomers. Further studies should be conducted using labelled isomers from both species to further investigate the possibility to image complex formation. Melittin and magainin 2 also show flat RDFs and therefore a uniform distribution of peptides bound to the membrane. The toroidal pore model has been suggested for both peptides and a two-state model with initial binding to the membrane followed by insertion is generally considered as their mode of action. While melittin and magainin 2 are clearly binding to the membrane surface and diffusing in 2D, there is no evidence of peptides accumulating around the pore region or showing an increased probability of being located around pore regions. The observations with calcium-flux on the other hand prove that conductive and stable pores are forming in the bilayer which are likely to be toroidal pores. Toroidal pores formed by melittin and magainin 2 are thought to be roughly on a scale of 1-10 nm which is much smaller than the the spatial resolution of 270 nm. [164, 203]. The number of peptides forming a toroidal pore is estimated to be between 4-8 so in principle one would expect a bright spot around the pore region [161]. However, it should be noted that the ratio of labelled to unlabelled peptides in solution is approximately 1:2500. The labelling ration was chosen to be low enough to allow identification of individual labelled molecules. The overall concentration was chosen to be high enough to cause pore formation which is based on electrical recordings performed in the first part of this chapter. Due to the low concentration of labelled peptides, there is only a small probability that labelled peptides are

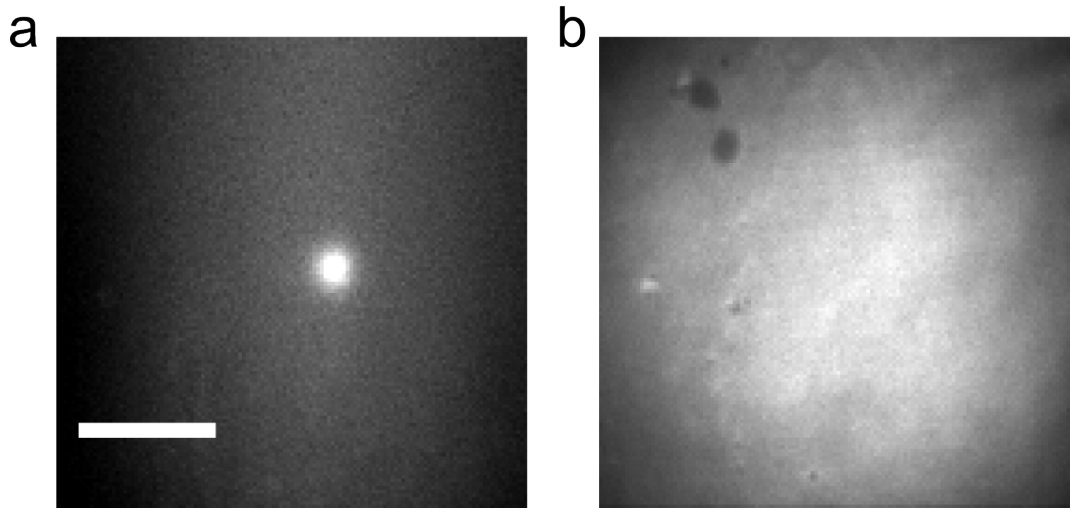


Figure 4.28: Dataset with 10 μM Melittin where 100% of the peptides are labelled. **(a)** Pore imaging with calcium-flux and blue excitation **(b)** Labelled peptide imaging with green excitation. Both images are z-stack projections for 1000 frames. Even when all peptides are labelled, there is no discernible increase in signal around the pore region. Scale bar is 10 μm and the same for both images.

actually present at pore. Performing an example calculation for a melittin dataset, the expected increase in signal is estimated by considering the ratio of peptides in a region covered by one pixel and the number of additional peptide due to the presence of a pore. From the number of tracked spots detected in the entire field of view, the total number of peptides present in the field of view can be estimated from the labelling ratio. From that number, it is estimated that there are on average 25 peptides (labelled and unlabelled) located in the bilayer area that corresponds to one pixel. Assuming that one pore consists of 5 peptides, the ratio $30/25 = 1.2$ predicts a 20% signal increase. The signal (intensity of fluorescent spots) to noise (standard deviation of overall signal over 1000 frames) ratio is $N/S = 0.43$ (43%), which is twice as large as the signal increase expected from a pore. Therefore it is unlikely to observe peptides forming a pore at this labelling ratio. At higher labelling ratios, the presence of labelled peptides in a pore should become more likely. However, experiments with 100% labelling also did not show any evidence for an increase in signal around a pore region (Fig.4.28) . At this labelling ratio the average noise to

base signal is $N/S = 0.06$ and a 20% change in signal due to pore formation should in principle be observable. Further investigation will be needed to clarify if the suggested pore models are valid. It should also be noted that the experiments shown here are constrained by the temporal resolution of image acquisition which is 50 Hz. Dynamic peptide binding and dissociation to form toroidal pores could happen on smaller time scales that are not resolvable with this camera setup. In addition, it has been suggested for melittin that toroidal pores only form in zwitterionic membranes together with cholesterol, whereas the carpet or detergent mechanism is prevalent in negatively charged membranes [162]. Changing the lipid composition in the system used here would show if any difference can be observed between both types of lipids. The spot count analysis generally shows a decrease in peptides bound to the surface when decreasing the voltage. On the other hand, applying a voltage clearly promotes pore formation and therefore the decrease in spots does not signify a decrease in peptide activity. The overall change is not more than 20% and concluded to be due to photobleaching of the dye label over the sequence of the experiment. This conclusion is based on the observation that the overall intensity decrease of the fluorescence signal ranges between 5-20%

Diffusion constants generally range between 1-3 $\mu m^2/s$ and are fairly constant with respect to different voltages. This shows that peptides are bound to the membrane and perform 2D-diffusion. Since the diffusion constant shows no dependence on the applied voltage, it is concluded that the increase in membrane permeability is not linked to increased peptide motility.

4.4 Conclusions

In this section an extensive study of the four AMPs melittin, magainin-2, alamethicin and indolicidon was described. Electrical characterisation showed concentra-

tion dependent membrane activity for melittin, magainin 2 and alamethicin. For indolicidin, no membrane activity was observed which is consistent with previous studies. Electrical studies in DIB system are straightforward and allow very easy manipulation of lipid composition, salt concentration as well as peptide concentration. This can easily be applied to other types of AMPs. Advantages compared to black lipid membranes are a smaller sample volume and higher stability of bilayers up to several hours or even days.

Based on the results of electrical measurements, the DIB system was modified to enable combined calcium-flux and single-molecule AMP imaging. The dual-colour setup of blue and green lasers allows flexible switching of excitation wavelength and is the first attempt to correlate pore and peptide locations in DIBs. The results generally indicate uniform peptide binding to the membrane surface. Indolicidin does not promote membrane permeation as shown by other studies. While no peptide complexes were observed for alamethicin, the stability of pores favours the barrel-stave model as shown previously [118]. While there is no direct evidence for toroidal pores from single-molecule data, the formation of punctate poration events indicates that toroidal pores are likely to be the mode of action for melittin and magainin 2. While further studies will be necessary, the results presented here indicated a mechanism where uniform peptide binding to the membrane surface is combined with barrel-stave (alamethicin) and toroidal pores (melittin and magainin 2).

Chapter 5

Conclusions and future work

The development of two novel experimental techniques for oSCR of individual pores in droplet interface bilayers are shown in this thesis. Fluorescence studies monitoring the concentration of potassium ions have so far only been realised in bulk or with efflux-assays but not on a single-channel level. Several applications of calcium-flux imaging have been published before, however not in combination with single-molecule imaging. There is so far one report on oSCR with alamethicin [118] and none involving melittin, magainin 2 or indolicidin. The results and limitations of both techniques are summarised below. Suggestions for improvements and future work are also discussed.

5.1 Potassium-flux imaging

Chapter 3 reported the successful implementation of an assay for potassium-flux imaging, resulting in the first ever observation of potassium-flux oSCR. Three indicator dyes were tested and it was concluded that APG-2 and APG-4 can be incorporated into the DIB system and both showed a clear signal around pore regions.

KS2 is in principle a potent indicator dye, but it requires the presence of Pluronic F-127 to increase solubility. The formation of stable bilayers was not possible in the presence of the surfactant and therefore KS2 was considered unsuitable for further investigation. The requirement of Pluronic is a major limitation for any future experiments involving lipid bilayer systems.

Detailed analysis was carried out for APG-4 to test the dye's limitations and the potential for applications involving potassium channels with smaller conductance. The signal response caused by an increase in potassium concentration makes pore regions clearly distinguishable. Analysis of the fluorescence profile shows that the time-scale of the dye response is in the region of 2.5-10 s. This comparatively slow response is a major limitation when considering channel-gating frequencies that are usually on a scale of milliseconds [140]. The second limitation becomes clear from the minimum detectable current which was estimated to be 2000 pA. Currents through single potassium channel usually range around 1-10 pA and can be detected with patch-clamping. This is several orders of magnitude smaller than the detectable current that is possible with APG-4. To conclude, there is a limitation with respect to temporal resolution as well as signal-to-background yield which makes oSCRs of potassium channels impossible with currently available dyes. Even attempts to image potassium-flux through α-hemolysin channels remained unsuccessful. For APG-2, no transmembrane conductance could be measured electrically in the presence of alpha-hemolysin, which is believed to be caused by blockage due to the presence of magnesium. Channel insertions were observed electrically in the presence of sodium, but given that α-hemolysin channels have a conductance of 900 pS, the current at -250 mV would be -225 pA which is roughly one order of magnitude lower than the minimum detectable current.

Despite the inability to extend this method to protein channels, the experimental method developed for the visualisation of electropores is a very important starting

point for any further attempt to improve potassium-flux imaging assays. Since it is the first ever realisation of potassium-flux oSCRs, future experiments can be based on the protocol presented here. The flexibility of the DIB setup would easily allow modifications of the experimental conditions to include novel potassium dyes that might have higher affinity and higher signal-to-noise response. It should also be noted that the results are the first report of oSCRs of electroporation. More detailed experiment on electroporation using calcium-flux imaging have been carried out in the lab and currently under review.

5.2 Pore formation and AMP imaging

Chapter 4 shows the first realisation of calcium-flux imaging through electropores combined with single-molecule AMP imaging. The setup was chosen to address the important question of pore formation by AMPs. The main models that have been proposed are the toroidal pore, carpet and barrel-stave model. Previous studies have either relied on pure electrical characterisation in model membranes, fluorescence efflux studies as well as structural methods such as X-Ray, NMR or oriented circular dichroism (OCD). While the barrel-stave model seems fairly accepted as the mode of action for alamethicin, the toroidal pore model for magianin 2 and melittin is more controversial. For a better understanding of pore formation due to peptide interactions, it is desirable to monitor peptide locations around a pore region in functional bilayers. The dual-colour setup allows rapid and flexible change of laser excitation with two channels respectively imaging calcium-flux through pores and fluorescently labelled AMPs in the membrane.

The initial electrical characterisation showed a clear increase in membrane permeation and lower stability in the presence alamethicin, magainin 2 and melittin. All

peptides showed activity at micromolar concentrations. Indolicidin, which has an intracellular mode of action, did not cause an increase in membrane activity and had a membrane stabilising effect. Binding of the peptides to the surface without forming pores most likely increases the stability of the bilayer during electrical recordings.

For all peptides, the images obtained from recording at blue and green laser excitation were compared by producing z-stack projections showing pore and peptide locations. This was followed by calculation of the radial distribution functions of tracked peptide molecules around the pore region for 5 datasets. Overall, there was no evidence for an increase in fluorescence and therefore peptide density in the region of pores, which would be expected when assuming a barrel-stave or toroidal pore model. For melittin and magainin 2, the pores appear more transient and in addition to stable pores, there are multiple pores that have a very short life-time. Punctate poration events observed with calcium-flux imaging demonstrate the formation of conductive pores which are likely to be toroidal. A detergent mechanism would result in rapid disintegration of the membrane structure whereas all experiments here show stable membranes with pore formation. The pore imaging data on alamethicin is consistent with previous results which were carried out with DPhPC bilayers [118]. Pores are very stable and remain in the same location for extended amounts of time indicating barrel-stave mechanism. Labelled alamethicin imaging does not show any evidence for an oligomer structure. It is possible that pores form preferentially from the F50/5 isomer. In that case, no increase would be detectable around the pore region, since the labelled sample used here only consists of F50/7. Pores in the presence of indolicidin only formed at very high voltages (-250 mV). In this region, pore formation is also observed in the absence of peptides and along with the electrical data, in can be concluded that indolicidin does not promote pore formation. There is a uniform distribution of peptides in the membrane. In order

to act on an intracellular level, indolicidin needs to traverse the membrane and it is expected that it binds to the membrane surface prior to insertion.

There are a number of future experiments that are required to further solidify and extend the results obtained here. While there are reasons to conclude a toroidal pore mechanism for magainin 2 and melittin, more direct evidence is needed to substantiate this mode of action. Recordings with higher time resolution than 20 ms would be able to show if the dynamics of the pore forming process are faster than observable here. Higher ratios of labelled to unlabelled peptides could also be chosen to achieve higher probabilities of observing a signal increase from peptide imaging of the pore region. A previous study suggested that toroidal pores for melittin only form in zwitterionic membranes [162]. Repeating the experiments with zwitterionic lipids such as DPhPC or DOPC would allow a comparison with the mix of zwitterionic and negatively charged lipids that was chosen here. For alamethicin, further work is needed to attempt imaging of pore-complexes. Should this be realised, the number of monomers forming a pore could be determined with photobleaching. Using the same species of labelled and unlabelled alamethicin would exclude the possibility of complex formation by only one isomer. The most interesting aspect of indolicidin is the mechanism of intracellular killing and the required crossing of the bilayer. Labelled indolicidin could be added to the substrate-side of the membrane to observe if there is an increase in fluorescence over time in the droplet due to indolicidin molecules going through the bilayer. This could also be monitored by submerging vesicles into a solution with high concentration of labelled indolicidin and imaging the fluorescence inside the vesicles over time.

It would also be interesting to show if peptides have an increased binding affinity to curved regions. It has been shown that the human defensin LL-37 preferentially binds to highly curved regions in *E.coli* cells [204]. Furthermore, it has been suggested that melittin and magainin 2 induce positive curvature strain on membranes

[205]. Preliminary experiments with curved substrates have been carried out in the lab and could be used to determine the binding of labelled peptides around curved regions.

Melittin has been shown to induce phase separation in DPPG rich membranes [206]. The effect of AMPs on phase separation could be determined with the DIB system used in this thesis (in a recent publication, phase separation was visualised in DIBs [207]). Labelled AMPs could be used to test if there is preferential binding to the liquid-ordered or liquid-disordered phase.

5.3 Summary

The techniques developed in this thesis are an important contribution to the field of oSCR. Potassium-flux imaging through individual electropores and calcium-flux combined with single-molecule imaging of labelled AMPs are reported for the first time. It is hoped that the experiments carried out here will provide a foundation for further studies and improvements of oSCR that will lead to a better understanding of potassium channels and pore formation of AMPs.

5.4 Publications

- Marc Szabo and Mark I Wallace. Imaging potassium- flux through individual electropores in droplet interface bilayers. *Biochimica et Biophysica Acta (BBA)-Biomembranes*, 2015 (Accepted for publication on 20 July 2015)

- Marc Szabo, Jason T Sengel and Mark I Wallace. Analysis of pore formation by antimicrobial peptides with combined calcium-flux and single-molecule imaging (in preparation, not submitted)

Bibliography

[1] Eva Bianconi, Allison Piovesan, Federica Facchin, Alina Beraudi, Raffaella Casadei, Flavia Frabetti, Lorenza Vitale, Maria Chiara Pelleri, Simone Tassani, Francesco Piva, Soledad Perez-Amodio, Pierluigi Strippoli, and Silvia Canaider. An estimation of the number of cells in the human body. *Annals of human biology*, 40(6):463–71, 2014.

[2] F.M. Ashcroft. *Ion Channels and Disease*. Elsevier Science, 1999.

[3] P R Cullis and B de Kruijff. Lipid polymorphism and the functional roles of lipids in biological membranes. *Biochimica et biophysica acta*, 559(4):399–420, 1979.

[4] Dan D. Lasic. Novel applications of liposomes. *Trends in Biotechnology*, 16(7):307–321, 1998.

[5] *LIPID MAPS Database*, 2016 (accessed May 4, 2016). `http://www.lipidmaps.org/data/structure/index.html`.

[6] Eoin Fahy, Shankar Subramaniam, H Alex Brown, Christopher K Glass, Alfred H Merrill, Robert C Murphy, Christian R H Raetz, David W Russell, Yousuke Seyama, Walter Shaw, Takao Shimizu, Friedrich Spener, Gerrit van Meer, Michael S VanNieuwenhze, Stephen H White, Joseph L Witztum, and

Edward a Dennis. A comprehensive classification system for lipids. *Journal of lipid research*, 46:839–861, 2005.

[7] Rob Phillips, Jane Kondev, Julie Theriot, and Hernan Garcia. *Physical biology of the cell*. Garland Science, 2012.

[8] Donald Voet and Judith G Voet. Biochemistry, 4-th edition. *NewYork: John Wiley& SonsInc*, pages 492–496, 2011.

[9] Eeman M, Deleu M, Marc Eeman, and Magali Deleu. From biological membranes to biomimetic model membranes. *Focus*, 14(4):719–736, 2010.

[10] Gerrit van Meer, Dennis R. Voelker, and Gerald W. Feigenson. Membrane lipids: where they are and how they behave. *Nature Reviews Molecular Cell Biology*, 9(2):112–124, 2008.

[11] W. Dowhan. MOLECULAR BASIS FOR MEMBRANE PHOSPHOLIPID DIVERSITY:Why Are There So Many Lipids? *Annual Review of Biochemistry*, 66(1):199–232, 1997.

[12] Martin Loose and Petra Schwille. Biomimetic membrane systems to study cellular organization. *Journal of Structural Biology*, 168(1):143–151, 2009.

[13] P Mueller, D O Rudin, H T Tien, and W C Wescott. Reconstitution of cell membrane structure in vitro and its transformation into an excitable system. *Nature*, 194:979–980, 1962.

[14] M Montal and P Mueller. Formation of bimolecular membranes from lipid monolayers and a study of their electrical properties. *Proceedings of the National Academy of Sciences of the United States of America*, 69(12):3561–6, December 1972.

[15] E. Bamberg, H. Alpes, H. J. Apell, R. Bradley, B. Härter, M. J. Quelle, and D. W. Urry. Formation of ionic channels in black lipid membranes by succinic derivatives of Gramicidin A. *The Journal of Membrane Biology*, 50(3-4):257–270, 1979.

[16] Patrick Van Gelder, Fabrice Dumas, and Mathias Winterhalter. Understanding the function of bacterial outer membrane channels by reconstitution into black lipid membranes. *Biophysical Chemistry*, 85(2-3):153–167, 2000.

[17] G. Belmonte, L. Cescatti, B. Ferrari, T. Nicolussi, M. Ropele, and G. Menestrina. Pore formation by Staphylococcus aureus alpha-toxin in lipid bilayers. *European Biophysics Journal*, 14(6):349–358, 1987.

[18] Mathias Winterhalter. Black lipid membranes. *Current Opinion in Colloid and Interface Science*, 5(3-4):250–255, 2000.

[19] E Castellana and P Cremer. Solid supported lipid bilayers: From biophysical studies to sensor design. *Surface Science Reports*, 61(10):429–444, 2006.

[20] Xiao Feng Kang, Stephen Cheley, Allison C. Rice-Ficht, and Hagan Bayley. A storable encapsulated bilayer chip containing a single protein nanopore. *Journal of the American Chemical Society*, 129(21):4701–4705, 2007.

[21] M.R.R. de Planque. Controlled delivery of membrane proteins to artificial lipid bilayers by nystatin–ergosterol modulated vesicle fusion. *IEE Proceedings - Nanobiotechnology*, 153:21–30(9), April 2006.

[22] Michele Zagnoni, Mairi E Sandison, Phedra Marius, Anthony G Lee, and Hywel Morgan. Controlled delivery of proteins into bilayer lipid membranes on chip. *Lab on a chip*, 7(9):1176–1183, 2007.

[23] Matthew a Holden and Hagan Bayley. Direct Introduction of Single Protein Channels and Pores into Lipid Bilayers. *Society*, 127(18):6502–6503, 2005.

[24] Matthew A Holden, Lakmal Jayasinghe, Oliver Daltrop, Amy Mason, and Hagan Bayley. Direct transfer of membrane proteins from bacteria to planar bilayers for rapid screening by single-channel recording. *Nature Chemical Biology*, 2(6):314–318, 2006.

[25] Thomas Gutsmann, Thomas Heimburg, Ulrich Keyser, Kozhinjampara R Mahendran, and Mathias Winterhalter. Protein reconstitution into freestanding planar lipid membranes for electrophysiological characterization. *Nature protocols*, 10(1):188–98, 2015.

[26] Yee-Hung M Chan and Steven G Boxer. Model membrane systems and their applications. *Current Opinion in Chemical Biology*, 11(6):581–587, 2007.

[27] Simon G. Patching. Surface plasmon resonance spectroscopy for characterisation of membrane protein–ligand interactions and its potential for drug discovery. *Biochimica et Biophysica Acta (BBA) - Biomembranes*, 1838(1):43–55, 2014.

[28] Marie-Paule Mingeot-Leclercq, Magali Deleu, Robert Brasseur, and Yves F Dufrêne. Atomic force microscopy of supported lipid bilayers. *Nature protocols*, 3(10):1654–1659, 2008.

[29] a Sonnleitner, G J Schütz, and T Schmidt. Free Brownian motion of individual lipid molecules in biomembranes. *Biophysical journal*, 77(November):2638–2642, 1999.

[30] J.Y. Wong, J. Majewski, M. Seitz, C.K. Park, J.N. Israelachvili, and G.S. Smith. Polymer-Cushioned Bilayers. I. A Structural Study of Various Prepara-

tion Methods Using Neutron Reflectometry. *Biophysical Journal*, 77(3):1445–1457, 1999.

[31] James R Thompson, Andrew J Heron, Yusdi Santoso, and Mark I Wallace. Enhanced stability and fluidity in droplet on hydrogel bilayers for measuring membrane protein diffusion. *Nano letters*, 7(12):3875–8, dec 2007.

[32] Andrew J. Heron, James R. Thompson, Amy E. Mason, and Mark I. Wallace. Direct detection of membrane channels from gels using water-in-oil droplet bilayers. *Journal of the American Chemical Society*, 129(51):16042–16047, 2007.

[33] Andrew J Heron, James R Thompson, Bríd Cronin, Hagan Bayley, and Mark I Wallace. Simultaneous measurement of ionic current and fluorescence from single protein pores. *Journal of the American Chemical Society*, 131(5):1652–3, February 2009.

[34] Sebastian Leptihn, Oliver K Castell, Brid Cronin, En-Hsin Lee, Linda C M Gross, David P Marshall, James R Thompson, Matthew Holden, and Mark I Wallace. Constructing droplet interface bilayers from the contact of aqueous droplets in oil. *Nature protocols*, 8(6):1048–57, June 2013.

[35] Hagan Bayley, Brid Cronin, Andrew Heron, Matthew a Holden, William L Hwang, Ruhma Syeda, James Thompson, and Mark Wallace. Droplet interface bilayers. *Molecular bioSystems*, 4(12):1191–208, December 2008.

[36] Tudor Luchian. The modulatory effect of calcium ions upon alamethicin monomers uptake on artificial phospholipid membranes. *Journal of Biological Physics*, 31(1):23–33, 2005.

[37] B. Eisenberg. Ionic channels in biological membranes: natural nanotubes described\nby the drift-diffusion equations. *1998 Sixth International Work-*

shop on Computational Electronics. Extended Abstracts (Cat. No.98EX116), 4842(95):117–123, 1998.

[38] Michael Zasloff. Antimicrobial peptides of multicellular organisms. *Nature*, 415(6870):389–395, January 2002.

[39] Jessica Olofsson, Kerstin Nolkrantz, Frida Ryttsén, Bradley a Lambie, Stephen G Weber, and Owe Orwar. Single-cell electroporation. *Current Opinion in Biotechnology*, 14(1):29–34, February 2003.

[40] Hiroshi Hibino, Atsushi Inanobe, Kazuharu Furutani, Shingo Murakami, and I A N Findlay. Inwardly Rectifying Potassium Channels : Their Structure , Function , and Physiological Roles. pages 291–366, 2010.

[41] Simon Bernèche and Benoît Roux. A gate in the selectivity filter of potassium channels. *Structure (London, England : 1993)*, 13(4):591–600, April 2005.

[42] Serdar Kuyucak and Turgut Bastug. Physics of ion channels. *Journal of biological physics*, 29(4):429–46, dec 2003.

[43] Roderick MacKinnon. Potassium channels. *FEBS Letters*, 555(1):62–65, 2003.

[44] Vassiliy N Bavro, Rita De Zorzi, Matthias R Schmidt, João R C Muniz, Lejla Zubcevic, Mark S P Sansom, Catherine Vénien-Bryan, and Stephen J Tucker. Structure of a KirBac potassium channel with an open bundle crossing indicates a mechanism of channel gating. *Nature structural & molecular biology*, 19(2):158–63, February 2012.

[45] Eve E Weatherill and Mark I Wallace. Combining Single-Molecule Imaging and Single-Channel Electrophysiology. *Journal of molecular biology*, (3), jul 2014.

[46] Paul R Selvin. Lighting up single ion channels. *Biophysical journal*, 84(1):1–2, January 2003.

[47] T Y Tsong. Electroporation of cell membranes. *Biophysical journal*, 60(2):297–306, 1991.

[48] C Huang, L Wheeldon, and T E Thompson. The Properties of Lipid Bilayer Membranes Separating Two Aqueous Phases: Formation of a Membrane of Simple Composition. *Journal of molecular biology*, 8(1):148–160, 1964.

[49] J M Crowley. Electrical breakdown of bimolecular lipid membranes as an electromechanical instability. *Biophysical journal*, 13:711–724, 1973.

[50] I.G. Abiror, V.B. Arakelyan, L.V. Chernomordik, Yu.A. Chizmadzhev, V.F. Pastushenko, and M.R. Tarasevich. Electric breakdown of bilayer lipid membranes I. The main experimental facts and their qualitative discussion. *Bioelectrochemistry and Bioenergetics*, 6(1):37–52, 1979.

[51] S. Kakorin, E. Redeker, and E. Neumann. Electroporative deformation of salt filled lipid vesicles. *European Biophysics Journal*, 27(1):43–53, 1998.

[52] J Teissie and T Y Tsong. Electric field induced transient pores in phospholipid bilayer vesicles. *Biochemistry*, 20(6):1548–1554, 1981.

[53] S Raffy and J Teissie. Insertion of glycophorin A, a transmembraneous protein, in lipid bilayers can be mediated by electropermeabilization. *Eur J Biochem*, 230(2):722–732, 1995.

[54] J. Teissie, M. Golzio, and M.P. Rols. Mechanisms of cell membrane electropermeabilization: A minireview of our present (lack of ?) knowledge. *Biochimica et Biophysica Acta (BBA) - General Subjects*, 1724(3):270–280, 2005.

[55] Muriel Golzio, Justin Teissie, and Marie-Pierre Rols. Direct visualization at the single-cell level of electrically mediated gene delivery. *Proceedings of the National Academy of Sciences of the United States of America*, 99(3):1292–7, February 2002.

[56] C Chen, S W Smye, M P Robinson, and J a Evans. Membrane electroporation theories: a review. *Medical & biological engineering & computing*, 44(1-2):5–14, March 2006.

[57] John Neu and Wanda Krassowska. Asymptotic model of electroporation. *Physical Review E*, 59(3):3471–3482, 1999.

[58] T. John Lewis. A Model for Bilayer Membrane Electroporation Based on Resultant Electromechanical Stress. *IEEE Transactions on Dielectrics and Electrical Insulation*, 10(5):769–777, 2003.

[59] R J Dubos. Studies on a bactericidal agent extracted from a soil bacillus: I. Preparation of the agent. Its activity in vitro. *The Journal of experimental medicine*, 70(1):1–10, 1939.

[60] R C Skarnes and D W Watson. Antimicrobial factors of normal tissues and fluids. *Bacteriological reviews*, 21(4):273–294, 1957.

[61] Guangshun Wang. Database-Guided Discovery of Potent Peptides to Combat HIV-1 or Superbugs. *Pharmaceuticals*, 6(6):728–758, 2013.

[62] Nannette Y. Yount, Arnold S. Bayer, Yan Q. Xiong, and Michael R. Yeaman. Advances in antimicrobial peptide immunobiology. *Peptide Science*, 84(5):435–458, 2006.

[63] Yechiel Shai. Mechanism of the binding, insertion and destabilization of phospholipid bilayer membranes by alpha-helical antimicrobial and cell non-

selective membrane-lytic peptides. *Biochimica et Biophysica Acta - Biomembranes*, 1462(1-2):55–70, 1999.

[64] Katsumi Matsuzaki. Why and how are peptide–lipid interactions utilized for self-defense? Magainins and tachyplesins as archetypes. *Biochimica et Biophysica Acta (BBA) - Biomembranes*, 1462(1-2):1–10, 1999.

[65] Gerrit van Meer, Dennis R. Voelker, and Gerald W. Feigenson. Membrane lipids: where they are and how they behave. *Nature Reviews Molecular Cell Biology*, 9(2):112–124, 2008.

[66] Georgi Beschiaschvili and Joachim Seelig. Melittin binding to mixed phosphatidylglycerol/phosphatidylcholine membranes. *Biochemistry*, 29(1):52–58, 1990.

[67] Kim A. Brogden. Antimicrobial peptides: pore formers or metabolic inhibitors in bacteria? *Nature Reviews Microbiology*, 3(3):238–250, 2005.

[68] Burkhard Bechinger. Structure and Function of Membrane-Lytic Peptides. *Critical Reviews in Plant Sciences*, 23(3):271–292, 2004.

[69] R J Taylor and R de Levie. "Reversed" alamethicin conductance in lipid bilayers. *Biophysical journal*, 59(4):873–9, 1991.

[70] M S Sansom. Alamethicin and related peptaibols–model ion channels. *European biophysics journal : EBJ*, 22(2):105–24, 1993.

[71] M T Tosteson and D C Tosteson. The sting. Melittin forms channels in lipid bilayers. *Biophysical journal*, 36(1):109–116, 1981.

[72] S. J. Ludtke, K. He, Y. Wu, and H. W. Huang. Cooperative membrane insertion of magainin correlated with its cytolytic activity. *Biochimica et Biophysica Acta - Biomembranes*, 1190(1):181–184, 1994.

[73] Beatrice Haimovich and Jacqueline C. Tanaka. Magainin-induced cytotoxicity in eukaryotic cells: kinetics, dose-response and channel characteristics. *Biochimica et Biophysica Acta (BBA) - Biomembranes*, 1240(2):149–158, 1995.

[74] C Subbalakshmi. Mechanism of antimicrobial action of indolicidin. *FEMS Microbiology Letters*, 160(1):91–96, 1998.

[75] Burkhard Bechinger and Karl Lohner. Detergent-like actions of linear amphipathic cationic antimicrobial peptides. *Biochimica et Biophysica Acta (BBA) - Biomembranes*, 1758(9):1529–1539, 2006.

[76] Michael Zasloff. Antimicrobial peptides in health and disease. *New England Journal of Medicine*, 347(15):1199–1200, 2002. PMID: 12374882.

[77] L. Ryan, B. Lamarre, T. Diu, J. Ravi, P. J. Judge, A. Temple, M. Carr, E. Cerasoli, B. Su, H. F. Jenkinson, G. Martyna, J. Crain, A. Watts, and M. G. Ryadnov. Anti-antimicrobial Peptides: FOLDING-MEDIATED HOST DEFENSE ANTAGONISTS. *Journal of Biological Chemistry*, 288(28):20162–20172, 2013.

[78] Jeffrey L Fox. Antimicrobial peptides stage a comeback. *Nature Biotechnology*, 31(5):379–382, 2013.

[79] Eduardo Guaní-Guerra, Teresa Santos-Mendoza, Saúl O. Lugo-Reyes, and Luis M. Terán. Antimicrobial peptides: General overview and clinical implications in human health and disease. *Clinical Immunology*, 135(1):1–11, 2010.

[80] John Dunlop, Mark Bowlby, Ravikumar Peri, Dmytro Vasilyev, and Robert Arias. High-throughput electrophysiology: an emerging paradigm for ion-

channel screening and physiology. *Nature reviews. Drug discovery*, 7(4):358–68, April 2008.

[81] ERWIN NEHER and BERT SAKMANN. Single-channel currents recorded from membrane of denervated frog muscle fibres. *Nature*, 260(5554):799–802, April 1976.

[82] O P Hamill, A Marty, E Neher, B Sakmann, and F J Sigworth. Improved patch-clamp techniques for high-resolution current recording from cells and cell-free membrane patches. *Pflügers Archiv : European Journal of Physiology*, 391(2):85–100, 1981.

[83] Sophie Demarche, Kaori Sugihara, Tomaso Zambelli, Louis Tiefenauer, and Janos Vörös. Techniques for recording reconstituted ion channels. *The Analyst*, 136(6):1077–89, mar 2011.

[84] B Sakmann and E Neher. Patch clamp techniques for studying ionic channels in excitable membranes. *Annual review of physiology*, 46:455–472, 1984.

[85] Markéta Bébarová. Advances in patch clamp technique: towards higher quality and quantity. *General physiology and biophysics*, 31(2):131—140, June 2012.

[86] H Duclohier, G Molle, and G Spach. Antimicrobial peptide magainin I from Xenopus skin forms anion-permeable channels in planar lipid bilayers. *Biophysical journal*, 56(5):1017–21, 1989.

[87] Enrico Gallucci, Daniela Meleleo, Silvia Micelli, and Vittorio Picciarelli. Magainin 2 channel formation in planar lipid membranes: the role of lipid polar groups and ergosterol. *European biophysics journal : EBJ*, 32(1):22–32, 2003.

[88] M Pawlak, S Stankowski, and G Schwarz. Melittin induced voltage-dependent conductance in DOPC lipid bilayers. *Biochimica et biophysica acta*, 1062(1):94–102, 1991.

[89] R. J. Bradley, D. W. Urry, R. Rapaka, and K. Okamoto. Channel Structures of Gramicidin : Characterization of Succinyl Derivatives. *Science*, pages 435–437, 1978.

[90] Ashish Arora, Dennis Rinehart, Gabor Szabo, and Lukas K. Tamm. Refolded Outer Membrane Protein A of Escherichia coliForms Ion Channels with Two Conductance States in Planar Lipid Bilayers. *J. Biol. Chem.*, 275(3):1594–1600, 2000.

[91] Ruhma Syeda, Matthew a Holden, William L Hwang, and Hagan Bayley. Screening Blockers Against a Potassium Channel with a Droplet Interface Bilayer Array. *Journal of the American Chemical Society*, 130(36):SI 1–5, 2008.

[92] Physical encapsulation of droplet interface bilayers for durable, portable biomolecular networks. *Lab on a chip*, 10(6):710–7, 2010.

[93] Matthew a. Holden, David Needham, and Hagan Bayley. Functional bionetworks from nanoliter water droplets. *Journal of the American Chemical Society*, 129(27):8650–8655, 2007.

[94] Sebastian Leptihn, James R Thompson, J Clive Ellory, Stephen J Tucker, and Mark I Wallace. In vitro reconstitution of eukaryotic ion channels using droplet interface bilayers. *Journal of the American Chemical Society*, 133(24):9370–5, June 2011.

[95] Angelo Demuro and Ian Parker. Optical single-channel recording: imaging Ca2+ flux through individual N-type voltage-gated channels expressed in Xenopus oocytes. *Cell Calcium*, 34(6):499–509, December 2003.

[96] Elena Molokanova and Alex Savchenko. Bright future of optical assays for ion channel drug discovery. *Drug discovery today*, 13(1-2):14–22, January 2008.

[97] Oliver K Castell, James Berridge, and Mark I Wallace. Quantification of membrane protein inhibition by optical ion flux in a droplet interface bilayer array. *Angewandte Chemie (International ed. in English)*, 51(13):3134–8, March 2012.

[98] Shi-qiang Wang, Long-sheng Song, and Edward G Lakatta. Ca 2 + signalling between single L-type Ca 2 + channels and ryanodine receptors in heart cells. 410(MARCH), 2001.

[99] S Peng, N G Publicover, J a Airey, J E Hall, H T Haigler, D Jiang, S R Wayne Chen, and J L Sutko. Diffusion of single cardiac ryanodine receptors in lipid bilayers is decreased by annexin 12. *Biophysical journal*, 86(1 Pt 1):145–51, January 2004.

[100] Stanley A Thayer, Michael Sturek, and Richard J Miller. Measurement of neuronal Ca 2 + transients using simultaneous microfluorimetry and electrophysiology. pages 216–223, 1988.

[101] Angelo Demuro and Ian Parker. "Optical patch-clamping": single-channel recording by imaging Ca2+ flux through individual muscle acetylcholine receptor channels. *The Journal of general physiology*, 126(3):179–92, September 2005.

[102] Angelo Demuro, Martin Smith, and Ian Parker. Single-channel Ca(2+) imaging implicates Aβ1-42 amyloid pores in Alzheimer's disease pathology. *The Journal of cell biology*, 195(3):515–24, October 2011.

[103] Toshihisa Osaki, Hiroaki Suzuki, Bruno Le Pioufle, and Shoji Takeuchi. Multichannel Simultaneous Measurements of Single-Molecule Translocation in r -Hemolysin Nanopore Array. 81(24):9866–9870, 2009.

[104] Douglas C. Rees, Geoffrey Chang, and Robert H. Spencer. Crystallographic analyses of ion channels: Lessons and challenges. *Journal of Biological Chemistry*, 275(2):713–716, 2000.

[105] S Weiss. Measuring conformational dynamics of biomolecules by single molecule fluorescence spectroscopy. *Nature structural biology*, 7(9):724—729, September 2000.

[106] V Borisenko, T Lougheed, J Hesse, E Füreder-Kitzmüller, N Fertig, J C Behrends, G A Woolley, and G J Schütz. Simultaneous optical and electrical recording of single gramicidin channels. *Biophysical journal*, 84(1):612–22, 2003.

[107] Linda C M Gross, Oliver K Castell, and Mark I Wallace. Dynamic and Reversible Control of 2D Membrane Protein. 2011.

[108] Joseph R Lakowicz. *Principles of fluorescence spectroscopy*. Springer Science & Business Media, 2013.

[109] D. Axelrod. Cell-substrate contacts illuminated by total internal reflection fluorescence. *Journal of Cell Biology*, 89(1):141–145, 1981.

[110] Adam J. M. Wollman, Richard Nudd, Erik G. Hedlund, and Mark C. Leake. From animaculum to single molecules: 300 years of the light microscope. *Open Biology*, 5(4), 2015.

[111] Marco Mongillo, Rosario Rizzuto, and Tullio Pozzan. Looking forward to seeing calcium. 4(July), 2003.

[112] BG Clark. An efficient implementation of the algorithm'clean'. *Astronomy and Astrophysics*, 89:377, 1980.

[113] Johannes Schindelin, Ignacio Arganda-Carreras, Erwin Frise, Verena Kaynig, Mark Longair, Tobias Pietzsch, Stephan Preibisch, Curtis Rueden, Stephan Saalfeld, Benjamin Schmid, Jean-Yves Tinevez, Daniel James White, Volker Hartenstein, Kevin Eliceiri, Pavel Tomancak, and Albert Cardona. Fiji: an open-source platform for biological-image analysis. *Nat Meth*, 9(7):676–682, July 2012.

[114] *Trackmate online documentation*, 2015 (accessed December 9, 2015). `http://fiji.sc/Getting_started_with_TrackMate`.

[115] Hui Kong, Hatice Cinar Akakin, and Sanjay E. Sarma. A generalized laplacian of gaussian filter for blob detection and its applications. *IEEE Transactions on Cybernetics*, 43(6):1719–1733, 2013.

[116] Nick Efford. *Digital image processing: a practical introduction using java (with CD-ROM)*. Addison-Wesley Longman Publishing Co., Inc., 2000.

[117] Khuloud Jaqaman, Dinah Loerke, Marcel Mettlen, Hirotaka Kuwata, Sergio Grinstein, Sandra L Schmid, and Gaudenz Danuser. Robust single-particle tracking in live-cell time-lapse sequences. *Nature Methods*, 5(8):695–702, 2008.

[118] Lydia M. Harriss, Bríd Cronin, James R. Thompson, and Mark I. Wallace. Imaging multiple conductance states in an alamethicin pore. *J. Am. Chem. Soc.*, 133(37):14507–14509, 2011.

[119] Hugues Abriel and Elena V. Zaklyazminskaya. Cardiac channelopathies: Genetic and molecular mechanisms. *Gene*, 517(1):1–11, 2013.

[120] Amiel a Dror and Karen B Avraham. Hearing loss: mechanisms revealed by genetics and cell biology. *Annual review of genetics*, 43:411–437, 2009.

[121] Sarah Weckhuysen, Simone Mandelstam, Arvid Suls, Dominique Audenaert, Tine Deconinck, Lieve R F Claes, Liesbet Deprez, Katrien Smets, Dimitrina Hristova, Iglika Yordanova, Albena Jordanova, Berten Ceulemans, An Jansen, Danièle Hasaerts, Filip Roelens, Lieven Lagae, Simone Yendle, Thorsten Stanley, Sarah E. Heron, John C. Mulley, Samuel F. Berkovic, Ingrid E. Scheffer, and Peter De Jonghe. KCNQ2 encephalopathy: Emerging phenotype of a neonatal epileptic encephalopathy. *Annals of Neurology*, 71(1):15–25, 2012.

[122] Chuan Tian, Ruixin Zhu, Lixin Zhu, Tianyi Qiu, Zhiwei Cao, and Tingguo Kang. Potassium channels: structures, diseases, and modulators. *Chemical biology & drug design*, 83(1):1–26, January 2014.

[123] S E Kasner and M B Ganz. Regulation of intracellular potassium in mesangial cells: a fluorescence analysis using the dye, PBFI. *Am J Physiol*, 262(3 Pt 2):F462–7, 1992.

[124] Ren Hugang, Luo Zhongchi, S Elinav, Pan Yingtian, R Fine, and Du Congwu. Simultaneous assessing the intracellular potassium and calcium concentrations noninvasively in vivo with high resolution fluorescence imaging. *Emerging Technologies for a Smarter World (CEWIT), 2011 8th International Conference & Expo on*, pages 1–6, 2011.

[125] Tomas Wald, Inga Petry-Podgorska, Radovan Fiser, Tomas Matousek, Jiri Dedina, Radim Osicka, Peter Sebo, and Jiri Masin. Quantification of potassium levels in cells treated with Bordetella adenylate cyclase toxin. *Analytical biochemistry*, 450:57–62, 2014.

[126] Xianfeng Zhou, Fengyu Su, Yanqing Tian, Cody Youngbull, Roger H Johnson, and Deirdre R Meldrum. A new highly selective fluorescent K+ sensor. *Journal of the American Chemical Society*, 133(46):18530–3, November 2011.

[127] Theresa S Rimmele and Jean-Yves Chatton. A novel optical intracellular imaging approach for potassium dynamics in astrocytes. *PloS one*, 9(10):e109243, 2014.

[128] Chien-Jung Lo, Mark C. Leake, and Richard M. Berry. Fluorescence Measurement of Intracellular Sodium Concentration in Single Escherichia coli Cells. *Biophysical Journal*, 90(1):357–365, 2006.

[129] C David Weaver, David Harden, Steven I Dworetzky, Barbara Robertson, and Ronald J Knox. A thallium-sensitive, fluorescence-based assay for detecting and characterizing potassium channel modulators in mammalian cells. *Journal of biomolecular screening*, 9(8):671–7, December 2004.

[130] L Michelle Lewis, Gautam Bhave, Brian A Chauder, Sreedatta Banerjee, Katharina A Lornsen, Rey Redha, Katherine Fallen, Craig W Lindsley, C David Weaver, and Jerod S Denton. High-Throughput Screening Reveals a Small-Molecule Inhibitor of the Renal Outer Medullary Potassium Channel and Kir7 . 1. 76(5):1094–1103, 2009.

[131] Rene Raphemot, Rishin J Kadakia, Michelle L Olsen, Sreedatta Banerjee, Emily Days, Stephen S Smith, C David Weaver, and Jerod S Denton. Development and validation of fluorescence-based and automated patch clamp-based

functional assays for the inward rectifier potassium channel Kir4.1. *Assay and drug development technologies*, 11(9-10):532–43, 2013.

[132] T Lu, L Wu, J Xiao, and J Yang. Permeant ion-dependent changes in gating of Kir2.1 inward rectifier potassium channels. *The Journal of general physiology*, 118(November):509–522, 2001.

[133] S. Rezazadeh. Rb+ Flux through hERG Channels Affects the Potency of Channel Blocking Drugs: Correlation with Data Obtained Using a High-Throughput Rb+ Efflux Assay. *Journal of Biomolecular Screening*, 9(7):588–597, 2004.

[134] J.C. Weaver. Electroporation of cells and tissues. *IEEE Transactions on Plasma Science*, 28(1):24–33, 2000.

[135] Eberhard Neumann, Sergej Kakorin, and Katja Tœ nsing. Fundamentals of electroporative delivery of drugs and genes. *Bioelectrochemistry and Bioenergetics*, 48:3–16, 1999.

[136] Stanisława Koronkiewicz and Sławomir Kalinowski. Influence of cholesterol on electroporation of bilayer lipid membranes: Chronopotentiometric studies. *Biochimica et Biophysica Acta - Biomembranes*, 1661:196–203, 2004.

[137] Meredith Lemasurier, Lise Heginbotham, and Christopher Miller. KcsA : It ' s a Potassium Channel. 118(September), 2001.

[138] A. Minta and P.R. Escamilla. *Cytosolic fluorescent ion indicators*. Google Patents, July 2013. EP Patent App. EP20,110,827,351.

[139] Marc Szabo and Mark I Wallace. Imaging potassium-flux through individual electropores in droplet interface bilayers. *Biochimica et Biophysica Acta (BBA)-Biomembranes*, 2015.

[140] Bertil Hille and others. *Ion channels of excitable membranes*, volume 507. Sinauer Sunderland, MA, 2001.

[141] JC Weaver and YA Chizmadzhev. Theory of electroporation: a review. *Bioelectrochemistry and bioenergetics*, 41:135–160, 1996.

[142] G Menestrina. Ionic channels formed by Staphylococcus aureus alpha-toxin: voltage-dependent inhibition by divalent and trivalent cations. *The Journal of membrane biology*, 90:177–190, 1986.

[143] Jianwei Shuai and Ian Parker. Optical single-channel recording by imaging Ca2+ flux through individual ion channels: theoretical considerations and limits to resolution. *Cell calcium*, 37(4):283–99, April 2005.

[144] Ricardo A. Cruciani, Jeffery L. Barker, Stewart R. Durell, Gopalan Raghunathan, H. Robert Guy, Michael Zasloff, and Elis F. Stanley. Magainin 2, a natural antibiotic from frog skin, forms ion channels in lipid bilayer membranes. *European Journal of Pharmacology: Molecular Pharmacology*, 226(4):287–296, 1992.

[145] G Boheim. Statistical analysis of alamethicin channels in black lipid membranes. *The Journal of membrane biology*, 19(3):277–303, 1974.

[146] Paulina D Rakowska, Haibo Jiang, Santanu Ray, Alice Pyne, Baptiste Lamarre, Matthew Carr, Peter J Judge, Jascindra Ravi, Ulla I M Gerling, Beate Koksch, Glenn J Martyna, Bart W Hoogenboom, Anthony Watts, Jason Crain, Chris R M Grovenor, and Maxim G Ryadnov. Nanoscale imaging reveals laterally expanding antimicrobial pores in lipid bilayers. *Proceedings of the National Academy of Sciences of the United States of America*, 110(22):8918–23, 2013.

[147] Sybille Rex. Pore formation induced by the peptide melittin in different lipid vesicle membranes. *Biophysical Chemistry*, 58(1-2):75–85, 1996.

[148] Per Wessman, Adam A. Strömstedt, Martin Malmsten, and Katarina Edwards. Melittin-lipid bilayer interactions and the role of cholesterol. *Biophysical journal*, 95(November):4324–4336, 2008.

[149] K Matsuzaki, O Murase, N Fujii, and K Miyajima. Translocation of a channel-forming antimicrobial peptide, magainin 2, across lipid bilayers by forming a pore. *Biochemistry*, 34(19):6521–6526, 1995.

[150] CT Terwilliger and D Eisenberg. The structure of melittin. *The Journal of biological chemistry*, 257:6–016, 1982. PDB ID 2MLT.

[151] Håkan Steiner, Dan Hultmark, A Engström, Hans Bennich, and Hans G Boman. Sequence and specificity of two antibacterial proteins involved in insect immunity. *The Journal of immunology*, 182(11):6635–6637, 2009.

[152] C. E. Dempsey. The actions of melittin on membranes. *Biochimica et Biophysica Acta - Reviews on Biomembranes*, 1031(2):143–161, 1990.

[153] G Schwarz, R T Zong, and T Popescu. Kinetics of melittin induced pore formation in the membrane of lipid vesicles. *Biochimica et biophysica acta*, 1110(1):97–104, 1992.

[154] G D Eytan and T Almary. Melittin-induced fusion of acidic liposomes. *FEBS letters*, 156(1):29–32, 1983.

[155] Goran Gajski and Vera Garaj-Vrhovac. Melittin: A lytic peptide with anticancer properties. *Environmental Toxicology and Pharmacology*, 36(2):697–705, 2013.

[156] H Vogel and F Jähnig. The structure of melittin in membranes. *Biophysical journal*, 50(4):573–582, 1986.

[157] M S Sansom. The biophysics of peptide models of ion channels. *Progress in biophysics and molecular biology*, 55(ii):139–235, 1991.

[158] K Matsuzaki, S Yoneyama, and K Miyajima. Pore formation and translocation of melittin. *Biophysical journal*, 73(2):831–838, 1997.

[159] L Yang, T a Harroun, T M Weiss, L Ding, and H W Huang. Barrel-stave model or toroidal model? A case study on melittin pores. *Biophysical journal*, 81(3):1475–85, 2001.

[160] JH Lin and A Baumgaertner. Stability of a melittin pore in a lipid bilayer: a molecular dynamics study. *Biophysical journal*, 78(4):1714–1724, 2000.

[161] Seong-Cheol Park, Jin-Young Kim, Sun-Oh Shin, Chan-Young Jeong, Mi-Hyun Kim, Song Yub Shin, Gang-Won Cheong, Yoonkyung Park, and Kyung-Soo Hahm. Investigation of toroidal pore and oligomerization by melittin using transmission electron microscopy. *Biochemical and biophysical research communications*, 343(1):222–8, 2006.

[162] Niv Papo and Yechiel Shai. Exploring peptide membrane interaction using surface plasmon resonance: Differentiation between pore formation versus membrane disruption by lytic peptides. *Biochemistry*, 42(2):458–466, 2003.

[163] Anna Lundquist, Per Wessman, Adrian R. Rennie, and Katarina Edwards. Melittin-Lipid interaction: A comparative study using liposomes, micelles and bilayerdisks. *Biochimica et Biophysica Acta - Biomembranes*, 1778(10):2210–2216, 2008.

[164] Huey W. Huang. Action of antimicrobial peptides: Two-state model. *Biochemistry*, 39(29):8347–8352, 2000.

[165] Jennifer Gesell, Michael Zasloff, and Stanley J Opella. Two-dimensional 1h nmr experiments show that the 23-residue magainin antibiotic peptide is an α-helix in dodecylphosphocholine micelles, sodium dodecylsulfate micelles, and trifluoroethanol/water solution. *Journal of biomolecular NMR*, 9(2):127–135, 1997. PDB ID 2MAG.

[166] M Zasloff. Magainins, a class of antimicrobial peptides from Xenopus skin: isolation, characterization of two active forms, and partial cDNA sequence of a precursor. *Proceedings of the National Academy of Sciences of the United States of America*, 84(15):5449–53, 1987.

[167] K Matsuzaki, K Sugishita, N Fujii, and K Miyajima. Molecular basis for membrane selectivity of an antimicrobial peptide, magainin 2. *Biochemistry*, 34(10):3423–3429, 1995.

[168] B Bechinger, M Zasloff, and S J Opella. Structure and orientation of the antibiotic peptide magainin in membranes by solid-state nuclear magnetic resonance spectroscopy. *Protein science : a publication of the Protein Society*, 2(12):2077–2084, 1993.

[169] S Ludtke, K He, and H Huang. Membrane thinning caused by magainin 2. *Biochemistry*, 34(51):16764–16769, 1995.

[170] Katsumi Matsuzaki, Osamu Murase, Nobutaka Fujii, and Koichiro Miyajima. An antimicrobial peptide, magainin 2, induced rapid flip-flop of phospholipids coupled with pore formation and peptide translocation. *Biochemistry*, 35(35):11361–11368, 1996.

[171] Steve J. Ludtke, Ke He, William T. Heller, Thad A. Harroun, Lin Yang, and Huey W. Huang. Membrane pores induced by magainin. *Biochemistry*, 35(43):13723–13728, 1996.

[172] Khoi Tan Nguyen, Stéphanie V. Le Clair, Shuji Ye, and Zhan Chen. Molecular interactions between magainin 2 and model membranes in situ. *Journal of Physical Chemistry B*, 113(36):12358–12363, 2009.

[173] Mohammad Abu Sayem Karal, Jahangir Md. Alam, Tomoki Takahashi, Victor Levadny, and Masahito Yamazaki. Stretch-Activated Pore of the Antimicrobial Peptide, Magainin 2. *Langmuir*, 31(11):3391–3401, 2015.

[174] Wonyoung Lee and Dong Gun Lee. Magainin 2 Induces Bacterial Cell Death Showing Apoptotic Properties. *Current Microbiology*, 69(6):794–801, 2014.

[175] Robert O Fox and Frederic M Richards. *A voltage-gated ion channel model inferred from the crystal structure of alamethicin at 1.5-Å resolution.* Nature Publishing Group, 1982.

[176] Paul Mueller and Donald O Rudin. Action Potentials induced in Biomolecular Lipid Membranes. *Nature*, 217:713–719, 1968.

[177] Balázs Leitgeb, András Szekeres, László Manczinger, Csaba Vágvölgyi, and László Kredics. The history of Alamethicin: A review of the most extensively studied peptaibol. *Chemistry and Biodiversity*, 4(6):1027–1051, 2007.

[178] L.G.M. Gordon and D.A. Haydon. The unit conductance channel of alamethicin. *Biochimica et Biophysica Acta (BBA) - Biomembranes*, 255(3):1014 – 1018, 1972.

[179] J Kirschbaum, C Krause, R K Winzheimer, and H Bruckner. Sequences of alamethicins F30 and F50 reconsidered and reconciled. *Journal of Peptide Science*, 9(11-12):799–809, 2003.

[180] Gilbert Baumann and Paul Mueller. A Molecular Model of Membrane Excitability. *J. Supramol. Struct.*, 557:538–557, 1974.

[181] R O Fox and F M Richards. A voltage-gated ion channel model inferred from the crystal structure of alamethicin at 1.5-A resolution. *Nature*, 300(5890):325–330, 1982.

[182] Ke He, S. J. Ludtke, W. T. Heller, and Huey W. Huang. Mechanism of alamethicin insertion into lipid bilayers. *Biophysical journal*, 71(November):2669–2679, 1996.

[183] Georg Pabst, Stephan L Grage, Sabine Danner-Pongratz, Weiguo Jing, Anne S Ulrich, Anthony Watts, Karl Lohner, and Andrea Hickel. Membrane thickening by the antimicrobial peptide PGLa. *Biophysical journal*, 95(12):5779–5788, 2008.

[184] Christine Kaduk, Margitta Dathe, and Michael Bienert. Functional modifications of alamethicin ion channels by substitution of glutamine 7, glycine 11 and proline 14. *Biochim. Biophys. Acta*, 1373(1):137–146, 1998.

[185] Annett Rozek, Carol L Friedrich, and Robert EW Hancock. Structure of the bovine antimicrobial peptide indolicidin bound to dodecylphosphocholine and sodium dodecyl sulfate micelles. *Biochemistry*, 39(51):15765–15774, 2000. PDB ID 1G89.

[186] Michael E. Selsted, Michael J. Novotny, Wendy L. Morris, Yi Quan Tang, Wayne Smith, and James S. Cullor. Indolicidin, a novel bactericidal

tridecapeptide amide from neutrophils. *Journal of Biological Chemistry*, 267(7):4292–4295, 1992.

[187] C Subbalakshmi, V Krishnakumari, and R Nagaraj. Requirements for antibacterial and hemolytic activities in the bovine neutrophil derived 13-residue peptide indolicidin. *FEBS Letters*, 395:48–52, 1996.

[188] Timothy J. Falla, D. Nedra Karunaratne, and R. E W Hancock. Mode of action of the antimicrobial peptide indolicidin. *Journal of Biological Chemistry*, 271(32):19298–19303, 1996.

[189] Manhong Wu, Elke Maier, Roland Benz, and Robert E W Hancock. Mechanism of interaction of different classes of cationic antimicrobial peptides with planar bilayers and with the cytoplasmic membrane of Escherichia coli. *Biochemistry*, 38(22):7235–7242, 1999.

[190] A S Ladokhin, M E Selsted, and S H White. Bilayer interactions of indolicidin, a small antimicrobial peptide rich in tryptophan, proline, and basic amino acids. *Biophysical journal*, 72(2 Pt 1):794–805, 1997.

[191] A. Rozek, C. L. Friedrich, and R. E W Hancock. Structure of the bovine antimicrobial peptide indolicidin bound to dodecylphosphocholine and sodium dodecyl sulfate micelles. *Biochemistry*, 39(51):15765–15774, 2000.

[192] Alexey S. Ladokhin, Michael E. Selsted, and Stephen H. White. CD spectra of indolicidin antimicrobial peptides suggest turns, not polyproline helix. *Biochemistry*, 38(38):12313–12319, 1999.

[193] Tatyana I. Rokitskaya, Nikolay I. Kolodkin, Elena a. Kotova, and Yuri N. Antonenko. Indolicidin action on membrane permeability: Carrier mechanism versus pore formation. *Biochimica et Biophysica Acta - Biomembranes*, 1808(1):91–97, 2011.

[194] Attila Gergely Végh, Krisztina Nagy, Zoltán Bálint, Ádám Kerényi, Gábor Rákhely, György Váró, and Zsolt Szegletes. Effect of Antimicrobial Peptide-Amide: Indolicidin on Biological Membranes. *Journal of Biomedicine and Biotechnology*, 2011:1–6, 2011.

[195] Chris Neale, Jenny C Y Hsu, Christopher M. Yip, and Régis Pomès. Indolicidin binding induces thinning of a lipid bilayer. *Biophysical Journal*, 106(8):29–31, 2014.

[196] Igor Vodyanoy, James E. Hall, T. M. Balasubramanian, and Garland R. Marshall. Two purified fractions of alamethicin have different conductance properties. *BBA - Biomembranes*, 684(1):53–58, 1982.

[197] Kamran C. Melikov, Vadim A. Frolov, Arseniy Shcherbakov, Andrey V. Samsonov, Yury A. Chizmadzhev, and Leonid V. Chernomordik. Voltage-Induced Nonconductive Pre-Pores and Metastable Single Pores in Unmodified Planar Lipid Bilayer. *Biophysical Journal*, 80(4):1829–1836, 2001.

[198] G. Beschiaschvili and J Seelig. Mellitin binding to mixed phosphatidylglycerol/phospatidylcholine membranes. *Biochemistry*, 29(1987):52–58, 1990.

[199] Markus R. Wenk and Joachim Seelig. Magainin 2 amide interaction with lipid membranes: Calorimetric detection of peptide binding and pore formation. *Biochemistry*, 37(11):3909–3916, 1998.

[200] V Rizzo, S Stankowski, and G Schwarz. Alamethicin incorporation in lipid bilayers: a thermodynamic study. *Biochemistry*, 26(10):2751–9, 1987.

[201] Sarah a Fowler and Helen E Blackwell. Structure-function relationships in peptoids: recent advances toward deciphering the structural requirements for biological function. *Organic & Biomolecular Chemistry*, 7(8):1508–1524, 2009.

[202] Yuichi Imura, Minoru Nishida, and Katsumi Matsuzaki. Action mechanism of PEGylated magainin 2 analogue peptide. *Biochimica et Biophysica Acta - Biomembranes*, 1768(10):2578–2585, 2007.

[203] Diana Giménez, Orlando L. Sánchez-Muñoz, and Jesús Salgado. Direct Observation of Nanometer-Scale Pores of Melittin in Supported Lipid Monolayers. *Langmuir*, 31(10):3146–3158, 2015.

[204] Kenneth J. Barns and James C. Weisshaar. Real-time attack of ll-37 on single bacillus subtilis cells. *Biochimica et Biophysica Acta (BBA) - Biomembranes*, 1828(6):1511 – 1520, 2013.

[205] K. Matsuzaki, K. I. Sugishita, N. Ishibe, M. Ueha, S. Nakata, K. Miyajima, and R. M. Epand. Relationship of membrane curvature to the formation of pores by magainin 2. *Biochemistry*, 37(98):11856–11863, 1998.

[206] M Lafleur, JF Faucon, J Dufourcq, and M Pézolet. Perturbation of binary phospholipid mixtures by melittin: a fluorescence and Raman spectroscopy study. *Biochim. Biophys. Acta*, 980:85–92, 1989.

[207] Gabrielle de Wit, John SH Danial, Philipp Kukura, and Mark I Wallace. Dynamic label-free imaging of lipid nanodomains. *Proceedings of the National Academy of Sciences*, 112(40):12299–12303, 2015.

Appendix A

Publications

A.1 Accepted

Marc Szabo and Mark I Wallace. Imaging potassium- flux through individual electropores in droplet interface bilayers. *Biochimica et Biophysica Acta (BBA)-Biomembranes*, 2015 (Accepted for publication 20 July 2015)

A.2 In preparation

Marc Szabo, Jason T Sengel and Mark I Wallace. Analysis of pore formation by antimicrobial peptides with combined calcium-flux and single-molecule imaging (in preparation, not submitted)

Appendix B

Code

B.1 Potassium imaging: step profile

```
Volt=[0 -20 -40 -60 -80 -100 -120 -140 -160 -180 -200 -220 -240]';
close all
Size_Step=size(Step);
interval=15/0.05;
StepAv=0;
AvProfile=0;
Average=0;
window=100;
cycle= 30/0.05;
for j=1:Size_Step(2);
    i=1;
    position=0;

    while (position+cycle)<= (length(Step));

        S=mean(Step((position+window):(position+interval-window),j),1);
        StepAv(i,j)= S;
```

```
            position=position+cycle;
            i=i+1;
    end
end


for j=1:13;

    AvProfile(j,1)= mean(StepAv(j,:),2);
    Stand_dev(j,1)=std(StepAv(j,:))/sqrt(j);
end
for j=1:14;
plot(Step(:,j));
figure();
end
Average=sum(Step,2);
figure()
plot(Volt,AvProfile,'+')
figure()
plot(Average/Size_Step(2))
```

B.2 Potassium imaging: squarewave profile

```
close all;
pointer=200;
interval=399;
Signal=Pore_data;
Signalnew=0;
Signalmult=0;
Signalav(1:(interval+1))=0;
counter=0;
```

```
Timenew=0.05:0.05:20;
n=1:1:400;
while (pointer+interval)<= length(Signal-32000);

    counter=counter+1;
    for i=pointer:(pointer+interval);

        Signalnew(i-199)=Signal(i);
        m=mod(i-200,400)+1;
        Signalmult(m,counter)=Signal(i);
    end
    pointer=pointer+interval;
end
for j=1:counter
  Signal_Mult_Av(:,j)= (Signalmult(:,j))/(mean(Signalmult((150:200),j),1));
end
Signalav=nanmean(Signalmult,2);

figure();
plot(Signalnew);
figure();
plot(Timenew,Signalav);
figure();
plot(Timenew,Signal_Mult_Av,'+','MarkerSize',2);
figure();
plot(Timenew,Signalmult,'+','MarkerSize',2);
```

B.3 AMP imaging: radial distribution functions

```
%This code calculates the distribution around one point Radius
%for averaging and distance limit can be varied
```

```
close all
clear Diff;
clear Corrdinates XY;
clear countsnorm;
clear counts;
clear centres;
clear Counts_total_norm;
clear Distances;
clear Counts_total_Av;
clear Counts_Av;
clear Countstotal;
clear Points;
px=0;
py=0;
k=1;
figure
PoreX=92;
PoreY=80;
radius=0;
CoordinatesXY=Coordinates(:,2:3);
i=1;
inc=2;
limit=30;
startX=PoreX-radius;
endX=PoreX+radius;
startY=PoreY-radius;
endY=PoreY+radius;

for px=startX:1:endX;
    for py=startY:1:endY;
```

```
        x=(0:inc:limit);
        xaxis=(inc:inc:limit);
        Diff(:,1)=px-CoordinatesXY(:,1);
        Diff(:,2)=py-CoordinatesXY(:,2);
        Distances=sqrt(sum(Diff.^2, 2));
        [Countstotal(:,i),edges]=histcounts(Distances,x);
        Points(:,i)=[px py];
        i=i+1;
    end
end
    Counts_Av(:,1)=mean(Countstotal,2);

for j=1:1:size(Counts_Av,1);
    Counts_total_Av(j)=sum(Counts_Av(1:j));
    Counts_total_norm(j)=Counts_total_Av(j)/(4*pi*inc*inc*j*j*Av_number);
end


subplot(2,1,1)
bar(xaxis,Counts_total_Av)
xlim([0 limit+1])
set(gca,'fontsize',10)
title([' Pore = (' int2str(PoreX) ',' int2str(PoreY) ')..
                                ..R= ' int2str(radius) ' '],'FontSize',10)

subplot(2,1,2)
bar(xaxis,Counts_total_norm)
xlim([0 limit+1])
yL=max(Counts_total_norm);
ylim([0 yL+1])
set(gca,'fontsize',10)
```

```
Pore_92_80=Counts_total_norm;
save('Pore_92_80');
save('C:\Dokumente\DPhil\AMP electro\AMP Paper\Analysis\Magainin\
                                Total pores\Pore_92_80.mat','Pore_92_80');
```

B.4 Gaussian fitting of pores

```
#pragma rtGlobals=1     // Use modern global access method.
#include  <All IP Procedures>
#include  <Image Saver>


Function LoadStack()
// Loads an image stack. Must be modifed to include a dialogue eventually
ImageLoad/T=tiff/S=0 /C=-1 /O /N=image //Loads the images
End

//to estimate backgroud use wavestats image

Function Gauspatches(patchsize, threshold, coverage)
variable patchsize //actually the RADIUS not DIAMETER of patch
variable threshold
variable coverage
wave image
variable i,j,k,m,n
Duplicate /O image image_cleaning
Make /O/N=1000 spot_count
Make /O /N=(1000,2,dimsize(image,2)) spotXpos=0, spotYpos=0, spotintensity=0
make /O/N=(6,1000,dimsize(image,2)) cf_list//=NaN
make /O/N=(6,1000,dimsize(image,2)) er_list//=NaN
Make /O/N=1000  W_coef_temp
```

```
Make /O/N=1000  W_sigma_temp
//Make /O/N=(1000,7,1000) output=0
//Set up stuff for drawing on screen
ImageTransform sumPlanes image
NewImage/K=0 /s=1 M_SumPlanes
ModifyGraph width=276,height=276
ModifyImage M_SumPlanes ctab={*,*,Grays,0}
SetDrawLayer ProgFront
SetDrawEnv linefgc= (65535,65535,0),fillpat= 0,xcoord= top,ycoord= left, save
//Now Clean and Fit
for (m=0; m<dimsize(image,2); m+=1) //each frame
    do
        ImageStats  /M=1 /P=(m) image_cleaning //find MaxX MaxY MaxInt
        Make /O/N=(Dimsize(image,0),Dimsize(image,1)) frame1=0
        frame1[][] = image_cleaning[p][q][m] //Just use one frame at a time
   for(j=0;j<=2*patchsize;j+=1)
   for(k=0;k<=2*patchsize;k+=1)
      spotXpos[i][0][m]=i+1
      spotYpos[i][0][m]=i+1
      spotintensity[i][0][m]=i+1
      spotXpos[i][1][m]=V_maxRowLoc
      spotYpos[i][1][m]=V_maxColLoc
      spotintensity[i][1][m]=V_max
    //output[i][0][m]=i+1
 duplicate /O/R=(V_maxRowLoc-j,V_maxRowLoc+j)(V_maxColLoc-j,V_maxColLoc+j)
                    frame1 gauss_frame //select patch to fit
    FitGauss(m) //fit
    cf_list[][i][m] = W_coef_temp[p] //write coefficients to file
    er_list[][i][m] = W_sigma_temp[p] //write errors to file
endfor
endfor
DrawRect V_maxRowLoc-patchsize,V_maxColLoc-patchsize,
```

```
                V_maxRowLoc+patchsize,V_maxColLoc+patchsize //Draw rectangle
        image_cleaning[(V_maxRowLoc-patchsize*coverage),
        (V_maxRowLoc+patchsize*coverage)][(V_maxColLoc-patchsize*coverage),
        (V_maxColLoc+patchsize*coverage)][m] = 0 //remove patch
        i+=1 //keep counting
    while (V_max>threshold)
    spot_count[i]=i
    i=0 //reset for each frame
endfor
n=0
print n
Edit cf_list
End

Function FitGauss(image_number)
variable image_number
Variable V_fitOptions = 4           // suppress progress window
Variable V_FitError = 0         // prevent abort on error
NewDataFolder /O root:temp
SetDataFolder root:temp
Make /O/N=7  W_coef
Make /O/N=7  W_sigma
Make/O/T/N=6 T_Constraints
T_Constraints[0] = {"K0 > 0","K1 > 0","K2 > 0","K3 > 0","K4 > 0","K5 > 0"}
Duplicate /O/R=[][][image_number] root:gauss_frame root:temp:imagetemp
Redimension/N=(-1,-1) imagetemp
Wavestats /Q imagetemp
K0 = V_avg
K1 = V_max-V_avg
K2 = V_maxRowLoc
K3 = 0.6
K4 = V_maxColLoc
```

```
K5 = 0.6
K6 = 0
//Print K0, K1, K2, K3, K4, K5, K6
CurveFit /G/N/Q/H="0000001" Gauss2D  imagetemp /D  /C=T_Constraints
    If (V_FitError !=0)
        //Printf " Bad %d \r", image_number
        W_coef=NaN
        W_sigma=NaN

    endif
Duplicate /O W_coef root:W_coef_temp
Duplicate /O W_sigma root:W_sigma_temp
//Print W_coef
SetDataFolder root:
End
```